Ground Source Heat Storage and Thermo-Physical Response of Soft Clay

by

Shoshanna Dawn Saxe

B. Eng Civil Engineering and Applied Mechanics (2007)

McGill University

Submitted to the Department of Civil and Environmental Engineering in Partial Fulfillment of the Requirements for the Degree of Master of Science in Civil and Environmental Engineering

at the

Massachusetts Institute of Technology

September 2009





Signature of Author .....
Department of Civil and Environmental Engineering
August 7, 2009

Certified by .....
Andrew J. Whittle
Professor of Civil and Environmental Engineering
Thesis Supervisor

Accepted by .....
Daniele Veneziano
Chairman, Departmental Committee for Graduate Students

Ground Source Heat Storage and Thermo-Physical Response of Soft Clay
by
Shoshanna Saxe
Submitted to Department of Civil and Environmental Engineering
on August 7, 2009 in Partial Fulfillment of the
Requirements for the Degree of

Master of Science in Geotechnical Engineering

# ABSTRACT

Ground source heat storage can condition buildings with reduced consumption of fossil fuels, an important issue in modern building design. However, seasonal heat storage can cause soil temperature fluctuations and possibly deformation of soft clays. This thesis evaluates the thermo-mechanical response of soft clays to seasonal heat storage and associated temperature fluctuations.

A literature review reveals that, in normally consolidated to lightly overconsolidated clays, increases in soil temperature can lead to significant plastic strains and a reduction in soil strength. This behavior can be modeled through constitutive formulations that include thermal strain within the elasto-plastic framework of the well-known Modified Cam-Clay Model. The current research uses the MCC Picard (1994) model to study the ground response to a buried heat exchange pipe. The spacing of the pipe was found to govern the effectiveness of ground heat storage. With only one pipe in semi-infinite soil, heat transfer to the ground dissipates quickly and thermal-mechanical interaction is negligible; however, seasonal heat storage is not possible. Closely spaced heat pipes would permit effective seasonal heat storage, but could undergo significant thermally induced consolidation deformations.

Thesis Supervisor: Andrew J. Whittle
Title: Professor of Civil and Environmental Engineering

# Acknowledgements

I would like to thank my advisor, Professor Andrew J. Whittle, for suggesting this topic and offering me the opportunity to study at the intersection of geotechnical engineering and green design; without him, this thesis would not have been possible.

Thank you to Emmanuel Bourgeois for his invaluable guidance on the internal workings of CESAR-LCPC and for clueing me in to the hidden existence of the Picard Model.
I am grateful to Professor Herbert Einstein and Professor Leslie Norford for supporting me through the teaching assistant positions that allowed me to pursue this research.

Thank you to my favorite sister, Rebecca, who can be found studying brains on her computer screen and who was the best part of living in Cambridge. To my parents, Dianne and Stewart Saxe, for their patience, advice and guidance (and particularly to my mother for the commas and 'below' not 'bellow'). To David, my big brother, who toughened me up. To Gloria, for her inexhaustible enthusiasm and encouragement. To Allan, who figured out the force distribution of a bicycle wheel upon demand. Thank you to Tanhum, for supporting my becoming a 'Master' before I become his wife.

Thank you to Christina, Despina, Nikolas P., Adonis, Yannis, Ruben, Giorgos, Kostas and Fillipos for the late nights and the early mornings. Thank you to Nikolas G. who never let go of the other end of the rope. Thank you to Tess and Steph for being the type of people who will spell the letter 'R' with their bodies on a street corner for no better reason other than it seemed like a good idea at the time.

Last but not least, thank you to my Branksome Girls for being true friends, 10 years on and counting.

"Oh! Piglet," said Pooh excitedly, "we're going on an Expotition, all of us, with things to eat. To discover something."

"To discover what?" said Piglet anxiously.

"Oh! Just something."

A.A. Milne

# Table of Contents

# List of Tables

# List of Figures

# 1 INTRODUCTION

Concern about global warming, emissions of greenhouse gases ($CO_2$, $CH_4$, etc) and the increased price of petroleum has led to a drive for increased energy efficiency in buildings. The vast majority of buildings require heating and/or cooling at least part of the year. This research considers the development of ground based heat storage systems, a technology that harnesses the thermal storage capacity of soils, and any associated impacts from thermal changes in clay. The use of the subsurface for energy storage can lead to a significant reduction in the use of primary energy used for heating and cooling, and effectively reduce emissions of $CO_2$ from new buildings (Laloui et al., 2006).

Soil and rocks have much larger thermal storage capacity than air and significant thermal inertia[1]. Air temperature fluctuations have minimal effects on the temperature of the ground. Even the effects of large seasonal shifts in air temperature extend only a few meters into the ground. At depths 5 to 10 m below ground surface, the temperature remains constant at the annual average air temperature. This leads the ground to be particularly suited for heat storage. Excess heat energy can be discharged to the ground in the summer for cooling and used in the winter for heating. Technologies that take advantage of the ground capacity to act as a heat source and sink are generally referred to as geothermal or ground-source heat pumps (GHP). A GHP is a loop of pipes running through the ground. A saline solution or antifreeze is pumped through the loop to exchange heat with the surrounding ground. In winter, the system extracts heat from the ground for heating and, in summer, rejects heat to the ground providing cooling. It is sometimes possible to run GHPs at temperatures high enough for water heating.

---

[1] The large mass of the ground combined with the large thermal storage capacity of soils and rocks make it possible for the ground to absorb a large quantity of energy with minimal temperature effects

GHPs have been used increasingly since the 1970's to increase building efficiency and decrease the use of primary energy sources. Like all heat pumps, GHPs require electricity to run the pump. However, the output of heating or cooling energy is many multiples the necessary input. The coefficient of performance (COP) is a ratio that describes the amount of energy moved by a heat pump, divided by the energy input to run it. The COP of GHPs is currently in the range of 3-5. With increased adoption, the technology is expected to reach a COP of 6-8 (Hughes, 2008). GHPs are found in many forms; the two most common GHPs are ground heat exchangers in vertical boreholes and in horizontal loops.

Energy foundations are a new type of GHP emerging in Europe. They combine the mechanical ground components of a GHP within the concrete foundation elements of a structure. This reduces construction costs and takes advantage of the large thermal storage capacity of concrete, significantly reducing the initial capital cost of a GHP. The use of energy foundations began in the 1980's in Austria and Switzerland (Brandl, 2006). The first energy foundations were energy base slabs and piles; the technique has expanded to energy diaphragm walls and most recently to energy tunnels. As a first estimate, 30-35 $W/m^2$ of heat energy can be extracted from earth-contact through fully embedded energy foundations.

Ideally, at the end of one heating and cooling cycle, the temperature of the ground should be returned to the annual average air temperature (the in situ temperature of the soil). A common obstacle to the adoption of GHPs is that the cooling season is longer than the heating season for many office buildings. A longer cooling season would drive up the ground temperature over time, reducing the efficiency of the ground as a heat sink. For this reason, GHPs are best suited to climates with distinct heating and cooling seasons of approximately equal length.

Soils, and clay in particular, exhibit deformation properties that are affected by changes in temperature. Thermal studies on clay have indicated that thermal stresses can lead to important behavior changes:

- A decrease in apparent preconsolidation pressure with increasing temperature;
- Increased deformation at constant stress with increasing temperature; and
- Decreasing shear strength at failure with increasing temperature.

These effects are most pronounced in normally and lightly over-consolidated clays.

For these reasons, the use of a GHP in clay can lead to significant deformations and lower strength in the clay. To date, GHPs in clay have been physically removed from the built environment to avoid any negative effects due to the changing temperature of the clay (Moritz, 1995). This requirement is a barrier to the adoption of energy foundations and to the widespread use of GHPs in the urban environment. The goal of this paper is to investigate the deformation and strength changes that occur in clay, due to changes in temperature. A better understanding of this behavior is needed to facilitate the adoption and safe utilization of urban GHPs, including energy foundations.

This thesis investigates the thermo-mechanical properties of clay and the ground response associated with ground source heat exchangers. Chapter 2 provides an extensive background on heat exchange and heat storage in the ground, including a summary of thermal properties of the ground and the measured performance of prototype heat storage system. Chapter 3 reviews the thermo-mechanical response of clay, as measured in laboratory tests. Chapter 4 presents a summary of a constitutive model proposed by Picard (1994) for simulating the coupling of thermal and mechanical properties, and illustrates the model performance in simulating elemental behavior observed in laboratory tests. The Picard Model (Beta version) has been integrated within a commercial finite element code CESAR-LCPC. Chapter 5 presents numerical fluctuations of mechanical response for idealized ground source heat exchange systems.

# 2 GROUND SOURCE HEAT EXCHANGE AND HEAT STORAGE

The year round constant temperature of the ground makes it an excellent medium for heat storage and heat exchange. This chapter looks at the thermal regime in the ground, the thermal properties pertinent to the design and operation of ground heat storage systems and different approaches to ground heat storage.

## 2.1 Subsurface Thermal Environment

Air temperatures, heat from the Earth's core, and thermal properties of the soil determine ground temperatures. Near the surface, where ground source heat exchangers operate, the influence of heat from the Earth's core is negligible. Soil and rocks have much larger thermal storage capacity than air and significant thermal inertia. Air temperature fluctuations have minimal effects on the temperature of the ground at depth (Andersland and Ladanyi, 2004). Even the effects of large seasonal shifts in air temperature only extend a few meters into the ground. Figure 2.1a illustrates how the air temperature changes over a year, fluctuating around the mean annual temperature. Due to the high thermal storage capacity of the ground, changes in the surface temperature lag behind changes in air temperature and depend on depth. Figure 2.1b illustrates the decreasing influence of the seasonal temperature on the ground with depth.

At depths 5 to 10 m below ground surface, the temperature of the ground remains constant at the annual average air temperature. In continental Europe, Canada, and the northern US, this temperature generally ranges from 8-16 °C. Table 2.1 lists the annual average air temperature for cities in Canada, Europe and the United States. This constant ground temperature can be harnessed by a ground-source heat pump for the conditioning of buildings. In the summer, when the ground is colder than the air, the temperature difference can be harnessed using heat exchanges and a heat pump to cool buildings.

Conversely, in the winter, when the ground is warmer than the air, the temperature difference can be used to heat the building. During the summer, excess heat is exhausted to the ground to provide air conditioning, raising the temperature of the soil. The heat stored in the summer can be used for heating in the winter. In regions closer to the equator, where the weather is warm year-round, the ground temperature 10 mBGS is closer to 20-25°C. It is still possible to use this hotter ground for cooling, but precautions have to be taken to prevent sustained changes in the annual average ground temperature.

## 2.2 Thermal Properties of Soils

### 2.2.1 Thermal Conductivity and Heat Capacity

Three main parameters control the thermal response of the ground:

(1) The amount of heat energy inputs, Q, [W];

(2) The thermal conductivity of the soil, $k_T$ [W/mK];

(3) The volumetric heat capacity of the soil, $C_v$ [J/m$^3$K].

The thermal conductivity and specific heat capacity are intrinsic properties of the soil; heat energy input depends on the operation of the ground source heat pump.

Table 2.2 lists the heat capacity and thermal conductivity for air, water, ice and a number of geomaterials.

The thermal conductivity of clay is an addition of the thermal conductivities of its constituents: soil minerals, water and air. Johansen (1975) developed the following formula for thermal conductivities of soils:

$$k_{dry}(W/mK) = \frac{0.137\rho_d + 64.7}{2{,}700 - 0.947\rho_d} \pm 20\% \qquad (2.1)$$

Where $\rho_d$ is the dry density (kg/m$^3$) and the average density of solid particles is 2700 kg/m$^3$. For saturated unfrozen soils, the thermal conductivity can be approximated by:

$$k_{sat} = k_{dry}^{1-n} k_w^n \qquad (2.2)$$

Here n is the soil porosity and $k_w$ is the thermal conductivity of water. GHPs should never operate below the freezing temperature; the thermal conductivity of frozen soils will not be dealt with here. Other models for calculating the thermal conductivity of soils have been developed since Johansen's 1975 thesis (Cote and Konrad 2005; Gong and Horton, 2007). However, these models depend on knowledge of the soil particle shapes and are therefore less widely applicable.

For fine soils, the thermal conductivity can be estimated from:

$$k = 0.1442(0.9 \log w - 0.2)(10)^{0.6243\rho_d} \qquad (2.3)$$

Where w is the water content of the soil (Johansen 1975). Figure 2.2 illustrates the range of thermal conductivity with water content and dry density for fine-grained soils.

Similarly, the heat capacity of soils can be calculated from the heat capacity and mass fraction of its constituents. Most soils have a heat capacity ranging from 670-1050 J/kgK (Esch, 2004).

For an unfrozen soil, the heat capacity can be calculated from:

$$c = \frac{1}{m}\left(c_s m_s + c_w m_w + c_{air} m_{air}\right) \qquad (2.4)$$

where m is mass and c is heat capacity of each constituent. Knowing that specific heat capacity is the ratio of the heat capacity of the soil to that of water, it is possible to calculate volumetric heat capacity $c_v$:

$$c_v = \left(\frac{\rho_d}{\rho_w}\right)\left(0.17 + 1.0\frac{w}{100}\right)c_{vw} \qquad (2.5)$$

Where $c_{vw}$ is the volumetric heat capacity of water (Andersland and Ladanyi, 2004).

### 2.2.2 Measuring Thermal Properties

The most common tests used for finding the thermal constituents of soils are the Guarded Hot Plate test, the Probe Test, and the Dual Probe Test.

The Guarded Hot Plate test is a steady state test, in which, two identical soil specimens are placed above and below a flat plate heater. To prevent horizontal heat losses, a horizontal guard heater surrounds the two specimens and heater. Cool heat sinks are placed on the top and bottom surfaces of the soil creating a heat drop of $\Delta T$ across the samples. The thermal conductivity of the sample can then be calculated by:

$$k = \frac{Q}{A}\frac{\Delta x}{\Delta T} \qquad (2.6)$$

Where Q is the rate of heat flow, A is the area of the specimen and $\Delta x$ is the thickness of the specimen. The Guarded Hot Plate test can be complicated to run and time consuming, and is usually only used in the laboratory. The test takes a long time to reach steady state. The large $\Delta T$ that is applied can cause moisture migration in the soil, causing a change in k. Another disadvantage of the Guarded Hot Plate test is the effect of gravity; the heat flow upwards is often significantly greater than the heat flow downwards. Nonetheless, the Guarded Hot Plate test is widely used and considered satisfactorily accurate (Farouki, 1986).

The thermal probe method is a transient test that can be used in laboratory or in situ. It comprises a thin needle, with a heater producing thermal energy, and a temperature sensor. Enough thermal energy is applied to raise the temperature of the probe by 1 or 2 K. The thermal conductivity of the soil can be calculated from:

$$k = \frac{q}{4\pi(T_2 - T_1)} \ln\left(\frac{t_2}{t_1}\right) \qquad (2.7)$$

where $T_1$ corresponds to the temperature probe at time, $t_1$ (Farouki, 1986), q is the input heat.

The dual probe test is a further development of the single probe method. Two probes are placed in the soil. A heat pulse is emitted from one probe and the temperature is measured at both probes with time. This allows for the thermal conductivity and thermal diffusivity to be measured simultaneously. The heat capacity is then calculated from the thermal diffusivity, D, and the thermal conductivity, k:

$$c_p = \frac{k}{\rho D} \qquad (2.8)$$

where ρ is the density of the soil (Sailor et al 2008).

## 2.3 Ground Heat Storage and Heat Exchange Systems

The ground can be used for heat storage and heat exchange in a number of different ways. The following paragraphs provide an overview of geothermal heat pumps, energy foundations and an in-depth look at a heat storage field run by the Swedish Geotechnical Institute.

### 2.3.1 GHP

The purpose of a GHP is to provide conditioning to a building with minimal or no reliance on fossil fuel-derived energy. Energy input is needed to move the heat transfer fluid and to power the heat pump, but this is many times less energy needed than to heat

the building directly. If a GHP is coupled to a solar panel, it can be run on entirely 'green' energy. The basic concept of GHPs is simple; vertical boreholes or horizontal trenches are used to exchange heat with the ground. During the cooling season (summer), excess heat is rejected to the ground and the ground acts as a heat sink. In the heating season (winter), the ground acts as a heat source and feeds heat into the building (Preene and Powrie, 2009).

GHPs can be run as open or closed loop systems. Open loop systems involve pumping ground water to the surface and running it through a heat exchanger and, finally, disposing of the water. This process changes the temperature of the ground water and can lead to thermal pollution. In closed loop systems, a heat exchange fluid is run through pipes buried in the ground. As the fluid travels through the pipes, it exchanges heat with the ground. The fluid is then passed through a heat pump. A heat pump is a refrigerant thermal exchange system that is efficient at transferring heat from one source to another. In this case, heat passes from the exchange fluid to the building heating system in the heating season and from the building cooling system to the exchange fluid during the cooling season (Preene and Powrie, 2009). Figure 2.3 illustrates some typical GHP geometries.

GHPs have been used increasingly since the 1970's to increase building efficiency and decrease the use of primary energy sources. Like all heat pumps, GHPs require the input of electricity to run the pump. However, the output of heating or cooling energy is many multiples the necessary input. The coefficient of performance (COP) is a ratio that describes the amount of energy moved by a heat pump divided by the energy input to run it. The COP of GHPs is currently in the range of 3-5. With increased adoption, the technology is expected to reach a COP of 6-8 (Hughes, 2008).

A ground energy system can be divided into three parts:

1. The source side: comprised of subsurface components, such as ground loops;
2. The load side: comprised of building and its conditioning loads, and;

3. The heat transfer system: comprised of the heat pump (Preene and Powrie, 2009).

The amount of thermal stress applied to the source side, the ground, depends on the amount of heating or cooling energy needed on the load side, the building, and the amount of ground activated by the system.

Many GHP systems have been designed without detailed geotechnical investigation; stock values for in-situ ground temperature, thermal conductivity and heat capacity were used. There has been very little long term monitoring of these systems (Preene and Powrie, 2009). GHP are usually operated between 5-40°C. More recently, there have been investigations into ground source heat storage at much higher temperatures, up to 90°C. High temperature heat storage eliminates the need for a heat pump and presents the possibility of ground-heated hot water, and of gaining more heating/cooling energy from the same volume for activated soil. For this reason high temperature stores have the potential to be more technically and economically feasible than lower temperature storage (Gabrielsson et al., 1997).

## 2.3.2 Energy Foundations

Brandl (2006) discussed a pilot research project where energy piles were installed to supply heating and cooling for a rehabilitation center. The seven-floor structure had a volume of 90,000 $m^3$ and a usable area of 21,500 $m^3$. 143 of the piles were fitted with heat exchangers for a total length of 2,050 m of energy piles. Figure 2.4 shows a cross section of the foundation of the rehabilitation center. The subsoil consisted of weathered talus for 2-5 m below ground level. Below that was silty sand to clayey silt underlain by clayey to sandy silt. The 143 piles were able to completely meet the heating and cooling loads of the building. Figure 2.5 shows the conditioning demand and output as well the heat carrier temperature. Figures 2.6 and 2.7 illustrate initial predictions of the temperature distributions around the energy piles from finite element analysis. The soil

temperatures range from just about 0°C during the heating season to a high of 26°C during the cooling season.

Adam and Markiewicz (2009) discuss a number of other energy foundation projects in Austria. The Uniqa Tower in Vienna has energy diaphragm walls that extend to 35 mBGS. Total surface area of 7,800 $m^2$ of diaphragm wall is activated for energy exchange producing 818 MWh of cooling energy and 646 MWh of heating energy. To achieve this, brine is run through the system at temperatures ranging from -2.8°C to 31.8°C. The Uniqa tower was constructed on granular soils; in clay, it would be unwise to run a ground heat storage system below freezing and it could result in very large deformations.

### 2.3.3 Heat Storage and Observations of Thermo-Mechanical Coupling (SGI case study)

The Swedish Geotechnical Institute (SGI) has conducted numerous studies on the use of clay for seasonal heat storage. They have built a number of heat fields; a plot of land with closely placed U-pipe vertical GSPs. Clay heat stores have been used successfully in Sweden since the 1970's. Much of the ground in Sweden is made of soft clay in layers 10-50 m thick. This soft clay has proven an economical medium for long-term heat storage. Most current heat stores operate up to a temperature of 30°C; unfortunately, at this temperature, the heat store can supply limited winter heat (Gabrielsson et al., 1997). SGI's Moritz (1995) and Gabrielsson et al (1997) conducted detailed lab and a large-scale field test on the effects of using soft Swedish clay for ground heat storage for temperatures up to 70°C.

#### 2.3.3.1 In Situ Conditions

The top 1.5- 2.0 meters of the soil was a dry crust of clay. Underneath the crust, there was some organic matter and then pure clay to a depth of 8 meters. Down to 18 meters, the clay exhibited sulphide staining and silt patches. Figure 2.8 shows the soil profile at the Swedish test site.

The clay crust is significantly overconsolidated, below which the clay is lightly overconsolidated, as shown in Figure 2.9. Figure 2.10 shows the ambient daily temperature for the test field. The annual mean ambient temperature ranged from 6.8°C - 8.5°C for the three years of study 1992-1994.

### 2.3.3.2 Field Measurements

A test field for evaluating the effects of a heat store operating at temperatures up to 70°C was built in 1992. The test field consisted of three 1,000 $m^3$ cubic heat stores. Vertical U-shaped ducts with a spacing of 1 m or 2 m were installed to a depth of 10 m in each test store. The tops of the heat stores were insulated. Heat was transferred to and from the soil by a heat transfer fluid distributed through the vertical ducts. Though the project was designed to evaluate the viability of seasonal solar heat storage, for the test field, the heat transfer fluid was heated using electricity. One of the three test stores was heated to 70°C and then held constant at that temperature, one alternated between 35 °C and 70 °C and the third was frozen and thawed with the temperature fluctuating above and below 0°C. In order to accelerate the test, each heating cycle was 3 months long, followed by a 3-month cooling cycle, rather than the 6-month cycles found in nature. The freeze/thaw store experienced extreme deformations and had to be terminated early; the U-shaped ducts became excessively deformed preventing the circulation of heat transfer fluid. Due to the large deformations, the freeze/thaw test was discontinued and is not discussed here (Gabrielsson et al., 1997).

The test fields served three important purposes: 1) to measure the settlements due to heating and 2) to evaluate how far away from the heat store the induced temperature

changes have a measurable effects on the soil, and 3) to evaluate the effect of heat storage on the geotechnical properties of the soil.

Over three years of investigation, Gabrielson et al (1997) found that, upon heating, excess pore pressure developed, triggering consolidation. The increased temperature also led to an increase in secondary compression (i.e., deformations at constant effective stress). After 2 years and 8 months of operation, there was 72 mm of settlement in the store with varying temperature and 88 mm of settlement in the store that had been held constant at 70 °C. During operation of the heat stores, significant excess pore pressures were measured. In heat store 1 with varying temperature, the maximum excess pore pressure measured at 9 m depth was 58 kPa; during cooling of the store, negative excess pore pressures were measured. In heat store 2, with temperature held constant at 70 °C, the maximum excess pore pressure measured at 9 mBGS was 47 kPa. The settlement of stores 1 and 2 with time are shown in Figure 2.11. Store 1 settled 7 cm and store 2 settled 8.5 cm over the course of the test. In heat store 1, there was a notable change in the rate of settlement, reflective of the changes in temperature. The store settled faster during soil heating than during soil cooling. However, there is an offset in this relationship; that change in rate of settlement lagged a number of months behind the change from soil heating to cooling.

The settlements were greatest at the center of the stores and decreased radially. Figure 2.12 shows the settlements of store 1 at the center and 1, 4 and 7 m outside the store.

In store 2, the settlement continued after the excess pore pressure had been dissipated, indicating the effect of temperature induced creep.

Since it is possible that changing the temperature of the soil can have serious effects on the soil properties and can trigger consolidation, it is important to understand how far the influence of the change in temperature extends radially in the ground. In the SGI field study, the temperature outside the boundary of the [10 by 10 by 10 m] heat store was

measured throughout the field study. Figure 2.13 illustrated the change in temperature around the store with time.

After 2 years and 11 months of operation, the heat field disturbance around store 1extended to 23 m from the center of the store, where the change in temperature was 0.1°C.

Test performed to evaluate the shear strength of the soil showed a decrease upon initial heating followed by a rebound to the initial strength. Figures 2.14 a and b show shear strength with time, for stores 1 and 2 respectively.

### 2.3.3.3 Investigation of Soil Properties

Moritz (1995) carried out a program of laboratory drained and undrained triaxial and CRS tests to determine the effect of a change in temperature on the properties of Swedish clay. In order to avoid temperature gradients, the clay was heated at a rate of 10°C/30 minutes.

Triaxial tests were carried out on 12 samples, 6 each from 6 mBGS and 9 mBGS. Of the 12 samples, eight were consolidated to in-situ stress at room temperature and four at 8°C, respectively. The samples that had been consolidated at room temperature were heated under drained or undrained conditions. Undrained compression tests were performed at 8°, 40° and 70 °C.

The heating of the samples resulted in an increase in pore pressure in undrained conditions and a decrease in volume in drained conditions. Table 2.3 shows the increase in pore pressure in the undrained tests (Moritz 1995). Figures 2.15 and 2.16 show the vertical deformation induced by heating samples from 6 and 9 mBGS to 40 and 70 °C. Vertical swelling of 0.2% was found in the sample from 6 mBGS at 70°C; no swelling was found in the sample from 9 mBGS, which compressed slightly. No vertical swelling

was found at 40°C at either depth. The significant decrease in effective horizontal stress, $\sigma'_H$, as the pore pressure increased, likely had a measurable effect on the volume change of the samples. At 9 mBGS, the initial vertical effective stress was $\sigma'_V$ = 70 kPa, $\sigma'_{Vc}$ = 80 kPa and the initial horizontal stress $\sigma'_H$=42 kPa. When the temperature was increased to 70°C, the pore pressure increased 35 kPa, reducing the effective stresses to $\sigma'_V$ = 70-35 = 35 kPa and $\sigma'_H$= 42-35 = 7 kPa, respectively. The effective horizontal stress became so low that the sample was close to active shear failure (Moritz 1995). Figure 2.17 illustrates how the significant reduction in $\sigma'_H$ brought the samples close to failure. In-situ, the much larger mass of clay prevents such a drop in confining stress.

Slow undrained triaxial compression tests showed decreased peak shear strength with increasing temperature. Figure 2.18 shows the results of slow undrained shear for the sample from 6 mBGS[2].

In drained conditions, the samples showed a reduction in volume with time at elevated temperatures. The drained triaxial tests were run for 24 hours. As can be seen from Figure 2.19, 24 hours was not sufficiently long for the specimens to fully drain and achieve maximum settlement; the curves do not level off. However, the trend of decreasing volume is clear (Moritz, 1995).

To determine the changes in compression characteristics of the Swedish clay with temperature, CRS tests were carried out in the laboratory. Figure 2.20 shows the deformation versus effective stress of specimens from 6 mBGS at different temperatures. The samples at higher temperatures exhibit more deformation under the same stress (Moritz 1995).

---

[2] The sample from 9 mBGS was disturbed, making the data unreliable, and is therefore not shown (Moritz 1995).

In the 1-D consolidation (CRS) tests, the apparent preconsolidation of the Swedish clay decreased with increasing temperature; however, the relationship was not linear. The change in preconsolidation with temperature can be approximated by the relationship:

$$\sigma'_{cT} = \sigma'_{cT_0}\left(\frac{T_0}{T}\right)^{0.15} \qquad (2.9)$$

Where $\sigma'_{cT}$ is the preconsolidation pressure [kPa] at temperature T [°C], and $\sigma'_{cTo}$ is the measured preconsolidation pressure [kPa] at room temperature $T_o$ [°C]. Figure 2.21 illustrates this trend.

The SGI research into soft clay as a medium for heat storage provides a wealth of information on the heating of soft soil. However, because the SGI tests were limited to thermal loading, they do not provide insight into the results of both thermally and mechanically loading clay as with energy foundations. In the absence of mechanical loading, it takes a very large amount of heat to cause a slightly OC clay to behave as if it is NC. The clay at the SGI test site is slightly overconsolidated (Figure 2.9) and was not sufficiently heated to behave as a NC clay. In general, SGI found that heating the clay from 8°C to 70°C had minimal effects on the geotechnical properties of the clay; heat induced strains were small, approximately 0.7%, and the change in temperature outside the store decreased rapidly with distance. Nonetheless, both Mortiz (1995) and Gabrielsson (1997) recommend that heat stores should be located a significant distance from slopes, building and other settlement sensitive constructions. With the use of energy foundations, the heated clay would be directly underneath buildings. More research is needed to understand the interaction of both mechanically and thermally loading the soil.

Table 2.1: Annual average air temperature in selected cities (Hoare, 2005)

| City | Annual Average Air Temperature | City | Annual Average Air Temperature |
|---|---|---|---|
| **Europe** | | **United States** | |
| Athens, Greece | 18.5 | Austin, Texas | 20.3 |
| Belgrade, Serbia | 11.6 | Boston, Massachusetts | 15.0 |
| Berlin, Germany | 8.9 | Charlotte, North Carolina | 15.6 |
| Brussels, Belgium | 10.3 | Chicago, Illinois | 10.2 |
| Bucharest, Romania | 10.7 | Columbus, Ohio | 10.7 |
| Budapest, Hungary | 10.4 | Denver, Colorado | 10.1 |
| Copenhagen-Malmö, Denmark/Sweden | 7.8 | Detroit, Michigan | 10.1 |
| Frankfurt Rhine Main Area, Germany | 9.8 | Indianapolis, Indiana | 11.2 |
| Hamburg Metropolitan Region, Germany | 8.6 | Jacksonville, Florida | 20.0 |
| Istanbul, Turkey | 14.1 | Las Vegas, Nevada | 19.5 |
| Kiev, Ukraine | 7.1 | Los Angeles, California | 17.7 |
| Lille-Kortrijk. France/ Belgium | 9.6 | Memphis, Tennessee | 16.8 |
| Lisbon, Portugal | 15.9 | Milwaukee, Wisconsin | 7.9 |
| London, UK | 11.7 | New York, New York | 11.5 |
| Madrid, Spain | 14.2 | Philadelphia, Pennsylvania | 12.3 |
| Marseille, France | 14.2 | Phoenix, Arizona | 21.4 |
| Milan, Italy | 12.7 | Portland, Oregon | 12.0 |
| Minsk, Belarus | 9.4 | San Diego, California | 18.1 |
| Moscow, Russia | 4.2 | San Francisco, California | 13.9 |
| Munich, Germany | 9.9 | Seattle, Washington | 11.5 |
| Naples, Italy | 15.6 | Washington, D.C. | 12.2 |
| Paris, France | 10.5 | **Canada** | |
| Prague, Czech Republic | 9.2 | Calgary, Alberta | 3.6 |
| Rome, Italy | 15.0 | Edmonton, Alberta | 2.9 |
| St. Petersburg, Russia | 4.5 | Montreal, Quebec | 6.5 |
| Stockholm, Sweden | 5.8 | Quebec City, Quebec | 4.3 |
| Turin, Italy | 14.0 | Toronto, Ontario | 7.6 |
| Vienna, Austria | 9.4 | Vancouver, British Columbia | 9.8 |
| Warsaw, Poland | 7.4 | Winnipeg, Manitoba | 2.0 |

Table 2.2: Thermal properties of selected materials (Harris, 1995)

| Material | Thermal Conductivity, $k_T$ (W/mK) | Volumetric Heat Capacity, $C_v$ ($MJ/m^3K$) |
|---|---|---|
| Water | 0.602 | 4.18 |
| Ice | 2.22 | 1.93 |
| Air | 0.024 | 0.00126 |
| Quartz | 8.4 | 1.9 |
| Many soil minerals | 2.9 | |
| Organic Soil | 0.25 | 2.5 |
| Limestone | 1.7-2.9 | 2.4-4.2 |
| Dolomite | 5.02 | 2.51 |
| Sandstone | 1.8-4.2 | 2.51 |
| Shale | 1.5 | 1.84 |
| Quartzite | 4.5-7.1 | |
| Concrete | 1.3-1.7 | |

Table 2.3: Maximum pore pressure during triaxial compression (Moritz, 1995)

| Sampling Depth (m) | Test Temperature (°C) | Maximum excess pore pressure during triaxial compression test (kPa) |
|---|---|---|
| 6 | 40 | 13 |
| 6 | 40 | 15 |
| 9 | 70 | 27 |
| 9 | 70 | 35 |

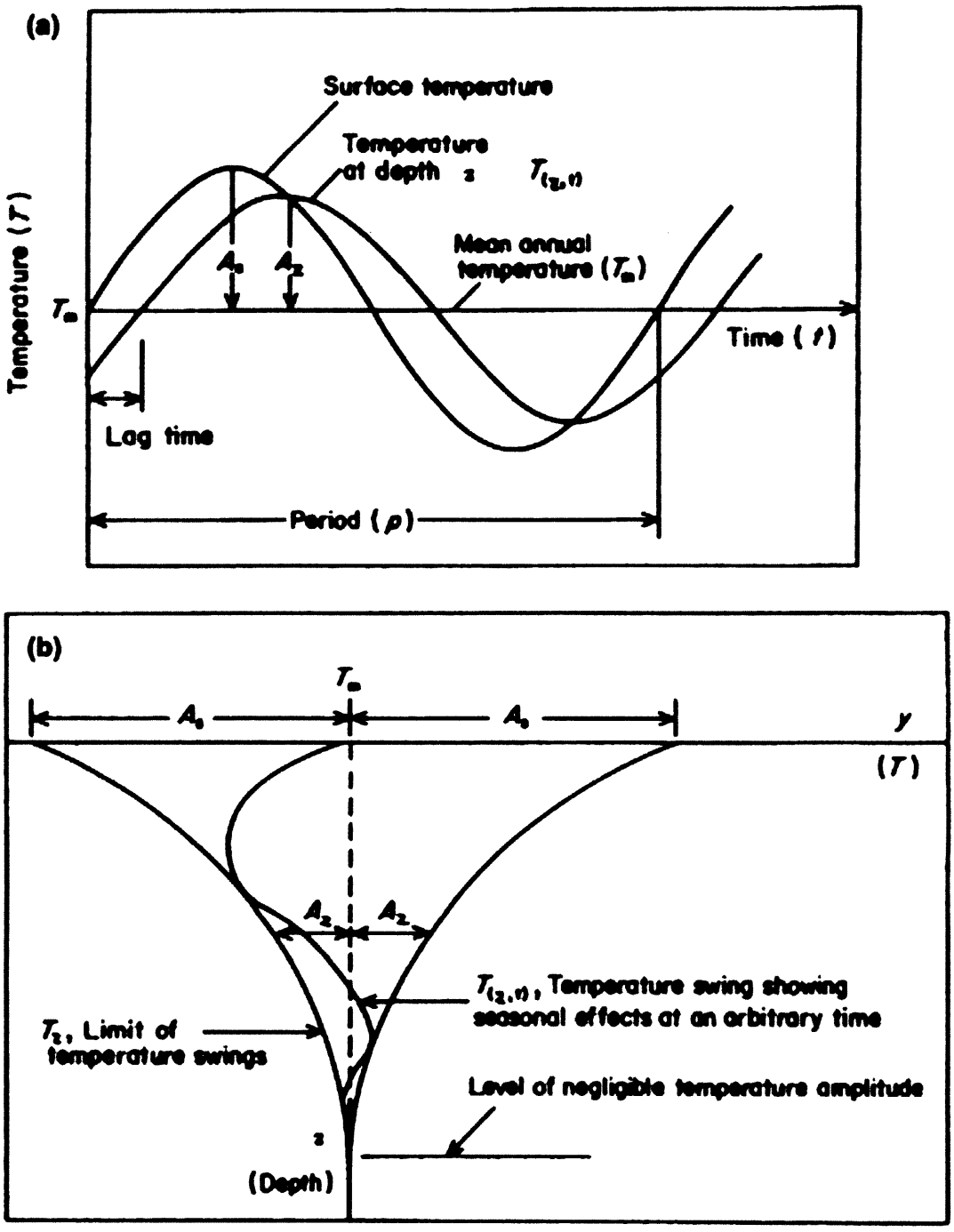


Figure 2.1: Surface and ground temperatures (a) seasonal variation (b) temperature penetration with depth (Andersland and Ladanyi, 2004)

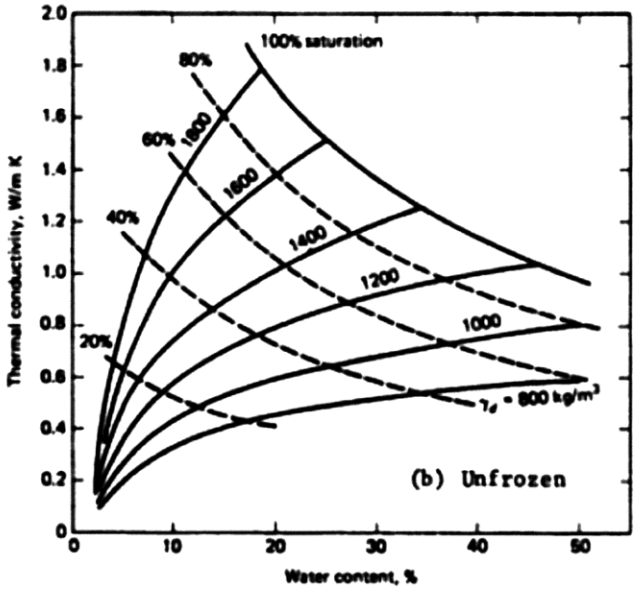


Figure 2.2: Average thermal conductivity of unfrozen silts and clays (Andersland and Ladanyi, 2004)

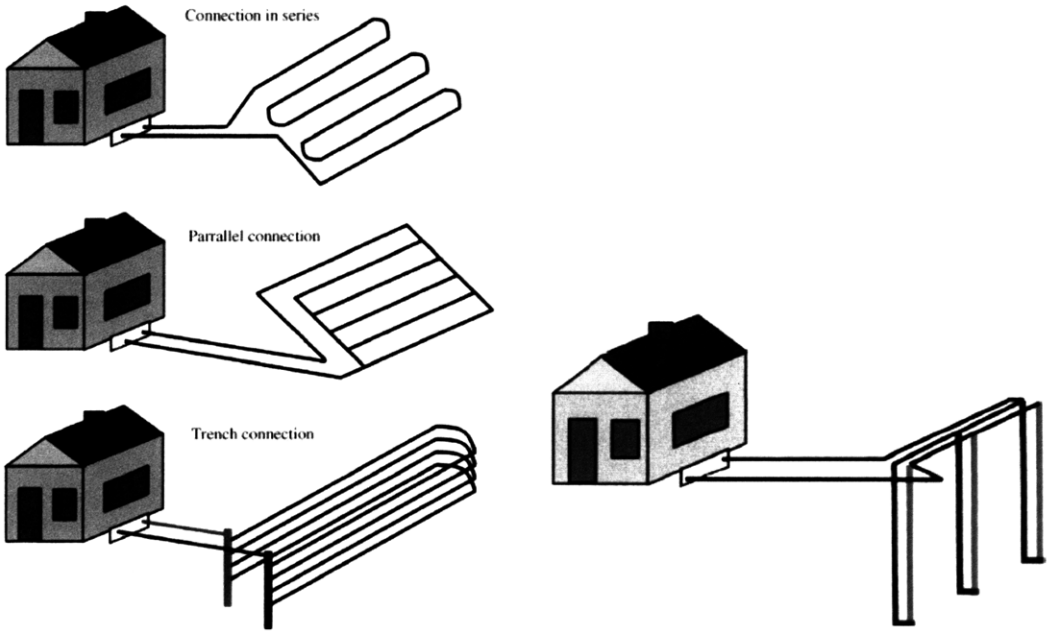


Figure 2.3: Ground heat exchangers (a) horizontal configurations, (b) vertical configuration (Florides and Kalogirou, 2007)

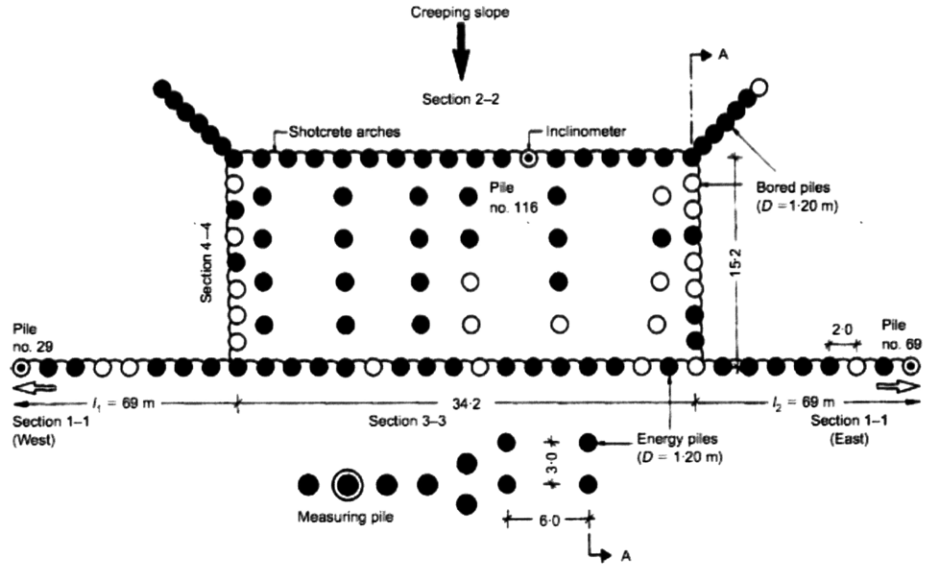


Figure 2.4: Location of energy piles (Black) and energy retaining walls in rehabilitation center (Brandl, 2006)

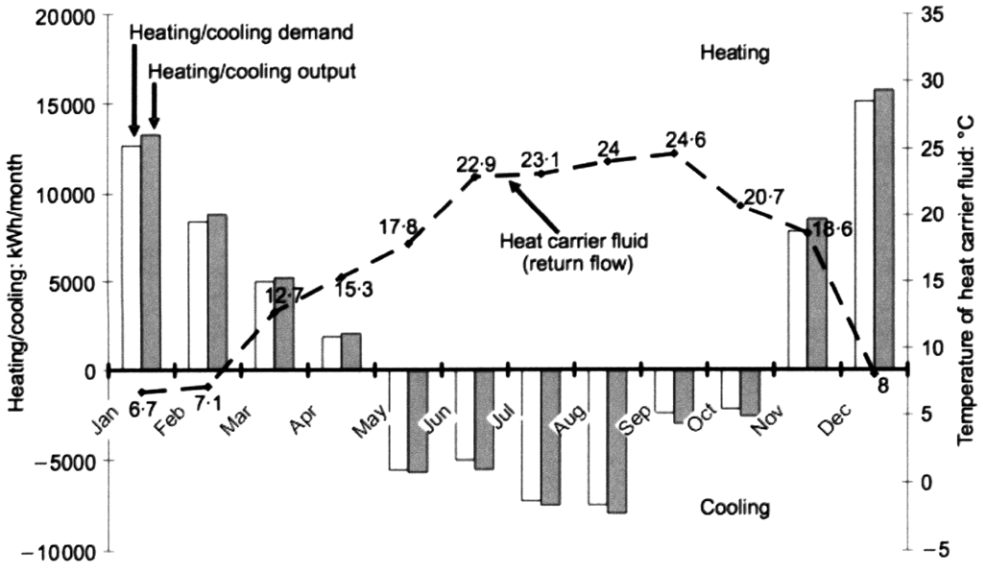


Figure 2.5: Annual energy demand and supply of rehabilitation center (Brandl, 2006)

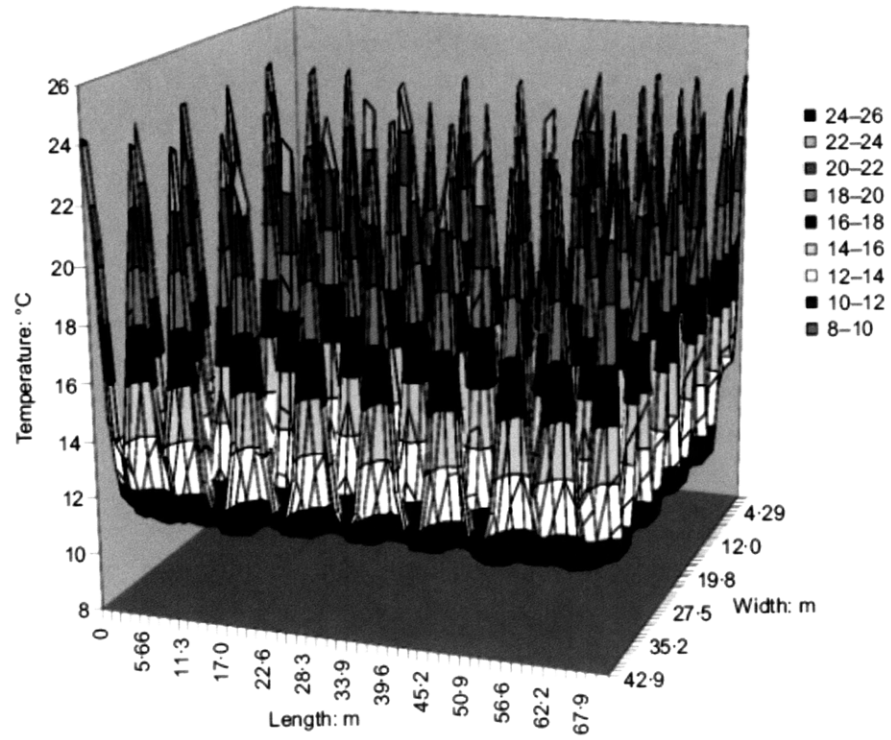


Figure 2.6: Numerical simulation of soil temperature around piles for cooling season (Brandl, 2006)

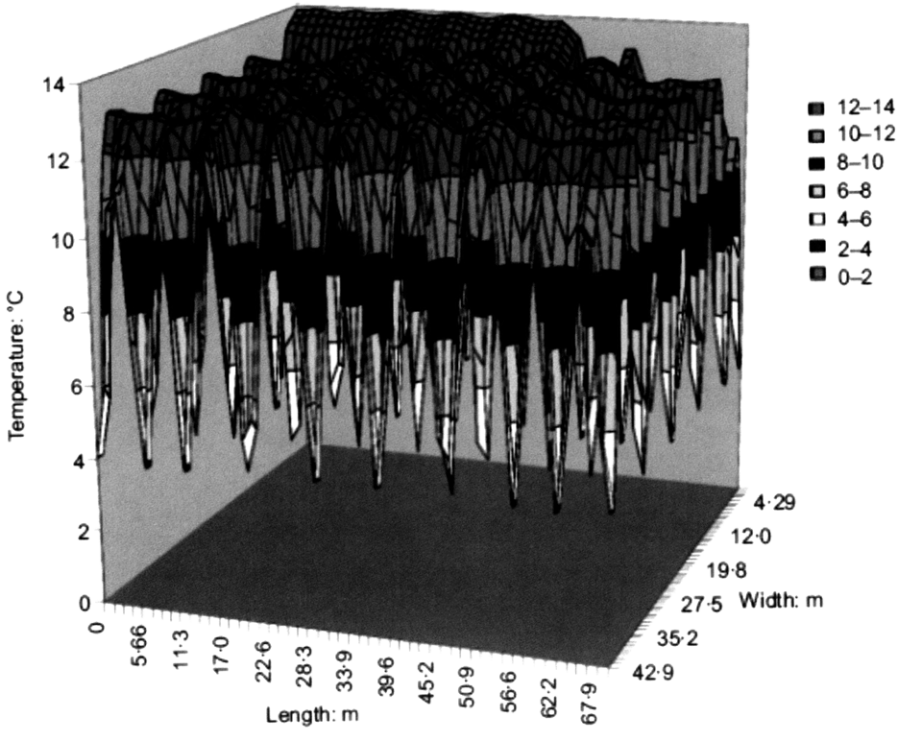

Figure 2.7: Numerical simulation of soil temperature around energy piles for heating season (Brandl, 2006)

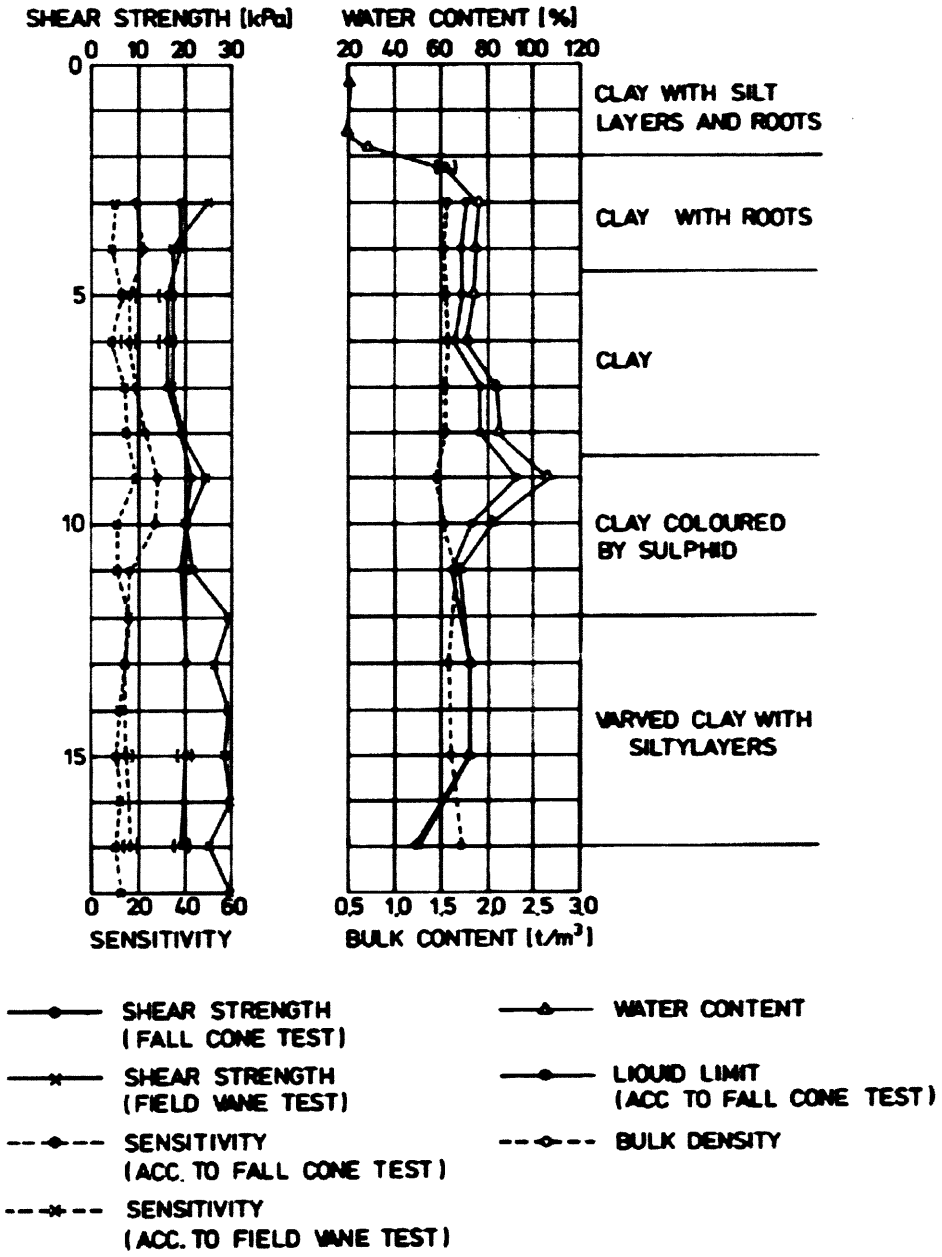


Figure 2.8: Soil profile of Swedish test field, Linkoping marina (Moritz, 1995)

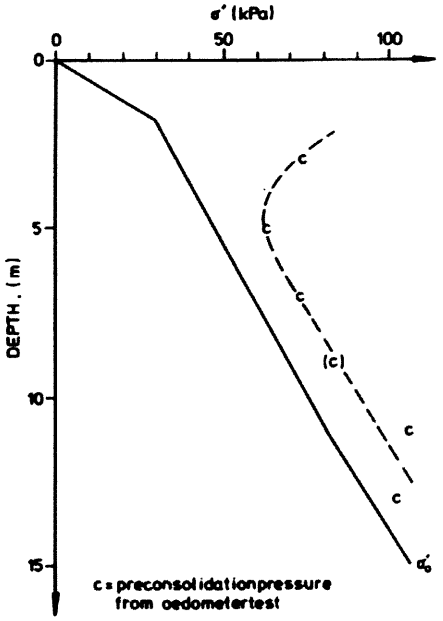


Figure 2.9: Preconsolidation pressure versus depth of Swedish test field (Moritz, 1995)

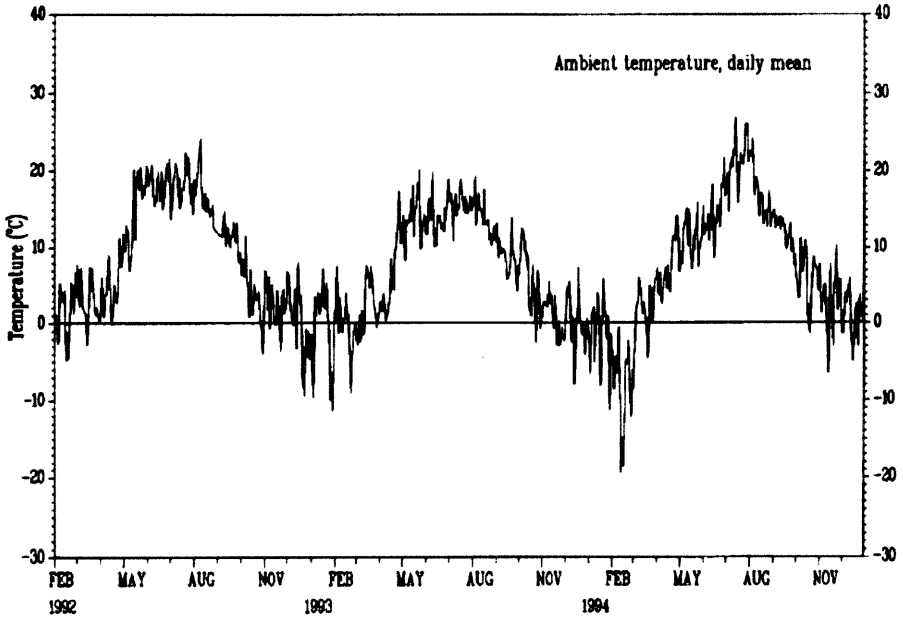


Figure 2.10: Daily mean air temperature for test field (Gabrielsson et al., 1997)

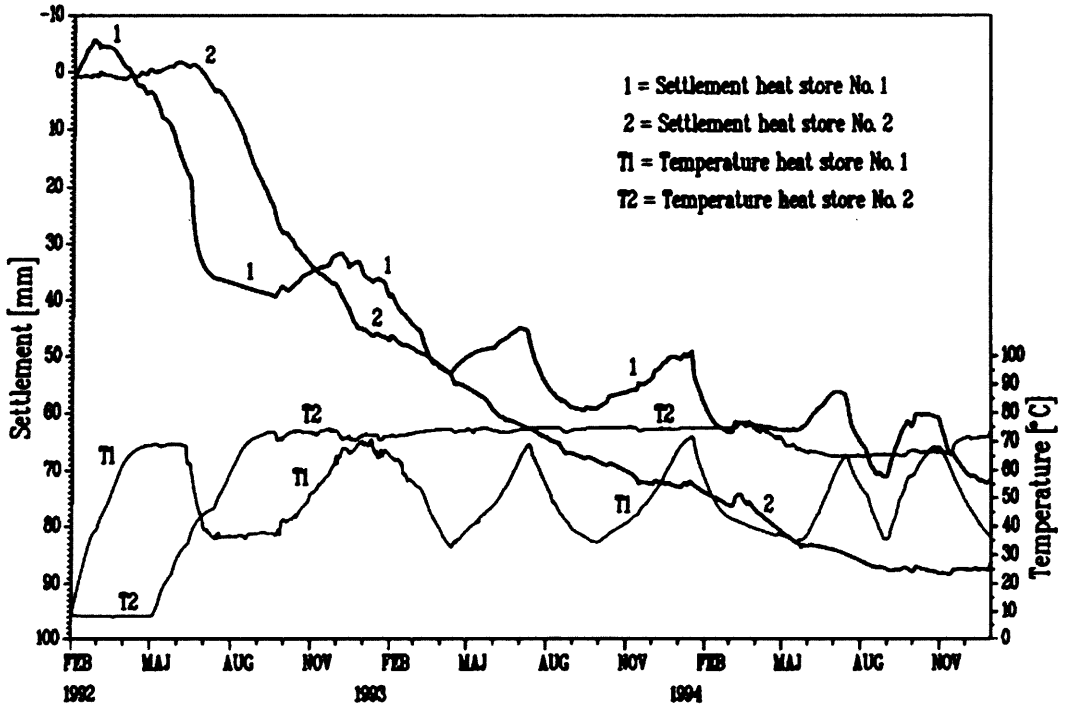


Figure 2.11: Temperature and total settlement at center of heat stores 1 and 2 (Gabrielsson et al., 1997).

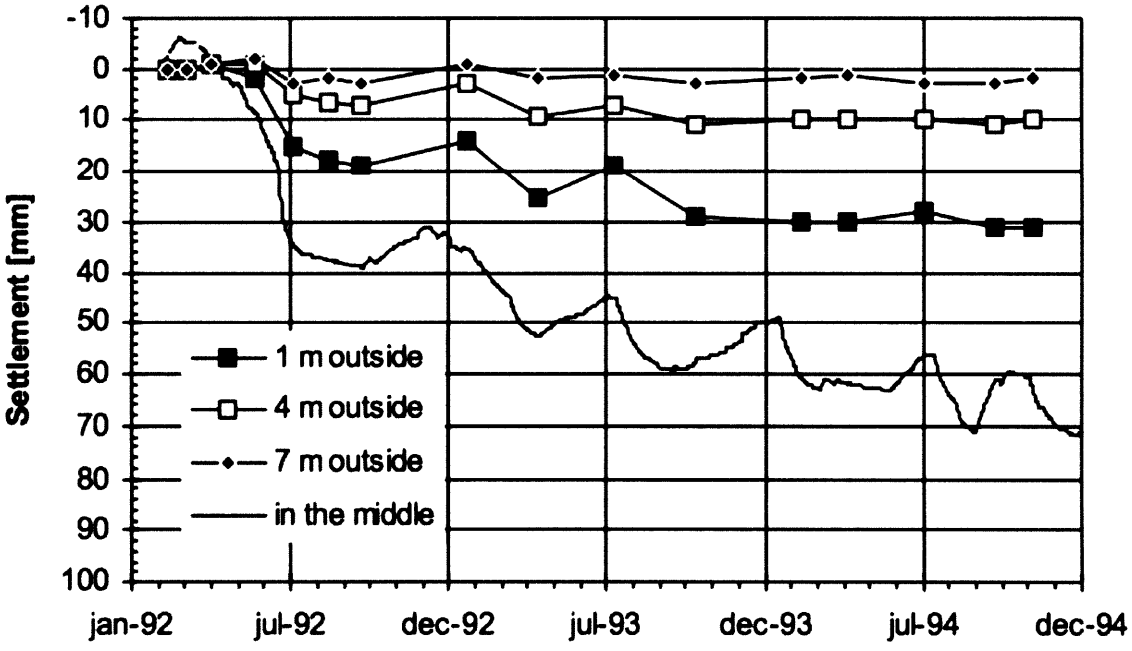


Figure 2.12: Settlement of ground surface at center and outside heat Store 1 (Gabrielsson et al., 1997)

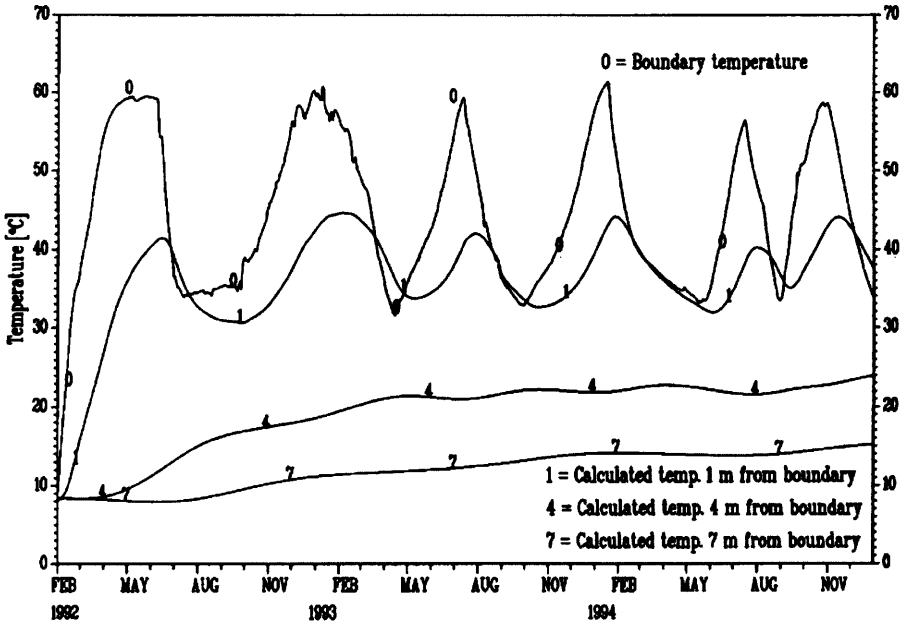


Figure 2.13: Temperature at 6 mBGS outside heat store with varying temperature. (Gabrielsson et al., 1997)

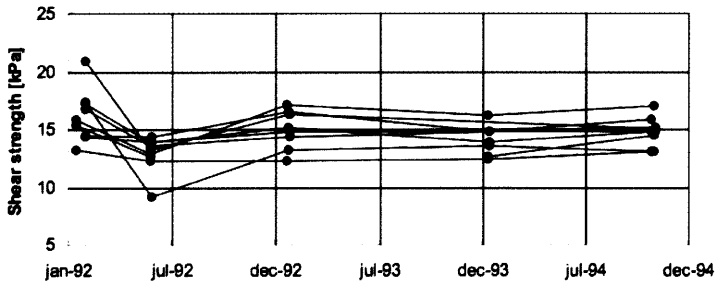


a) Store 1

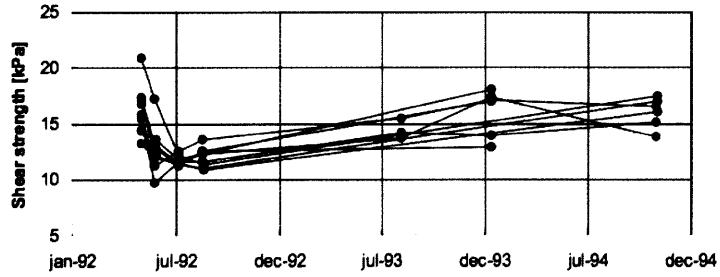


b) Store 2

Figure 2.14: Results of shear strength tests (Gabrielsson et al., 1997)

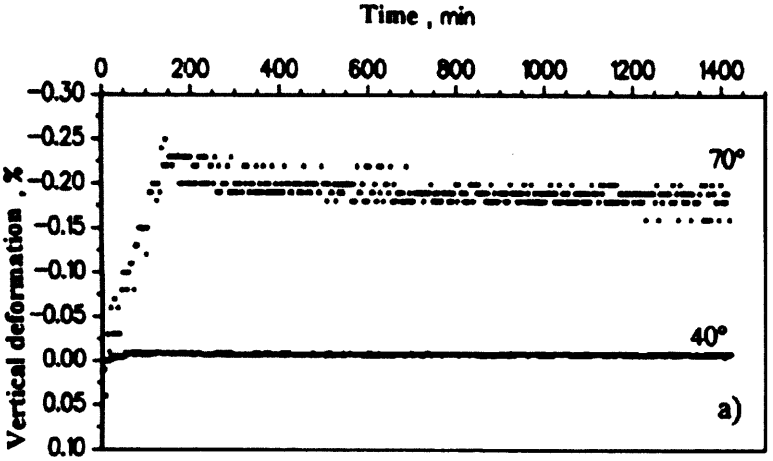


Figure 2.15: Deformation of Sample from 6 mBGS upon undrained heating (Moritz, 1995)

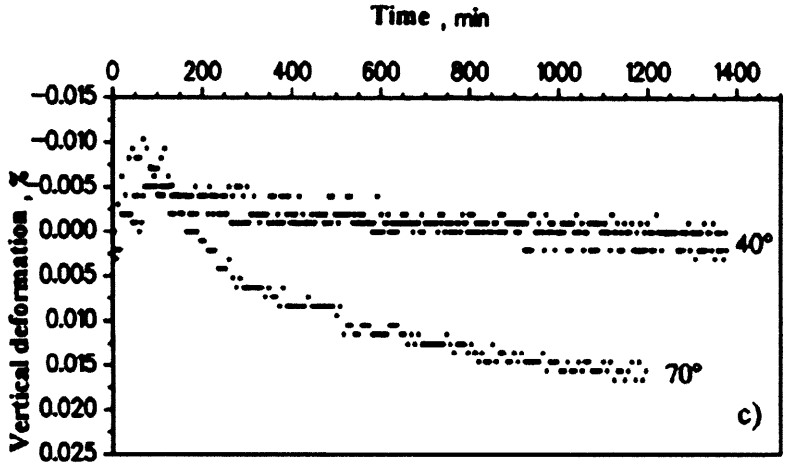


Figure 2.16: Deformation of sample from 9 mBGS upon undrained heating (Moritz, 1995)

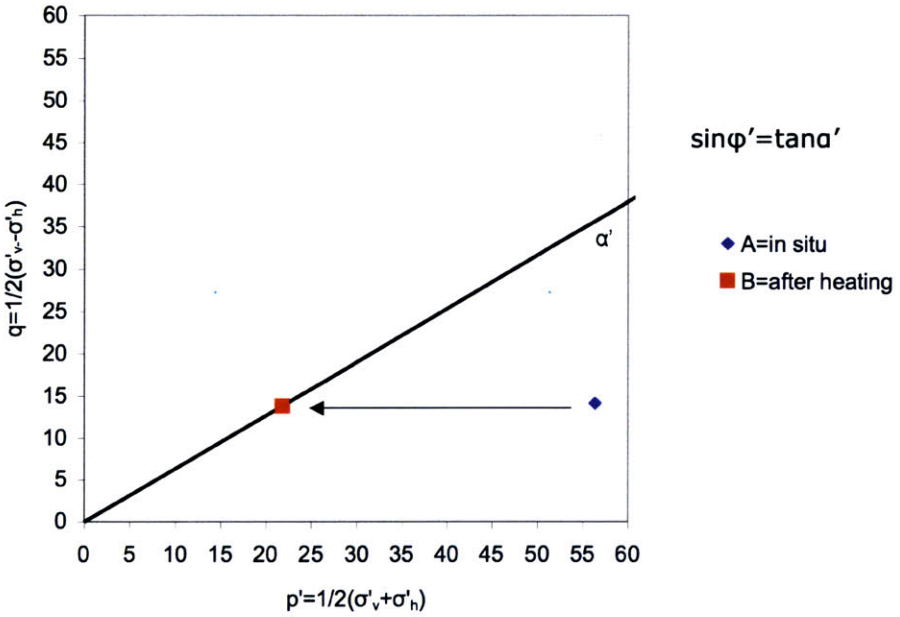


Figure 2.17: The stress path of sample from 9 mBGS during heating to 70°C (after Moritz, 1995)

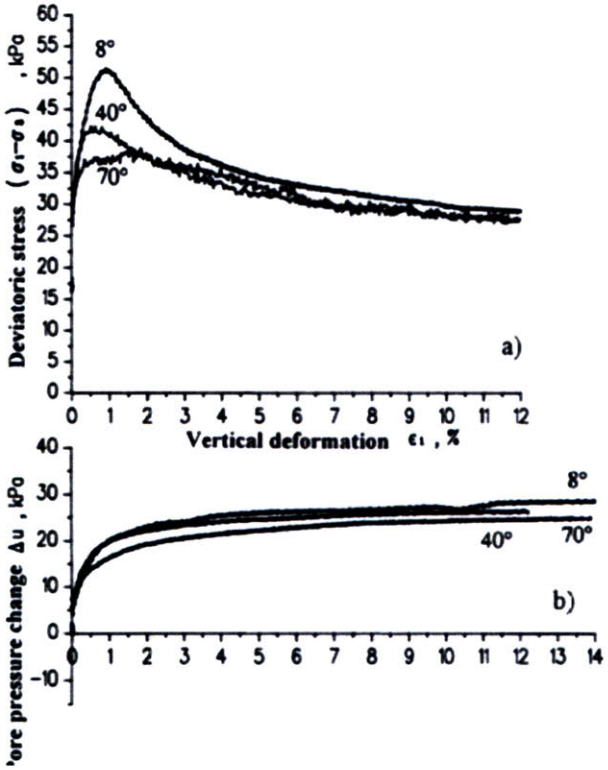


Figure 2.18: Results of slow undrained triaxial test on sample from 6 mBGS (Moritz, 1995)

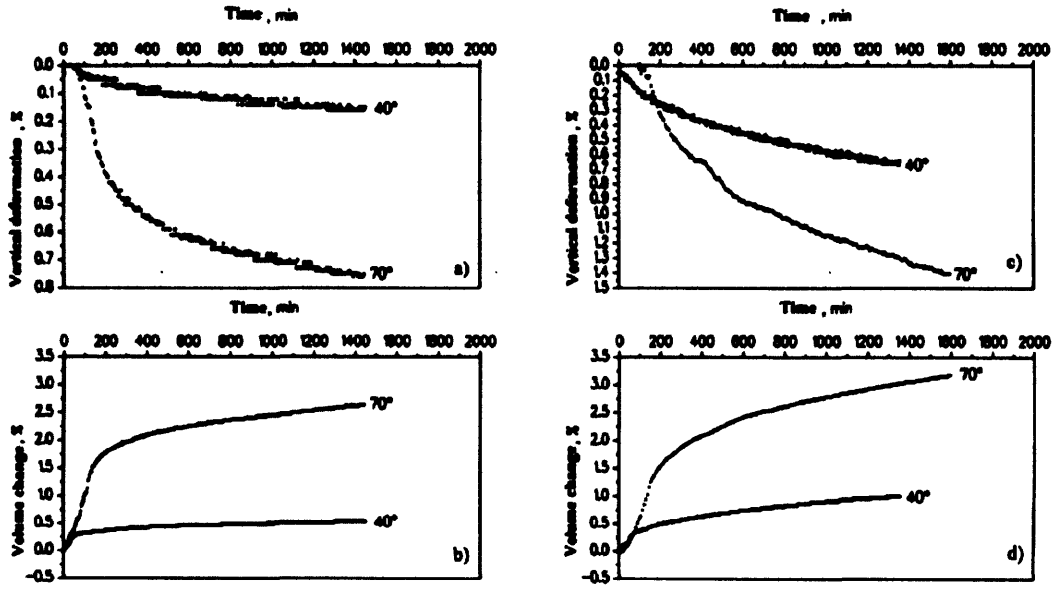


Figure 2.19: Vertical deformation and volume change under drained conditions (right: sample from 6mBGS, left: sample from 9 mBGS) (Moritz, 1995)

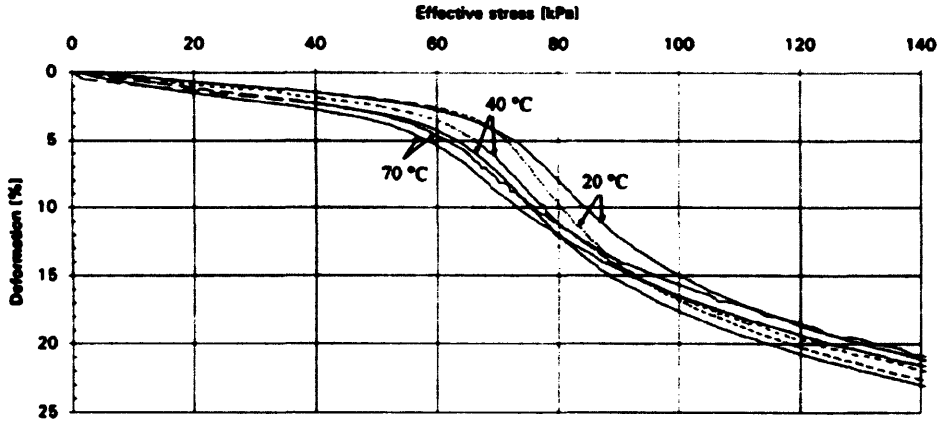


Figure 2.20: 1-D compression data from Lingkoping Clay, samples from 6mBGS (Moritz, 1995)

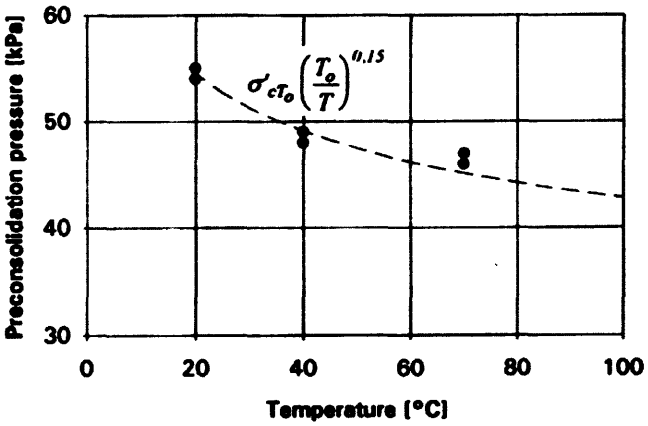


Figure 2.21: Change in preconsolidation stress with temperature of clay from Lingkoping, Sweden from 6 mBGS (Moritz, 1995)

# 3 MEASUREMENT AND MODELING OF THERMO-MECHANICAL PROPERTIES OF CLAYS

## 3.1 Measured Behavior

The application of ground heat exchange necessitates an in-depth analysis of heat-induced deformations in clays. Soft clays are particularly sensitive to temperature changes. Temperature induced changes in overconsolidated soils are generally very small and reversible, but these same temperature-induced changes in soft soils are non-trivial. A 12 °C change in temperature of a soft clay typically leads to a 10% change in undrained shear strength and preconsolidation pressure (Leroueil and Marques, 1996). An increase in soil temperature has two fundamental consequences: 1) the thermal expansion of the solid particles and pore water, and 2) a modification in the strength of the contacts between the solid particles (Leroueil and Marques, 1996).

### 3.1.1 Compression and Consolidation Properties

Temperature and strain rate both influence the viscous behavior of natural clays. A change in either the temperature or the strain rate at which clay is tested will result in a change in the apparent preconsolidation and compression characteristics of the clay. At higher temperatures, clay has a smaller apparent preconsolidation and is more compressible; a normally consolidated sample develops apparent overconsolidation behavior when cooled (Leroueil and Marques, 1996).

Increasing the rate of strain produces similar shifting in the stress-strain curve as decreasing the temperature and hence both effects are related to viscous properties of the

clay. Boudali et al (1994) performed a number of CRS tests on Berthierville Clay at different temperature and strain rates. Figure 3.1 shows four such CRS tests, including two overlapping tests that were run at T=5°C and strain rate, $\dot{\varepsilon} = 1.6\text{x}10^{-7}\ s^{-1}$ and T=35°C and strain rate, $\dot{\varepsilon}$ = of $1.6\text{x}10^{-7}\ s^{-1}$. At a constant strain rate, the lower the temperature, the higher the effective stress in the soil at a given strain. At a constant temperature, the higher the strain rate, the larger the effective stress at a given strain (Boudali et al., 1994). In the construction and operation of a ground energy storage system, the influence of strain rate is not of particular importance; the thermal loads do not affect the rate of any mechanical loads that are applied to the soil.

In drained conditions, an increase in temperature is associated with an expulsion of pore water and therefore a reduction in void ratio, leading to thermally induced consolidation. The net effect is an inelastic particle rearrangement in normally and lightly overconsolidated soils, resulting in irrecoverable deformations (Leroueil and Marques, 1996). Normally consolidated and lightly overconsolidated clays consolidate when heated, whereas highly overconsolidated clays first dilate and then contract. The amount of dilation/contraction depends on the overconsolidation ratio (OCR) of the clay and the magnitude of the temperature change (Laloui and Cekerevac, 2003). Figure 3.2 shows a summary of the relationship of the volumetric strain to OCR for a range of different clays and applied increments of temperature. The effect of temperature on clay changes from compressive to dilative at approximately OCR=2.

Temperature has a significant effect on the compressibility of clay. As temperature increases, the apparent preconsolidation pressure decreases and larger strains develop at a given level of effective stress. Figure 3.3 shows the shift of the compression curve and the decrease in preconsolidation pressure with increasing temperature. In NC and lightly OC clays, the creep rate increases at higher temperatures. (Leroueil and Marques, 1996), as demonstrated in Figure 3.4. Towhata et al, (1993) found that the rate of consolidation increases dramatically upon heating.

#### 3.1.1.1 Changes in Pre-consolidation Pressure

It has repeatedly been found that the apparent preconsolidation pressure decreases with increasing temperature. Leroueil and Marques (1996) found that the decrease in preconsolidation pressure with increasing temperature averages 1%/°C between 5 and 40°C. Figures 3.5 shows a compilation of the preconsolidation pressure versus temperature relationships found in the literature. In the overconsolidated range, the vertical strain generated by a temperature change of 30 °C is a relatively small 0.5%. However, in normally consolidated samples, a temperature change of 30°C can have significant effect on compressibility. In these clays, at constant strain rate, the lower the temperature, the higher the effective stress at a given strain or void ratio (Leroueil, 1996)

### 3.1.2 Shear Strength

Clays have also been known to experience thermal shear failure at elevated temperatures during undrained heating. According to Hueckel et al. (2009), thermal failure may be due to:

- Differential thermal expansion rates of clay minerals and water;
- Mineral debonding, and;
- Changes in adsorbed water.

In undrained conditions, heating leads to an increase in pore pressure, resulting in a decrease in effective stress (and undrained strength); the undrained response has been found to be elastic (i.e. reversible) for both normally and overconsolidated clay (Leroueil and Marques, 1996). Hueckel et al. (2009) discuss the phenomenon of thermal failure and present a cross-section of experiments on the topic. Figure 3.6 shows decreasing strength with temperature from triaxial tests performed on Spanish clay. The Spanish clay studied has a plasticity index between 18 and 28 percent, 13 percent carbonate content and friction angle $\phi$=29° (Hueckel et al., 1998). If the clay is loaded beyond its reduced

strength at elevated temperatures, failure will occur. For any construction that involves thermal loading, it is imperative to include the reduced clay strength at temperature in load bearing calculations (Hueckel et al., 2009). However, Leroueil and Marques (1996) hypothesize that, when the temperature increase is accompanied by a significant decrease in void ratio, the strength gain due to the lower void ratio compensates for the strength lost at the higher temperature. The effect of temperature changes on the strength of clay varies significantly from one clay to the next, depending on mineralogy, temperature, stress history and OCR. Different clays exhibit very different behavior under the same thermal loads. At present, there is no unifying theory to predict the sensitivity of clay strength to thermal loading (Hueckel et al., 2009).

## 3.2 Models of Thermo-Mechanical Coupling in Clay

There have been a number of attempts to model the deformations and changes in shear strength that occur in clay upon heating. In the 1980's, thermo-elasticity was used to model the effects of temperature on pore pressure and consolidation (e.g., Britto et al., 1992). However, thermo-elastic models are unable to simulate the irreversible effects of heating. To simulate these irreversible effects of temperature on clay, a thermo-elastic-plastic model is needed (Graham et al 2001). Numerous researchers have made modifications to the Modified Cam Clay (MCC; Roscoe and Burland, 1968) model to try to match the behavioral changes seen in clay upon temperature change. This chapter will summarize a number of the approaches taken towards creating "Thermal Cam Clay". The Modified Cam-Clay (MCC) model itself will not be expanded upon here. The MCC model is generally believed to be best suited to normally consolidated and lightly over-consolidated clays; the accuracy of the model is significantly reduced when dealing with highly overconsolidated soils. Since this paper is primarily concerned with the effects of heating on normally and lightly overconsolidated soils, this limitation is reasonable.

The distinctive feature of all Thermo-Cam-Clay models is the dependence of the yield surface on temperature. All Thermo-Cam-Clay models add a thermal term to the

deformation of the yield surface. As temperature increases, the yield surface contracts leading to a reduced OCR. The following summarize a number of Thermo-Cam-Clay models presented in the literature.

### 3.2.1 Hueckel and Borsetto (1990)

Hueckel and Borsetto based their thermal-mechanical clay model on the "Critical state soil mechanics" concepts presented by Schofield and Wroth (1968). The critical state model is made up of an elastic region, a yield surface, a plastic flow rule and a hardening law. Figure 3.7 shows a schematic of the Hueckel and Borsetto model, and illustrates how the yield surface contracts with increasing temperature.

Since the preconsolidation pressure of clay, and by extension the yield surface, changes with temperature, the equation of the yield surface is dependant on stress, volumetric strain and temperature. The yield surface in triaxial shear space can be written as:

$$f = f(p',q,\varepsilon_v^{tp},\Delta T) \tag{3.1}$$

where:

$$\Delta T = T - T_0 \tag{3.2}$$

$$p' = \frac{\sigma_1' + 2\sigma_3'}{3}$$

$$q = \sigma_1' - \sigma_3' \tag{3.3}$$

$\varepsilon_v^{tp}$ is the thermoplastic volumetric strain, p' and q are the mean effective stress and deviator stress, respectively.

Hueckel and Borsetto (1990) assume the elastic strain components are independent of temperature. Their model used a non-associated flow rule for thermoplastic strain.

$$\varepsilon_v^{tp} = \frac{1}{3}\Lambda_v \frac{\partial g}{\partial p'} \tag{3.4}$$

$$\varepsilon_s^{tp} = \frac{3}{2}\Lambda_s \frac{\partial g}{\partial q} \tag{3.5}$$

where g is the plastic potential surface, $\Lambda_v$ and $\Lambda_s$ are plastic multipliers.

$$g = g(p', q, \varepsilon_v^{tp}, \Delta T) \tag{3.6}$$

$$\Lambda_v = \frac{\left(\frac{\partial f}{dq}\right)\dot{q} + \left(\frac{\partial f}{dp'}\right)\dot{p}' + \left(\frac{\partial f}{dT}\right)\dot{T}}{H} \tag{3.7}$$

$$\Lambda_q = \Lambda_v + \frac{f_1}{H}\dot{T} \tag{3.8}$$

Where H is the thermoplastic hardening modulus

$$H = -\frac{\partial f}{\partial \varepsilon_v^{tp}} \frac{\partial g}{\partial p'} \tag{3.9}$$

$$f_1 = -\frac{\partial f}{\partial T} + f_{1T}\left(\Delta T, p', q, \varepsilon_v^{tp}\right) \tag{3.10}$$

Therefore, unloading occurs when one of two conditions are met:

1) $f < 0$

2) $f = 0$ and $\frac{\partial f}{dq}\dot{q} + \frac{\partial f}{dp'}\dot{p}' + \frac{\partial f}{dT}\dot{T} < 0$ with $\Lambda_v = 0$

Loading occurs when:

$f = 0$ and $\dot{f} = 0$ at $\Lambda_v > 0$

This thermo-plastic model satisfactorily replicates features measured in laboratory element tests. The yield surface shrinks with an increase in temperature, known as thermal softening. Since cooling leads only to an elastic response, the heating-cooling

cycle leads to a consolidation of the clay, as seen in experiments (Hueckel and Baldi, 1990). Figures 3.8 and 3.9 show two different stress paths, starting at OCR 12.5 and 5 at 20°C and 90°C, and their results. These Figures show that this model is consistent with the reduction in peak shear strength seen experimentally.

Based on their constitutive and experimental results (Hueckel and Borsetto, 1990 and Hueckel and Baldi 1990), the following formula was proposed for the yield surface:

$$p_c = p_{c0}\exp\left(\frac{1}{\lambda - H_T}\left\{e_1 - (1-a_0\Delta T)\left[e_g - (1+e_0)\varepsilon_v^{tp}\right]\right\}\right) + 2\left(a_1\Delta T + a_2\Delta T|\Delta T|\right) \qquad (3.11)$$

where

$$H_T = \left[\frac{H_i}{1+e_0} + (\alpha_1 + \alpha_2\Delta T)\Delta T\right](1+e_0) \qquad (3.12)$$

$$e_g = \frac{1}{a_0\Delta T_g - 1}\left(\left(\lambda - K_{Tg}\right)\ln\left\{\left[p_c' - 2\left(a_1\Delta T_g + a_2\Delta T_g|\Delta T_g|\right)\right]\frac{1}{p_{co}}\right\} - e_1\right) \qquad (3.13)$$

$\alpha_1$ and $\alpha_2$ are temperature constants controlling the reduction of the yield surface

$e_0$ = the void ratio at the initial state

$e_1$= the void ratio at $p'_{co}$

$p'_g$, $q_g$ and $e_g$ are the stress in the geostatic state and void ratio for geostatic conditions

$T_g$=the insitu temperature of the ground

Figure 3.9 illustrates the behavior of the model at 20°C and 90°C. Hueckel and Baldi (1990) found this model to be reasonably accurate at predicting clay behavior during thermoplastic consolidation, thermo-mechanical undrained failure due to heating, thermal ductilization of clay during triaxial compression and cyclic temperature loading. Figure 3.10 compares the predictive power of this model to experimental data during a drained heating and cooling cycle of NC Boom Clay, repeated by Senevirantne (1993). For the comparison, two types of analysis were run: (A) used a constant value of the coefficient of thermal expansion, $\alpha$, of the soil and (B) used a linearly decreasing value of the coefficient or thermal expansion with the stress ratio. Figure 3.11 summarizes further

predictions of pore pressure and axial strain response for constant volume heating of Boom Clay at constant shear stress. These results show that the model underestimates axial strains due to heating. While linearly variable thermal expansivity is needed to accurately simulate pore pressure.

## 3.2.2 Picard Model (1994)

The Picard model was developed at the l'Ecole Nationale des Ponts et Chaussees in France as part of the Doctoral Thesis by Picard (1994). The model has been programmed into the commercial finite element modeling software CESAR-LCPC.

The Picard (1994) Model is similar to the formulation by Hueckel and Borsetto's (1990) presented above, but presents a number of simplifications.

The yield surface is defined as a function of stress state and preconsolidation pressure, (p',q, $p_c$), while preconsolidation pressure, $p_c$, is a hardening parameter dependent on temperature.

$$f(p',q,p_c) = p'(p' + p_c) + \left(\frac{q}{M}\right)^2 \qquad (3.14a)$$

$$p_c = p_{co}\exp\left(-v\left(\varepsilon_v^p + 3\alpha_p \Delta T\right)\right) \qquad (3.14b)$$

where:

$p_{co}$ is the preconsolidation pressure at the reference temperature, $T_o$

$\alpha_p$ is the coefficient of plastic thermal dilation

$v$ is the elastic-plastic parameter, $v = \frac{1+e_0}{\lambda-\kappa}$

$\Delta T$ is the change in temperature

The ability of the model to predict clay behavior depends on the selection of $\alpha_p$ to match lab behavior (Picard, 1994). Figures 3.12 and 3.13 show the ability of the Picard model to predict deformation of Boom Clay with temperature. Picard found that using the value of $v$ calculated from the measured, $\lambda$, $\kappa$, and $e_o$ did not always produced accurate results. Figure 3.12, with v=12.6, shows the deformation predicted using the measured Boom Clay properties, $e_0$, $\lambda$ and $\kappa$. In this case, the model provides reasonable predictions for p'=1 MPa where the behavior is approximately elastic (very small irrecoverable strain) and at 6 MPa (large plastic compression). However, there are large discrepancies in the prediction for the intermediate state where p'=3 MPa.

By increasing the coefficient of thermal hardening to $v$= 30 in Figure 3.13, it was possible to better predict inelastic behavior during heating of the clay at 3 MPa. This divergence of $v$ from the measured $e_0$, $\lambda$ and $\kappa$, increased the accuracy of shear strains in drained shear tests but generates error in the 1-D consolidation behavior (Picard 1994). Figure 3.14 shows the effect of changing V on predictions of 1-D incremental and oedometer test of Boom Clay. (Picard, 1994).

### 3.2.3 Robinet et al (1996)

Robinet et al, (1996) presented a thermomechanical model for non-expansive clays, (e.g. kaolinite) with two plastic mechanisms; 1) a mechanical yield surface based on Modified Cam-Clay, $f_{Tm}$, and (2) a thermal yield surface, $f_T$.

The thermal yield surface, $f_T$, defines a place between two temperature ranges. When the temperature is less than the threshold temperature, $T_c$, thermal strains are reversible, and beyond $T_c$ there are both reversible and irreversible strains (Robinet et al., 1996).

$$f_T = T - T_c = 0 \qquad (3.15)$$

The total thermal volume strain is made up of both the reversible and irreversible components.

$$\dot{\varepsilon}_{TV}^{t} = \dot{\varepsilon}_{TV}^{r} + \dot{\varepsilon}_{TV}^{ir} \tag{3.16}$$

where

$$\dot{\varepsilon}_{TV}^{r} = -\frac{\alpha}{3}\dot{T}\delta_{ij} \tag{3.17a}$$

$$\dot{\varepsilon}_{TV}^{ir} = -a_T b_T \eta \exp(-b_T T)\dot{T} \text{ if } T=T_c \text{ and } \dot{T} > 0 \tag{3.17b}$$

$\alpha$ is the coefficient of thermal expansion of the skeleton and water, and $a_T$ and $b_T$ are thermal parameters of the clay.

The expansion of the system due to temperature change alone is often ignored, since it is likely to be much smaller than any mechanical effects. Robinet et al (1995) found that this expansion sometimes plays a very important role in the thermo-mechanical behavior of clays. This consideration of irreversible thermal strains is the main difference between this model and the one put forward by Hueckel and Borsetto (1990), discussed above.

The mechanical yield surface, $f_{Tm}$, was developed based on generalized mechanisms of Modified Cam-Clay (Roscoe and Burland, 1968).

$$f_{Tm}(p',q,p'_{cT}) = q^2 - M^2\gamma^2 p'(bp'_{cT} - p')R^2(\Theta) \tag{3.18}$$

where $R(\Theta)$ is a function of the lode angle

$$p'_{cT} = p'_{co}\exp\left(v\varepsilon_{mv}^{p}\right)\exp\left(\beta_T \varepsilon_{Tv}^{ir}\right) \text{ if } T=T_c \text{ and } \dot{T} > 0 \tag{3.19}$$

$\varepsilon_{mv}^{p}$ is the volumetric plastic strain

$$v = \frac{1+e_o}{\lambda-\kappa}$$

$\beta_T$ is the coefficient of thermoplastic compressibility

$\varepsilon_{dTm}^{p}$ is the thermo-mechanical deviator strain

$\gamma$ is a deviatoric strain hardening parameter $\gamma = \frac{\varepsilon_{dTm}^{p}}{a + \varepsilon_{dTm}^{p}}$, a, b are the Hujeux parameters.

The parameter $R(\Theta)$ describes the generalization of the yield surface to account for difference in Code Angle, $\theta$.

$$R(\Theta) = \frac{\sqrt{3}}{2} \frac{M_E / M_c}{\left(1 + M_E / M_c\right)\sin\left(\Theta - \frac{\pi}{6}\right) + M_E / M_c \sqrt{3}\sin\Theta} \tag{3.20}$$

$$M_c = \frac{6\sin\phi}{(3 - \sin\phi)}; M_E = \frac{-6\sin\phi}{(3 + \sin\phi)} \tag{3.21}$$

Figure 3.15 shows a comparison of the predictions made by the Robinet et al. (1995) model and experiments run by Baldi et al. (1990). The model is able to well predict the experimental behavior at both 23 and 95°C. Figure 3.16 shows the theoretical stress path for this test and illustrates the uniqueness of this model, the thermal yield condition, $f_T$.

### 3.2.4 ACMEG-T (2008)

Since the 1980's, several large-scale tests have been conducted in Mol, Belgium with the goal of better understanding the effects of heat transfer from the deep burial of nuclear waste containers. The ACMEG-T constitutive model was used to simulate one of these tests, ATLAS: Admissible Thermal Loading for Argillaceous Storage (François et al., 2008).

In ACMEG-T, the thermo-mechanical process is defined through 2-coupled mechanisms: 1) an isotropic mechanism, and 2) a deviatoric plastic mechanism. Figure 3.17 illustrates these two yield mechanisms.

$$f_{iso} = p' - p'_c r_{iso} \tag{3.22}$$

$$f_{dev} = q - Mp'\left(1 - b\ln\frac{p'd}{p'_c}\right)r_{dev} = 0 \tag{3.23}$$

$b$ and $d$ are constants that govern the shape of the deviatoric yield limit.

ACMEG-T differs from the other models discussed here in that M, the slope of the critical state line, depends on temperature.

$M = M_o - g(T - T_o)$ where $g$ defines the evolution of M with temperature and $M_o = \frac{6\sin\phi'_o}{3-\sin\phi'_o}$

As in the other models discussed, the preconsolidation pressure is dependant on temperature.

$$p'_c = p'_{c0TO}\exp\{\beta\varepsilon_v^p\}\left\{1-\gamma_T \log\left[T/T_o\right]\right\} \quad (3.24)$$

where

$p'_{c0T0}$ is the value of the preconsolidation pressure at the reference state and temperature, $T_0$.

$\beta$ and $\gamma_T$ are material properties.

$r_{iso}$ and $r_{dev}$ correspond to the degree of mobilized plasticity

$$r_{iso} = r^e_{iso}\frac{\varepsilon^p_{iso}}{c+\varepsilon_v^{p,iso}} \quad (3.25)$$

where $c$ and $r^e_{iso}$ are material properties

$$r_{dev} = r^e_{dev} + \frac{\varepsilon^p_d}{a+\varepsilon^p_d} \quad (3.26)$$

where $a$ and $r^e_{dev}$ are material properties

$\varepsilon^p_d$ is the deviatoric plastic strain

ACMEG-T was used to predict the behavior of Boom Clay in an isotropic compression test. Figure 3.18 compares the ACMEG-T predictions to experiments by Baldi et al in 1991.

ACMEG-T was found to be effective at simulating both the temperature field around a hot buried object and the resulted changes in pore pressure. As Figures 3.18 and 3.19

show, ACMEG-T is able to reasonably replicate the clay's response under isotropic and thermal loading. It is worth noting that, in Figure 3.19, ACMEG-T was better able to replicate the volumetric strain induced by heating than the Picard model could under similar conditions (in Figure 3.12). However, the ACMEG-T model does not capture well the hysteresis behavior observed in isotropic loading and unloading (Figure 3.18).

### 3.2.5 Laloui et al (2008)

The models discussed above deal with the effects of temperature on the yield locus without including the effects of strain rate. As discussed in Section 3.11, an increase in strain rate expands the apparent yield surface, the opposite effect of an increase in temperature. Laloui et al. (2008) proposed a strain-rate temperature coupled model to simulate both the effects of temperature and strain-rate changes. For this model, the vertical yield stress is function of both strain rate and temperature:

$\sigma'_y = f\left(\dot{\varepsilon}_v^{vp}, T\right)$

where

$\dot{\varepsilon}_v^{vp}$ is the visco-plastic strain rate, and T is temperature

The formula developed for the vertical yield stress is:

$$\sigma'_{y\dot{\varepsilon},T} = \sigma'_{y\dot{\varepsilon},T_o}\left(\frac{\dot{\varepsilon}_v^{vp}}{\dot{\varepsilon}_{v0}^{vp}}\right)^{C_A}\left(1-\gamma\log\frac{T}{T_0}\right) \qquad (3.27)$$

where

$C_A = \dfrac{C_{\alpha e}}{C_c}$ is a soil parameter usually between 0.06 and 0.04 for non-organic clays

$\gamma$ is a soil parameter relating to the hardening of the yield surface with temperature change and usually varies between 0.10 for kaolin and 1.2 sand-bentonite mixture (Laloui et al, 2008)

Incorporating the dependence of the yield surface on strain rate and temperature, the yield limit equation becomes:

$$f = p' - \sigma_{y0} \exp\left(\beta \varepsilon_v^{vp}\right)\left(\frac{\dot{\varepsilon}_v^{vp}}{\dot{\varepsilon}_{v0}^{vp}}\right)^{C_A}\left(1 - \gamma \log\frac{T}{T_0}\right) \tag{3.28}$$

The model was tested by Laloui et al. (2008) for its ability to predict changes in the yield surface with temperature at constant strain rate and with changing strain rate at constant temperature. Figures 3.20 and 3.21 show a comparison of the simulations and experiments performed by Boudali et al (1994) on Berthierville Clay.

## 3.2.6 Selection of Model for Simulations

As interest has grown in the fields of nuclear waste burial, geothermal heating, energy foundations and the effect of temperature of sample disturbance, the utility of an accurate thermo-elasto-plastic model for clay has become apparent. Five such models have been summarized above. All of the models discussed were found by their authors to offer accurate predictions of the deformations of saturated clay when exposed to thermal stresses. No one model has emerged as dominant and none of them have been extensively tested to discover their strengths and weaknesses. The Hueckel and Borsseto (1990) model, by virtue of being the oldest, has received the most vetting and is most often referenced. However, as pointed out by Laloui et al. (2008), the model does not account for the effects of strain rate, which are similar and opposite to the effects of temperature on the yielding of a clay. More research is needed into the predictive power of thermo-elasto-plastic modeling.

For this thesis, the Picard (1994) model was used. The Picard model is available as part of the CESAR-LCPC platform. Its commercial availability was the primary reason for selecting this model. LCPC provides a copy of Picard's Doctorate Thesis "Ecrouissage Thermique des argiles saturees: Application au stockage de dechets radioactifs". The thesis provided background and verification data for the model. Picard's thesis, the

commercial availability of the software and support from LCPC made it possible to satisfactorily perform thermo-elasto-plastic modeling of ground deformations for heat exchangers installed in clay, as discussed in Chapter 4 and 5.

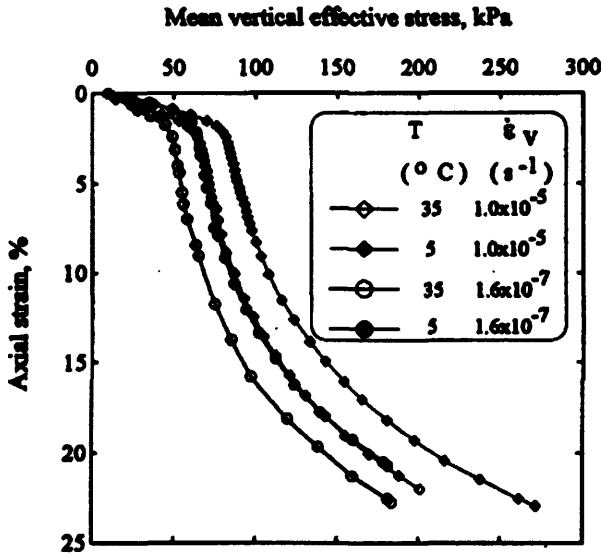


Figure 3.1: CRS consolidation test, showing effect of strain rate and temperature on 1-D compression behavior of Berthierville Clay. (Boudali et al., 1994)

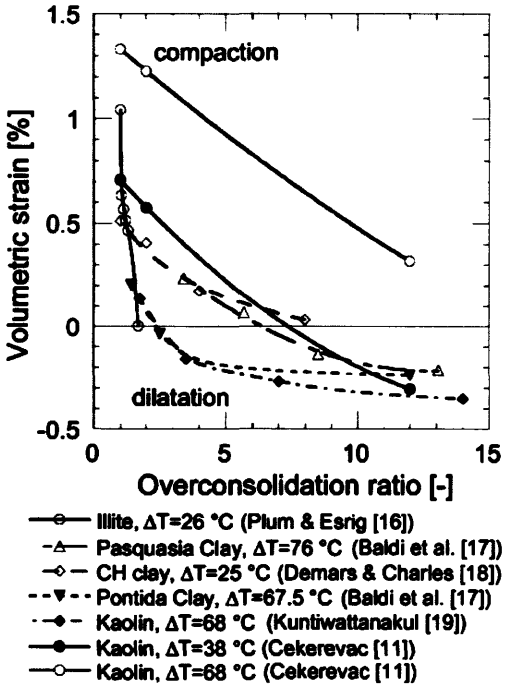


Figure 3.2: Influence of OCR on thermal volumetric strain (Laloui and Cekerevac, 2003)

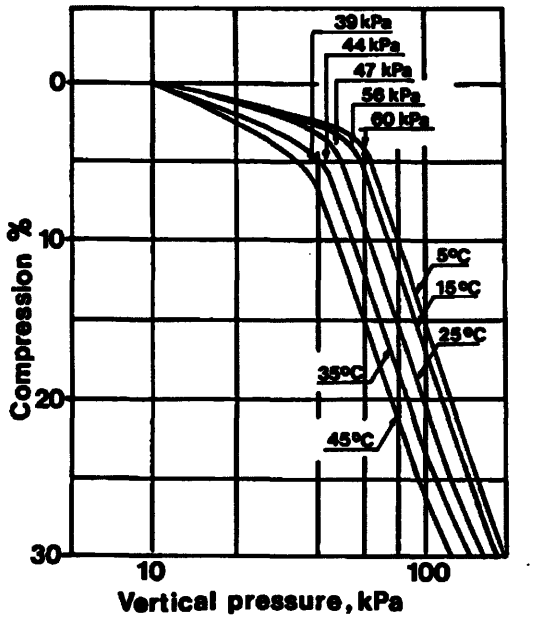


Figure 3.3: Results of oedometer tests performed on "identical" samples of Luleà clay at various temperatures (Eriksson, 1989).

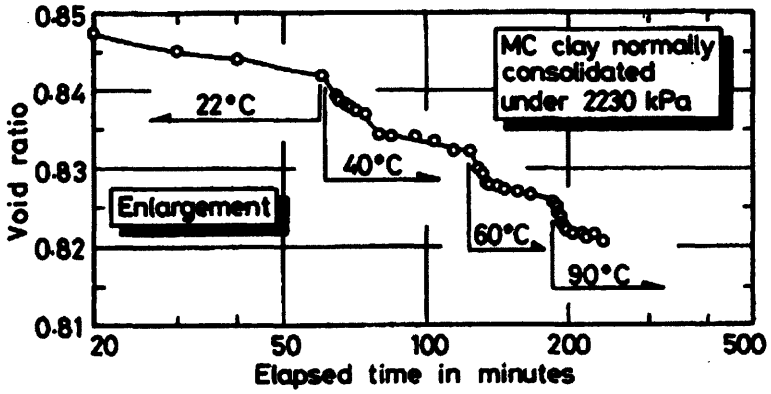


Figure 3.4: Increase in rate of consolidation with increasing temperature (Towhata et al., 1993)

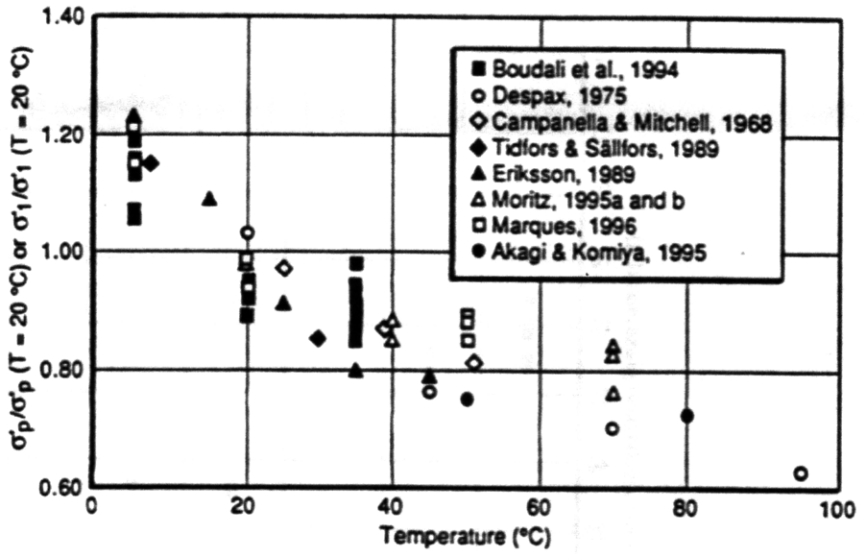


Figure 3.5: Variation of normalized preconsolidation pressure with temperature (Leroueil and Marques, 1996).

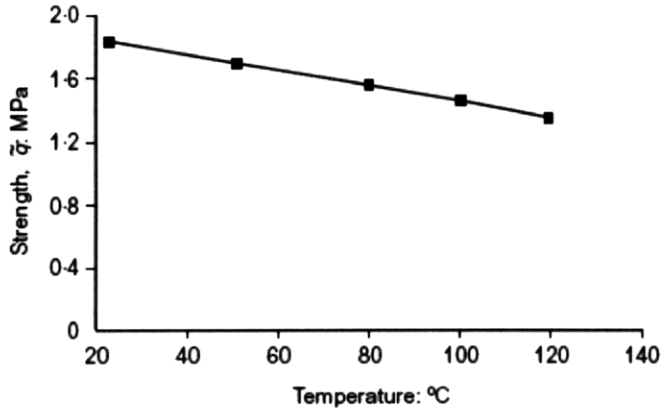


Figure 3.6: Strength of Spanish Clay from triaxial tests (Hueckel et al., 2009).

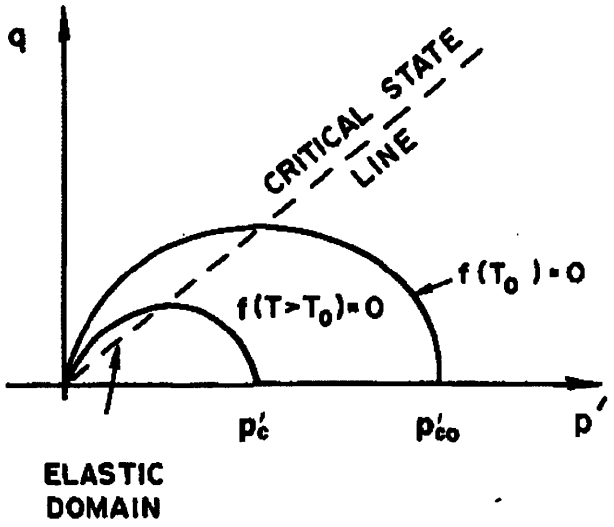


Figure 3.7: Elastic domain and yield surface, yield surface shrinks due to heating (Hueckel and Borsetto, 1990)

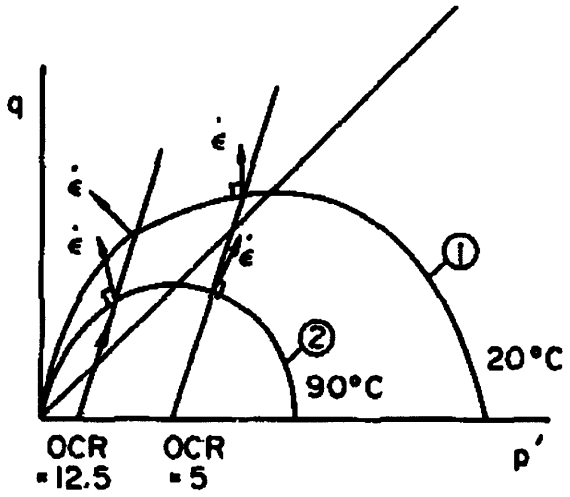


Figure 3.8: Two different stress paths for different OCR at different temperature (Hueckel and Baldi, 1990)

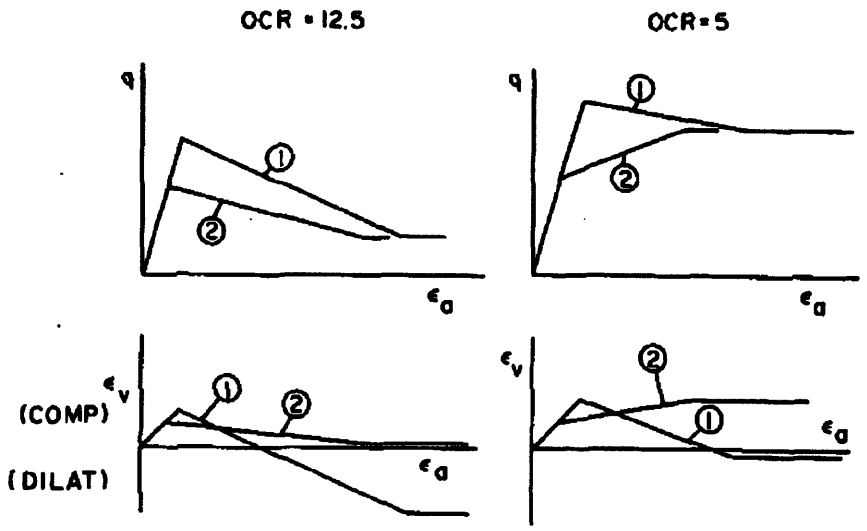


Figure 3.9: The theoretical response at (1) 20°C and (2) 90°C (Hueckel and Baldi, 1990)

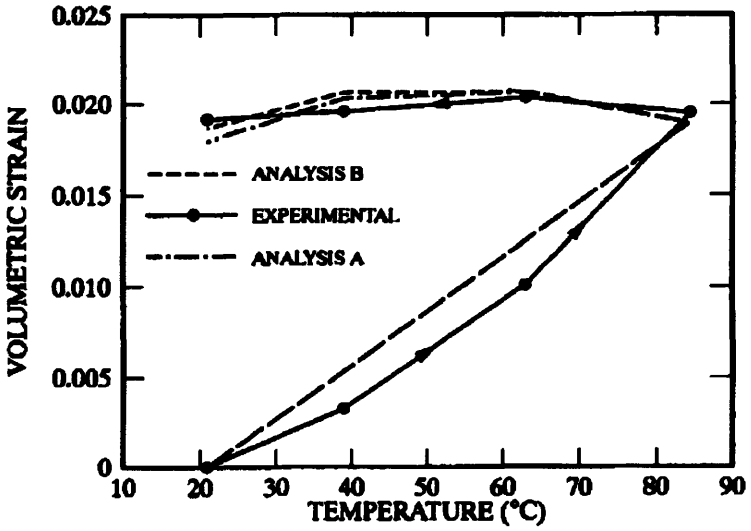


Figure 3.10: Comparison of Hueckel and Borsetto model with experimental measurements of volume strain for drained thermal loading (Seneviratne, 1993)

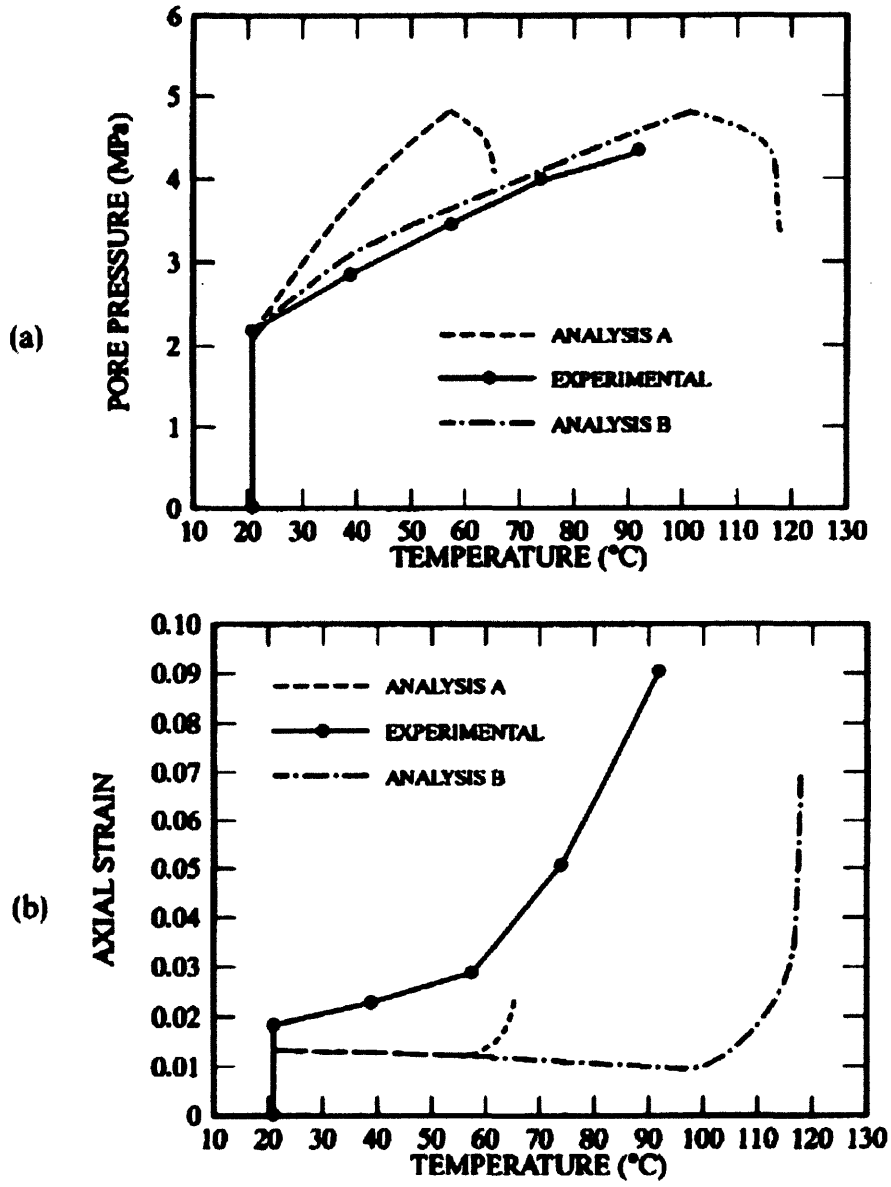


Figure 3.11: Undrained heating of Boom Clay (a) pore pressure response (b) axial strain response (Seneviratne, 1993)

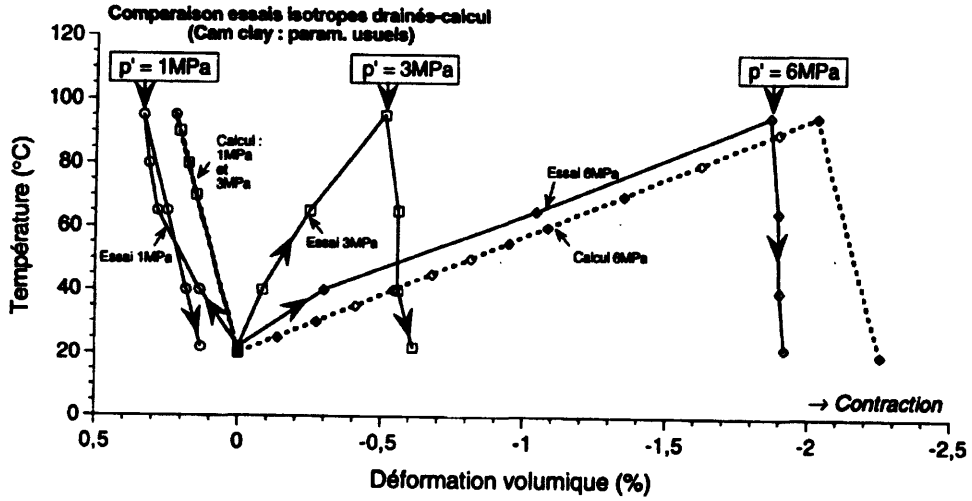


Figure 3.12: Lab results and predictions of Picard model showing deformation with temperature, v=12.6 (Picard, 1994)

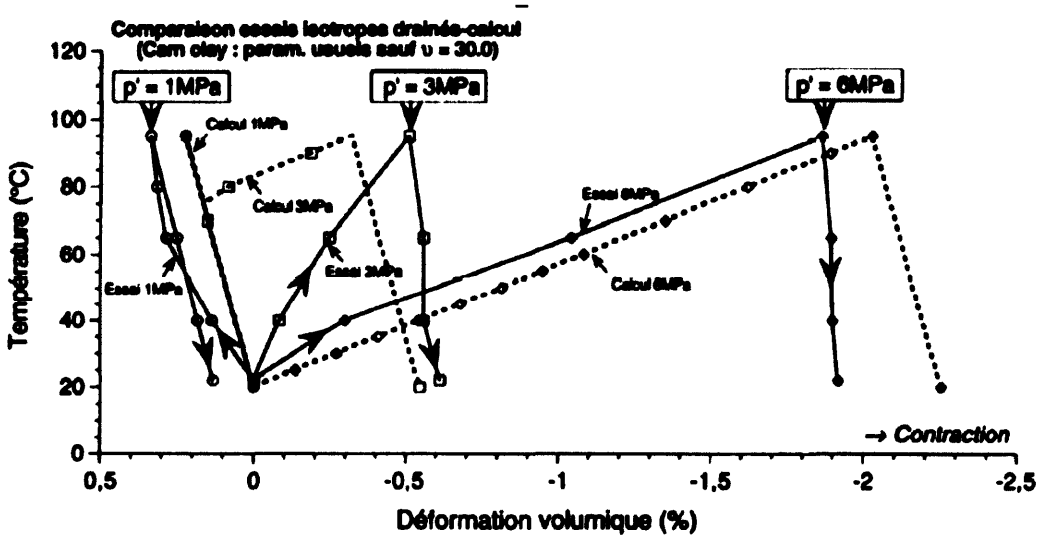


Figure 3.13: Lab results and predictions of Picard model showing deformation with temperature, v=30.0 (Picard, 1994)

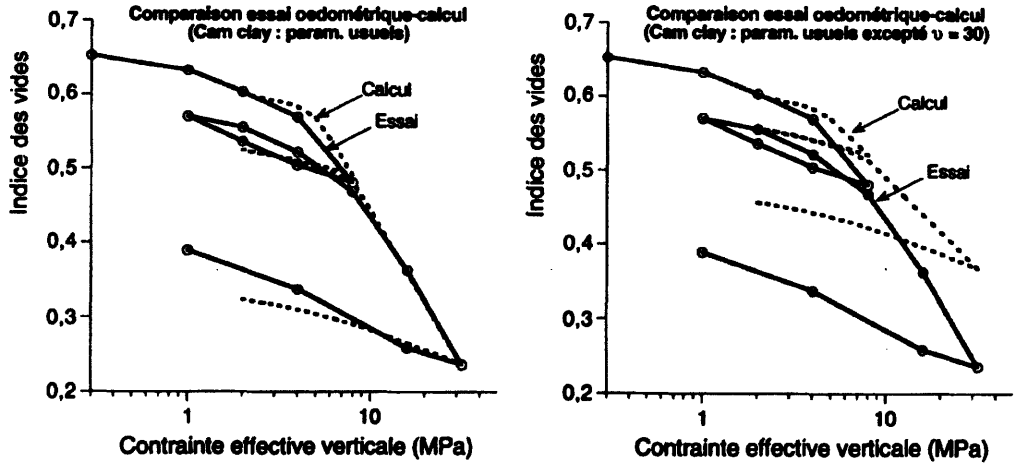


Figure 3.14: Effect of hardening parameter V on predictions of 1-D compression for Boom Clay (1) v=12.6, (2) v=30.0 (Picard, 1994)

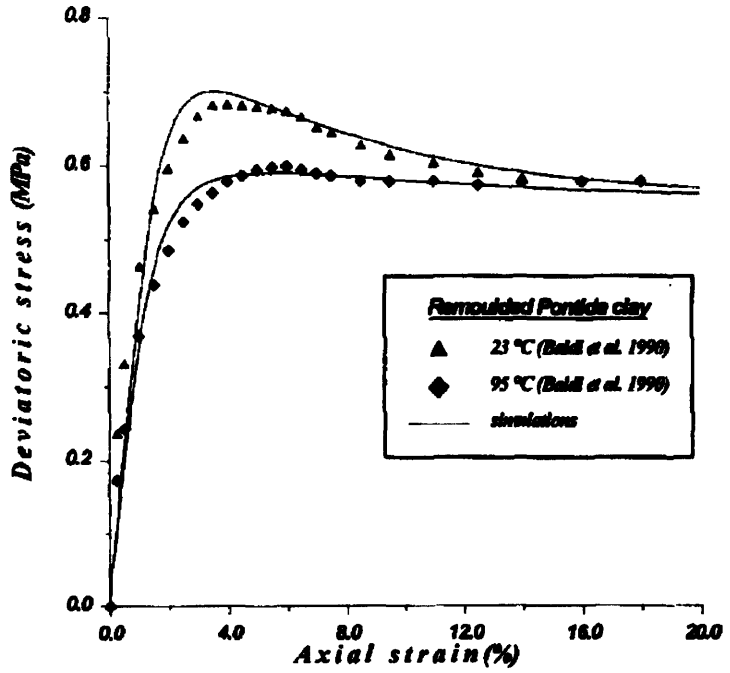


Figure 3.15: Comparison of simulations using the Robinet model with drained triaxial shear tests on overconsolidated Pontida Clay (Robinet et al., 1996)

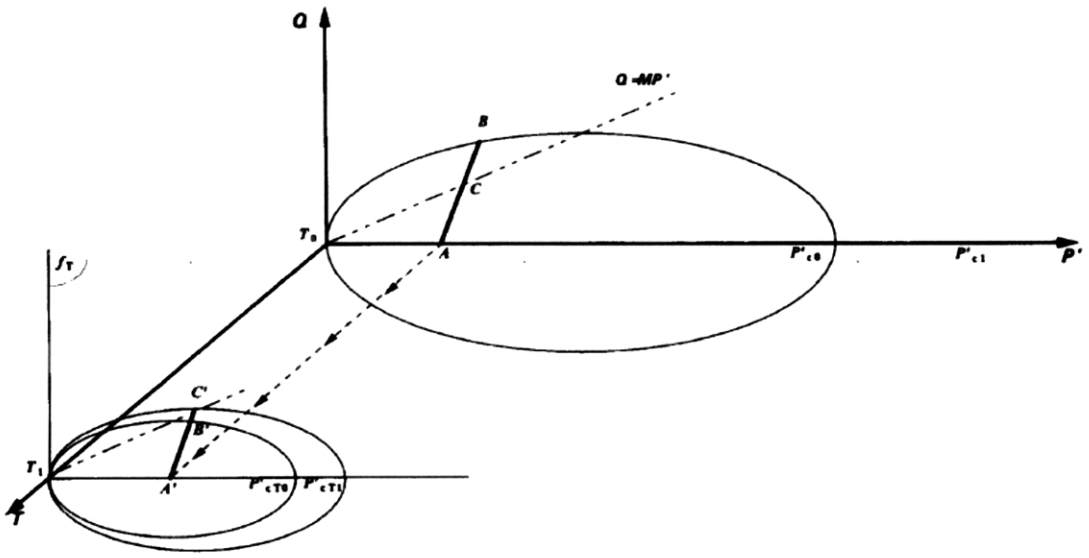


Figure 3.16: Stress paths for tests shown in Figure 3.15 above showing both plastic conditions (Robinet et al., 1996)

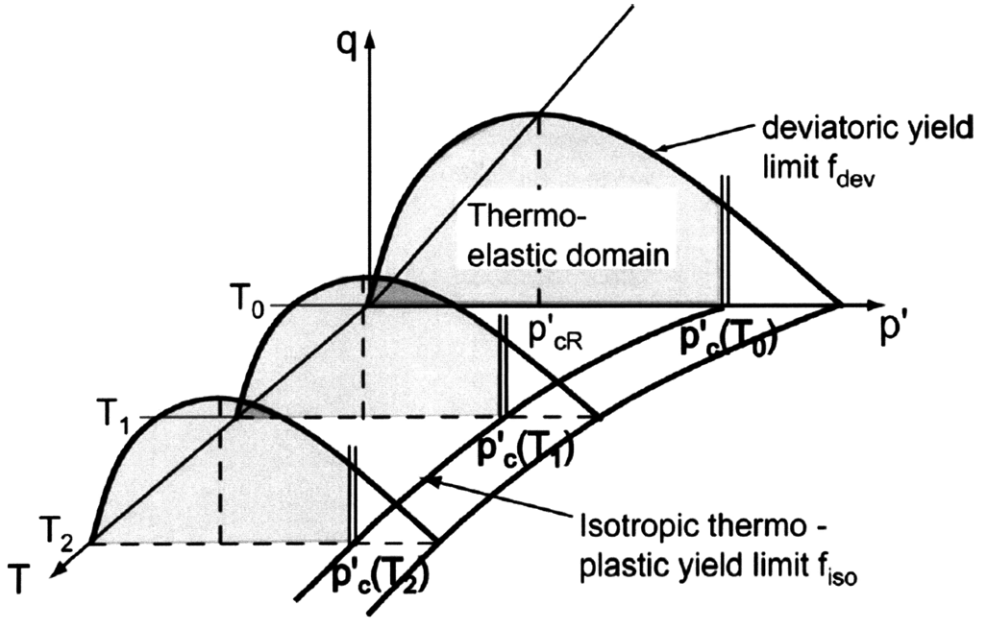


Figure 3.17: Schematic of ACMEG-T Thermo-mechanical model, showing both yield surfaces (François et al., 2008)

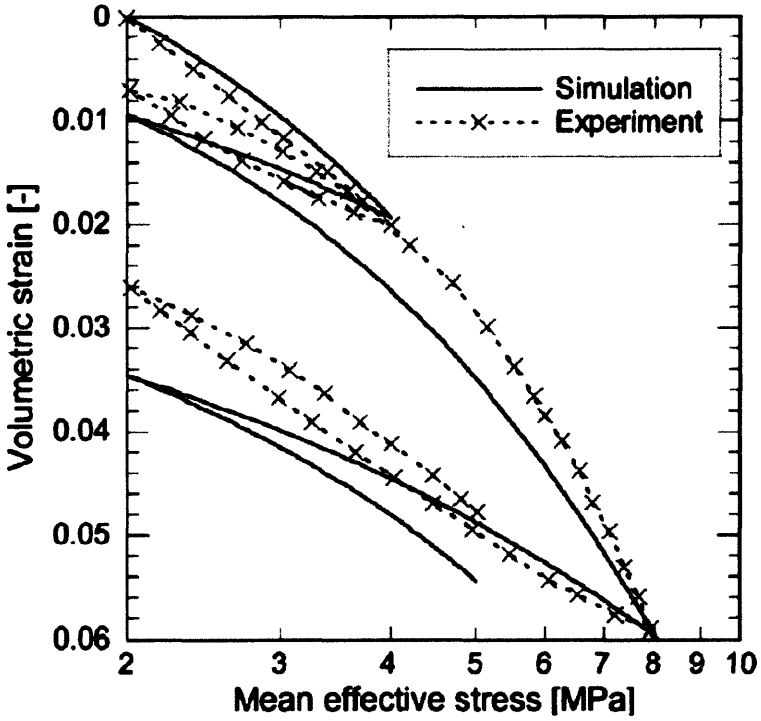


Figure 3.18: Comparison on ACMEG-T simulation and experiment, isotropic compression test. (François et al., 2008)

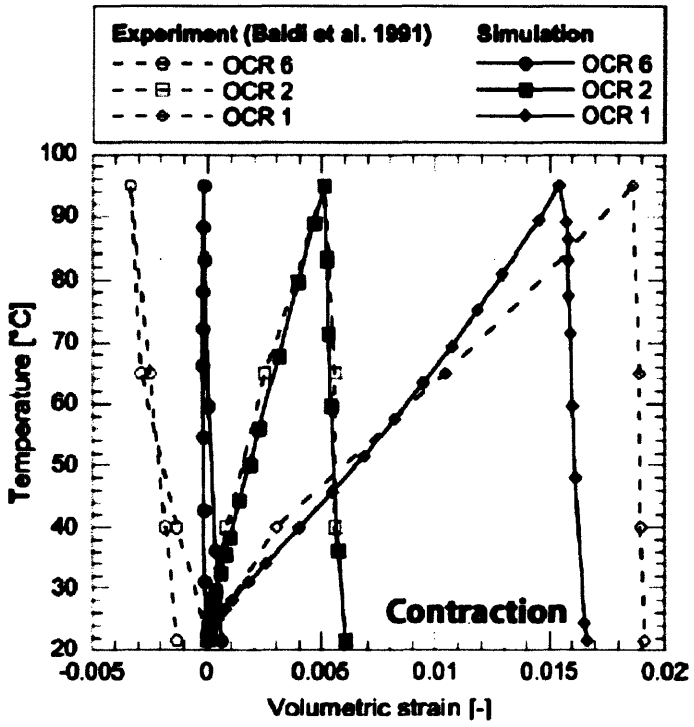


Figure 3.19: Comparison of ACMEG-T simulations volumetric strain measured in cycles of heating for Boom Clay (François et al., 2008).

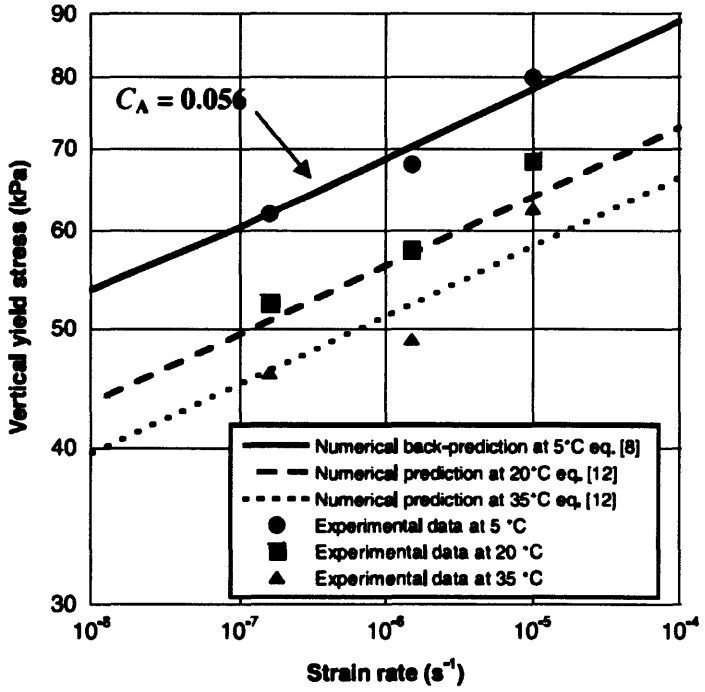


Figure 3.20: Changes in yield limit with strain rate at constant temperature: simulations and experiments (Laloui et al., 2008)

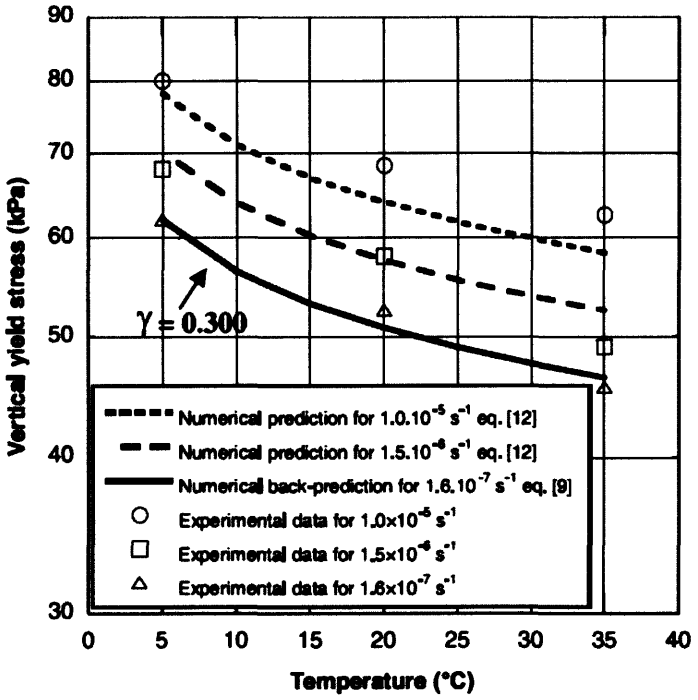


Figure 3.21: Changes in yield limit with temperature at constant strain rates: simulations and experiments on Berthierville Clay (Laloui et al., 2008)

# 4 EVALUATION OF THE PICARD MODEL

This chapter evaluates the Picard model (1994) through 1) the process of replicating Picard's simulations for Boom Clay; 2) the application of the Picard model for simulating data from a sensitive clay from St-Roch-de-l'Achigan (Marques et al., 2004) and 3) exploring the ability and limitations of Picard to simulate thermally induced strains.

## 4.1 Verifying Picard's Results

The original Picard (1994) model was developed and validated through comparisons with Baldi et al, (1991) and ISMES (1993). A number of these validation tests were repeated here.

Boom Clay is found in Northeast Belgium, near the town of Boom. It is a marine deposit from the Oligocene period. Boom Clay is principally composed of illite with, $w_n$ = 23-26%, $w_L$ = 60-70%, $w_p$ = 13-19% and $I_L$ = 45-55%.

The current implementation of the Picard (1994) model requires 18 input parameters (material properties and initial state variables) as shown in Table 4.1. together with input values selected for Boom Clay (Picard, 1994).

Figure 4.1 compares computed and measured behavior for a standard drained triaxial shear test (CIDC) performed on a specimen of reconstituted Boom Clay at $T=T_o=20°C$. The current simulation (Saxe, 2009) was carried out using parameters listed in Table 4.1. The model slightly overestimated the measured shear strength in this case.

Figure 4.2 shows a second CIDC test performed on Boom Clay at T=90°C. The computer simulations are good approximations of the measured data. However, there is a significant discrepancy between the computation reported by Picard (1994) and Saxe (2009). The apparent $p'_{co}$ at 90 °C computed by Saxe (2009) is 0.3 MPa larger than that

found by Picard (1994) indicating that the change in temperature resulted in a smaller contraction of the yield surface. The source of the discrepancy is unknown and may be due to the Beta status of the Picard (1994) Model on the CESAR-LCPC platform. The source of the error is most probable related to the preconsolidation stress parameter $p'_c$.

The data in Figure 4.1 shows $p'_{co}$ (at 20°C) is consistent between the sets of simulations. Two parameters, $\alpha_p$ and v, control thermal hardening[3]. There appears to be an error in the implementation of the thermal hardening equation in the program. From critical state soil mechanics:

$$p_y = p'_o + \frac{1}{3}q_y \text{ MPa} \tag{4.1}$$

$$q^2 - M^2 p'(p'_c - p') = 0 \tag{4.2}$$

$$p'_c = \frac{1}{p'}\left(\frac{q^2}{M^2}\right) + p' \text{ MPa} \tag{4.3}$$

From the Picard (1994) model:

$$p'_c = p'_{co}\exp\left(-v\left(\varepsilon_v^p + 3\alpha_p \Delta T\right)\right) \tag{4.4}$$

At first yield $\varepsilon_v^p$=0 therefore,

$$p'_c = p'_{co}\exp\left(-v3\alpha_p \Delta T\right) \text{ MPa} \tag{4.5}$$

The values of $q_y$ at 20°C and 90°C can be derived from Figures 4.1 and 4.2. Using equations 4.1, 4.3 and 4.5 it is possible to calculate $p'_c$. Table 4.2 shows $p'_c$ for all three simulations and $p'_{c90}$ derived from $p'_{c20}$. Table 4.2 shows that the simulations run by Picard correctly match the formulas presented for the model by Picard (1994). This

[3] Implementation was part of PhD thesis by Picard (1994) but has not been developed further within CESAR-LCPC. This model is only accessed through numerical input controls

indicates that the thermal hardening mechanism in the Picard model on the LCPC platform includes an error. The thermal hardening exhibited by Saxe (2009) is weaker than expected. The amount of thermal hardening exhibited by Saxe (2009) corresponds to $\alpha_p = 5x10^{-5}$, half the intended value. Until the error is corrected in the program, using artificially large values of $\alpha_p$ will correct for this problem without affecting other parts of the model.

## 4.2 St-Roch-de-l'Achigan Clay

St-Roch-de-L'Achigan (SRLA) Clay is a Champlain Sea clay from Quebec, Canada. The thermal behavior of this clay was discussed by Marques et al (2004). SRLA Clay is very sensitive with $S_t$=30 to 50 and highly plastic. The vertical yield stress of SRLA Clay changes 1%/°C, indicating that the deformation behavior of the clay is significantly effected by temperature changes (Marques et al., 2004). Figure 4.3 compares two sets of 1-D consolidation test of the SRLA Clay at 10°C and 50°C. The results show an average difference in volume strain $\Delta q$=5% at a given level of effective stress, corresponding to the offset in the VCL's at these two temperatures.

The careful documentation of soil properties and testing procedures by Marques et al (2004) made it possible to simulate the 1-D compression behavior of SRLA Clay using the Picard Model. Table 4.3 lists the properties that were used to calculate the inputs needed for the Picard model. The value for the Biot Modulus was taken from that listed by Picard (1994) for Boom Clay. $G_s$ was taken to equal 2.74.

From Marques et al (2004) the water content, w=85%. Assuming that the clay is fully saturated and using $G_s$=2.74, it was possible to estimate void ratio, $e_o$, before shearing. The initial void ratio, $e_o$= 2.33.

With $e_o$, $\kappa$ and $\nu$: it was possible to determine the Young's Modulus, E, at p' = 150 kPa.

$$K = \frac{1+e}{\kappa} p' = 2.3\ MPa \qquad (4.6)$$

$$K = \frac{E}{3(1-2\nu')}; \nu' = 0,35; E = 2.1 MPa \qquad (4.7)$$

$\alpha_p$ was determined through trial and error in repeated simulations to match the change in preconsolidation pressure from 10°C to 50°C and found to be $\alpha_p = 10^{-3}\ K^{-1}$.

$v$ is the coefficient of thermal hardening $v = \frac{1+e_0}{\lambda - \kappa}$.

Table 4.4 list the input parameters selected for SRLA Clay using the Picard Model.

## 4.3 1-D Drained Compression of SRLA Clay

Drained 1-D compression behavior was simulated using CESAR-LCPC with the sample fully drained through the duration of the test. The deformation of the sample was specified through displacement control. Fifty increments of 0.005 m ($d\varepsilon$=0.5%) displacement were applied at constant temperature, T, at 10°C, 20°C and 50°C. The temperature of the sample was held constant throughout the test.

Figure 4.4 shows the Picard model simulation compared with the experimental results found by Marques et al 1994. The analysis does not precisely predict the measured data. In reality, $\lambda$ is not constant, it changes subtly with changes in temperature and/or stress level. The Picard model assumes linearized behavior of the normally consolidated clay in e-logp' space. In contrast, SRLA is highly sensitive clay and is not well described by a single compression index (e.g. $C_c$ or $\lambda$ are not constant for SRLA Clay). However, the model calibration (with $\alpha_p = 10^{-3} K^{-1}$) gives a reasonable approximation for the difference in axial strains observed at 10°C and 50°C. However, the simulations became less accurate with increasing vertical effective stress, $\sigma'_v$.

Having verified that it is possible to match experimental data in 1-D consolidation using the Picard model, the next step was to evaluate the behavior of the simulated SRLA Clay during drained and undrained shearing.

## 4.4 Undrained Shearing

Undrained triaxial shearing of a 1m-radius sample in axisymmetric conditions was performed to test SRLA Clay in undrained shear. No drainage was allowed during shearing. The temperature was held constant at either 20°C or 50°C. The initial temperature of the sample was set to either 20°C or 50°C, the thermal boundaries were held constant through the duration of the test and no thermal load was applied to the sample during testing. The sample was loaded in two steps:

1) Fully drained until normally consolidated condition at p' = 112 kPa, q=0 kPa, $p'_{co}$=111 kPa;
2) Undrained shearing by displacement-control until failure

Figures 4.5-4.7 show the results of undrained shearing at 20°C and 50°C.

According to the MCC model, the undrained shear strength of isotropically consolidated SRLA Clay can be found analytically through:

$$\frac{s_u}{p'_{co}} = \frac{M}{2}(0.5)^m \qquad (4.8)$$

Where $m = 1 - \frac{\kappa}{\lambda}$ and $2s_u = q_f$

There is some uncertainty in the value of m, as only $v = \frac{1+e_0}{\lambda - \kappa}$ is specified in the Picard model. However assuming m = 0.85-1.0, leads to a range for $q_f$= 63.3 – 70.2 kPa. Figure 4.5a, $q_{f\text{-simulated}}$, showed a unique effective stress path for both temperatures with $q_f$ =67 kPa (i.e., m=0.91).

Figure 4.5a underlines that the main thermal control in the Picard model is $\alpha_p$, which controls the changes in $p'_c$ with temperature. After yielding, any thermal effects are negligible. In both tests, 20°C and 50°C, the sample was consolidated to an NC state. The subsequent undrained shear response is unique for all temperatures.

The difference is that the yield surface shrinks with increasing temperature. The sample at 50°C yielded before the sample at 20°C and therefore experienced more deformation during the K=1 consolidation stage. Figure 4.5b shows the shear stress-strain response. Figure 4.6 includes axial strain in both consolidation and shearing phases at T=20°C and 50°C.

Figure 4.7 shows the volumetric (void ratio, e, vs. lnp') space used in CSSM during shearing. The 50°C sample experienced approximately 3% more volumetric deformation during consolidation to p'=112 kPa than the 20°C sample. Since this was an undrained simulation, there was no volume change during shearing. Both tests failed at the same p', indicating that there is an equal offset in the location of the CSL and VCL lines at 20°C and 50°C.

The slopes ($\lambda$) of both VCLs and CSLs lines are parallel and equal to $\lambda$=0.96. The slope of 0.96 is significantly lower than the assumed $\lambda$ of 1.25. The apparent $\lambda$ is dependent on the apparent $\kappa$, which in turn is dependant on the Young's Modulus. The Young's Modulus, as an input parameter, is set and does not change with changes in stress and strain in the model. This will result in changes in the apparent $\kappa$ and, by association, the apparent $\lambda$.

## 4.5 Drained Shearing

Drained triaxial shearing was carried out using the same CESAR-LCPC axisymmetric model. Full drainage was provided to the sample; 0 kPa pore pressure was allowed to develop in the sample and the temperature was either 20°C or 50°C. The sample was loaded in two steps:

1) Fully drained until normally consolidated at p' = 112 kPa, q = 0 kPa, p'co = 111 kPa;
2) Drained loading by stress control until failure.

Figures 4.8-4.11 show the results of the drained shear tests.

From critical state soil mechanics, it is possible to calculate the expected point of failure during drained shearing. The point of failure should be the intersection of the critical state line and a line extending from the starting point of shearing at a slope of 3.

Critical State Line: $q = 1.13p'$

Slope of Shearing: $p' = 112 + \frac{1}{3}q$

Expected point of failure: $p'_f = 179.6$ kPa, $q_f = 203$ kPa

Figure 4.8 shows that the simulations predicted the same failure point as calculated above. However, the simulation predicted very large strains, due to the extremely high sensitivity of SRLA Clay.

Figures 4.8b and 4.9 illustrate the q vs axial strain relationship. During consolidation before shearing, the 50°C deformed 3% more than the sample at 20°C. The 3% offset is obscured by the very large strains experienced during drained shearing. The deformations here are very large due to the very large plasticity of the SRLA Clay. Such large deformations would not be observed due to the high sensitivity of the clay and structuring phenomenon not discussed here (Marques et al 2004). Figures 4.8c and 4.10 show the axial strain-volume strain relationship with and without the initial effects of consolidation.

Similar to the undrained case, Figure 4.11, shows that there are small differences in shear and consolidation behavior at 20°C and 50°C in drained conditions. During consolidation to 112 kPa, the sample at 50°C consolidated 3% more than the sample at 20°C. During drained shear the two samples exhibit similar behavior while maintaining the original deformation offset. As in the undrained case both simulation fail at the same p', underlining the equal left shift in the VCL and CSL with increasing temperature.

## 4.6 Effect of Temperature Change in Undrained Shear of NC SRLA Clay

The previous paragraph highlights the offsets in VCL and CSL during consolidation and shear in NC SRLA Clay while constant temperature is maintained throughout the test. This section explores the effects of changing temperature environments during consolidation and shearing for NC SRLA Clay.

Two constant volume simulations were compared:

A. Consolidated fully drained at 20°C to p'=112 kPa, q=0 kPa, then sheared undrained until failure at 50°C
B. Consolidated fully drained at 50°C to p'=112 kPa, q=0 kPa, then sheared undrained until failure at 20°C

Since the shearing was displacement-controlled, the displacement path of the sample doesn't change. Instead, the stress level in the samples adjusted to match the amount of displacement being imposed upon them. Figure 4.12a shows the stress paths for specimens A and B. For specimen A, the change $\Delta T=(T_2-T_1)$ = +30°C, causes a step change in the excess pore pressure within the sample ($\Delta u \approx 12$ kPa) as no volume change can occur. This leads to an equal reduction in the effective stress. The subsequent stress path is analogous to the one shown is Figure 4.5a. Due to the lower initial stress before shearing, the shear strength, $S_u$=67 kPa, is reduced to $S_u$=62 kPa, a reduction of 9%. For

specimen B there is no measured change is pore pressure due to $\Delta T=(T_2-T_1)=-30°C$. However, smaller pore water pressures, $\Delta u$, develop during the test, which leads to an increase in measured shear strength. For specimen B, the measured shear strength increased from 67 kPa to 72 kPa, and increase of 9%. Figure 4.12b shows the deviator stress, q, versus axial strain, $\varepsilon_a$, for specimens A and B.

Figure 4.13 illustrates the void ratio, e, vs lnp' relationship during undrained shearing for specimens A and B. Specimen A, consolidated at 20°C, begins shearing on the 20°C-VCL, similar to the 20°C sample in Figure 4.7. However, since specimen A was sheared at 50°C, it continues to deform past the 20°C-CSL and fails on the 50°C-CSL at p'=55.5 kPa. Similarly, specimen B begins shear on the 50°C-VCL and fails on the 20°C-CSL at p'=64.6 kPa.

## 4.7 Effect of Temperature Change in Drained Shear Behavior

Effects of temperature change in drained shear of NC SRLA Clay are considered by comparing Picard (1994) model predictions for two cases.

C. Consolidated fully drained at 20°C to p'=112 kPa, q=0 kPa, then sheared drained until failure at 50°C
D. Consolidated fully drained at 50°C to p'=112 kPa, q=0 kPa, then sheared drained until failure at 20°C

The drained tests were stress controlled and followed the same stress path as the tests that were run at constant temperature.

Figure 4.14a shows the stress paths of specimens C and D. Figure 4.14b and 4.14c show the q-axial strain, $\varepsilon_a$, and volume strain, $\varepsilon_v$, -axial strain, $\varepsilon_a$, relationships.

Figure 4.14c shows the axial strain during the drained shearing. During shearing, all the samples exhibit the same deformation behavior. In Figure 4.14c, there is a small offset for the different tests. The general behavior is the same; the offset is due to the expansion of the soil particles due to the temperature change as controlled by thermo-elastic properties, $\alpha_d$ and $3\alpha_m$.

Specimen C shows at immediate volumetric compression ($\Delta\varepsilon_v \approx 3\%$) due to the step change in temperature $\Delta T=(T_2-T_1) = +30°C$. Thereafter, the behavior is dominated by the large shear strains needed to attain the critical state condition. For specimen D, the change in temperature $\Delta T=(T_2-T_1) = +30°C$ results in an apparent overconsolidation. Figure 4.15 shows the stress path of both samples in e-lnp' space.

Figure 4.15 illustrates the movement of the specimens between the VCL and CSL lines of the two different temperatures. Specimen C began on the 20°C-VCL, then due to the step change in temperature deforms at constant stress until the 50°C-VCL. During shearing, specimen C followed the 50°C drained shear path to CS on the 50°C-CSL. Specimen D began on the 50°C-VCL, then due to the reduction in temperature experiences an increase in stress with constant volume to move onto the 20°C-VSL. During shearing, specimen D followed to 20°C drained shear path to CS on the 20°C CSL.

## 4.8 Cyclic Thermal Loading

Having evaluated the behavior of the Picard model at different constant temperatures and consolidated at one temperature and sheared at another, the next step was to evaluate a temperature cycle in undrained shearing. Two tests were performed:

C. The sample was consolidated at 20°C, then sheared at 50°C half of the way to failure, ($q/q_f=0.5$), finally the temperature was decreased back to 20°C and sheared until failure

D. The sample was consolidated at 50°C, then sheared at 20°C half of the way to failure, ($q/q_f$=0.5), finally the temperature was decreased back to 50°C and sheared until failure

The results indicate the capability of the Picard (1994) model to simulate repeated expansion and contraction of the yield surface during cyclic thermal loading.

Figure 4.16 and 4.17 shows the e-lnp' relationship for specimen E and F, respectively. The samples behaved as expected. As shown in Figure 4.16, for specimen E, the shift after consolidation to 50°C resulted in an increase in strain at constant pressure, and the decrease to 20°C resulted in an apparent preconsolidation pressure. The sample failed at the same point as the constant 20°C simulation.

Figure 4.17 illustrates the results from a simulation consolidated at 50°C, sheared at 20°C halfway to failure, reheated to 50°C and sheared to failure. The initial cooling produces an apparent preconsolidation pressure; with increased stress the path shifts to the constant 20°C line. After reheating, the volume strain increased at constant stress until the 50°C line and then follows the 50°C path until failure.

Table 4.1: Picard Model input parameters for Boom Clay (from Picard, 1994)

| *Physical Properties* | | | |
|---|---|---|---|
| Buoyant Density | $\rho_{bouyant}$ | $kN/m^3$ | 7.5 |
| Fluid Density | $\rho_{fluid}$ | $kg/m^3$ | 1000 |
| Porosity | n | | 0.4 |
| | | | |
| *Conduction Properties* | | | |
| Permeability $K_{xi}=K_{yi}=K_{zi}$ | $k_{x\text{-}intrinsic}$ | m/s | 2.70E-2 |
| Thermal Conductivity $K_{xT}=K_{yT}=K_{zT}$ | $k_{x\text{-}thermal}$ | W/m/K | 1.7 |
| | | | |
| *Material Properties* | | | |
| *Poro-Elastic* | | | |
| Young's Modulus | E | Pa | 1.80E+08 |
| Poisson's Ratio | $\nu$ | | 0.17 |
| Biot Coefficient | b | | 1 |
| Biot Modulus | $M_{biot}$ | Pa | 4.40E+09 |
| Skempton's Coefficient | $\beta$ | | 1 |
| *Thermo-Elastic* | | | |
| Thermo-Elastic Compressibility Coefficient | $\alpha_d$ | $K^{-1}$ | 1.00E-05 |
| Thermal Expansion Coefficient | $3\alpha_m$ | $K^{-1}$ | 1.00E-05 |
| *Thermo-Plastic* | | | |
| Slope of the Critical State Line | M | | 0.87 |
| Coefficient of Plastic Strain Hardening | $V=(1+e_0)/(\lambda-\kappa)$ | | 12.6 |
| Coefficient of Thermal Hardening | $\alpha_p$ | $K^{-1}$ | 1.00E-04 |
| | | | |
| *Other* | | | |
| Preconsolidation Pressure | $P_{c0}$ | Pa | 5.00E+06 |
| Reference Temperature | $T_o$ | Deg C | 20 |

Table 4.2: Calculation of $p'_c$ using critical state soil mechanics and Picard thermal hardening

| | | | From Figure 4.2 | |
|---|---|---|---|---|
| | Formula | Expected at 20°C | At 90°C (Saxe) | At 90°C (Picard) |
| $q_y$ | | 2.2 | 1.9 | 1.6 |
| $p_y$ | $p_y=p_o+1/3q_y$ | 2.7 | 2.6 | 2.5 |
| $p_c$ | $p'_c=1/p'(q^2/M^2)+p'$ | 5.0 | 4.4 | 3.8 |
| $p_c$ | $p'_c=p'_{co}\exp(-v3\alpha_p\Delta T)$ | 3.8 | | |

Table 4.3: Physical and engineering properties of SRLA Clay (Marques et al., 2004)

| | UNITS | | NOTES |
|---|---|---|---|
| w | % | 85% | $G_s*w=S*e$ |
| $G_s$ | | 2.74 | $G_s=\gamma'_s/\gamma'_w$ |
| $e_0$ | | 2.33 | |
| $C_C/1+e_0$ | | 0.86 | Between given range of 0.59 to 1.36 |
| $C_c$ | | 2.88 | |
| $\lambda$ | | 1.25 | $\lambda = 0.434C_c$ |
| $\kappa$ | | 0.05 | |
| $\sigma_{pconv}$ | kPa | 125 | Average of 120-130 range |
| $K_0=\sigma'_3/\sigma'_1$ | | 1 | |
| $\phi_{peak}$ | degrees | 28.5 | |
| $\phi_{criticalstate}$ | degrees | 36.4 | |
| $k_{thermal}$ | W/m/K | 1.7 | |

Table 4.4: Picard Model input parameters for SRLA Clay

| *Physical Properties* | | | |
|---|---|---|---|
| Buoyant Density | $\rho_{bouyant}$ | $kN/m^3$ | 5.0 |
| Fluid Density | $\rho_{fluid}$ | $kg/m^3$ | 1000 |
| Porosity | n | | 0.4 |
| | | | |
| *Conduction Properties* | | | |
| Permeability $K_{xi}=K_{yi}=K_{zi}$ | $k_{x\text{-intrinsic}}$ | m/s | 2.5E-9 |
| Thermal Conductivity $K_{xT}=K_{yT}=K_{zT}$ | $k_{x\text{-thermal}}$ | W/m/K | 1.7 |
| | | | |
| *Material Properties* | | | |
| *Poro-Elastic* | | | |
| Young's Modulus | E | Pa | 2.1E+06 |
| Poisson's Ratio | $\nu$ | | 0.35 |
| Biot Coefficient | b | | 1 |
| Biot Modulus | $M_{biot}$ | Pa | 4.40E+09 |
| Skempton's Coefficient | $\beta$ | | 1 |
| *Thermo-Elastic* | | | |
| Thermo-Elastic Compressibility Coefficient | $\alpha_d$ | $K^{-1}$ | 1.00E-05 |
| Thermal Expansion Coefficient | $3\alpha_m$ | $K^{-1}$ | 1.00E-05 |
| *Thermo-Plastic* | | | |
| Slope of the Critical State Line | M | | 1.13 |
| Coefficient of Plastic Strain Hardening | $v=(1+e_0)/(\lambda-\kappa)$ | | 2.77 |
| Coefficient of Thermal Hardening | $\alpha_p$ | $K^{-1}$ | 1.00E-03 |
| | | | |
| *Other* | | | |
| Preconsolidation Pressure | $P_{c0}$ | Pa | 1.11E+05 |
| Reference Temperature | $T_o$ | Deg C | 20 |

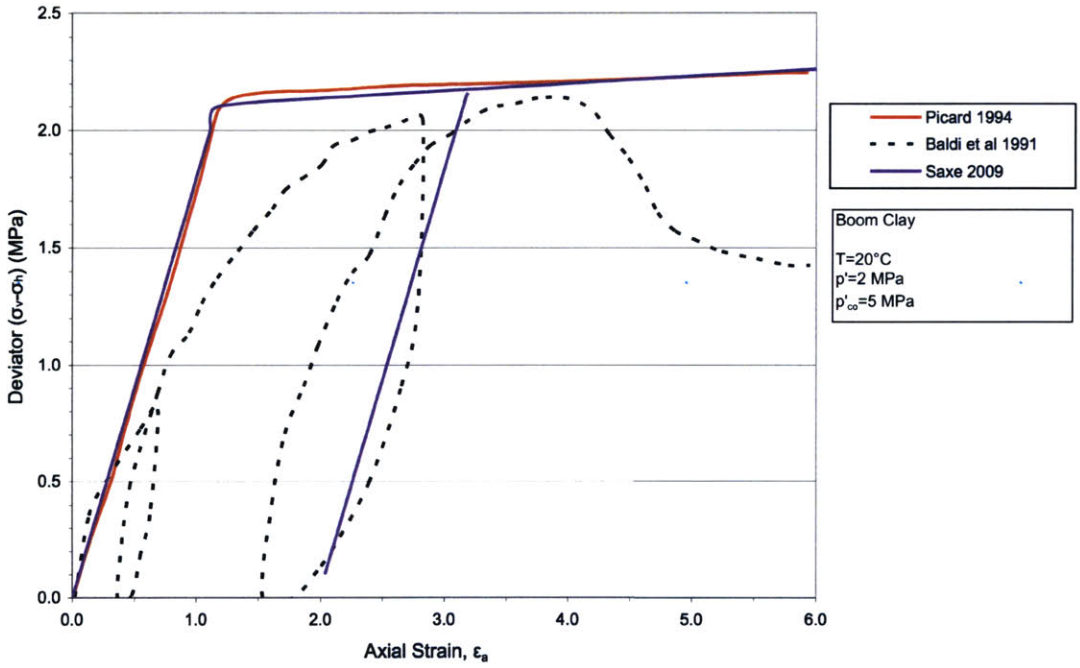


Figure 4.1: Comparison of numerical simulations using Picard Model for CIDC test on overconsolidated Boom Clay at T = 20°C

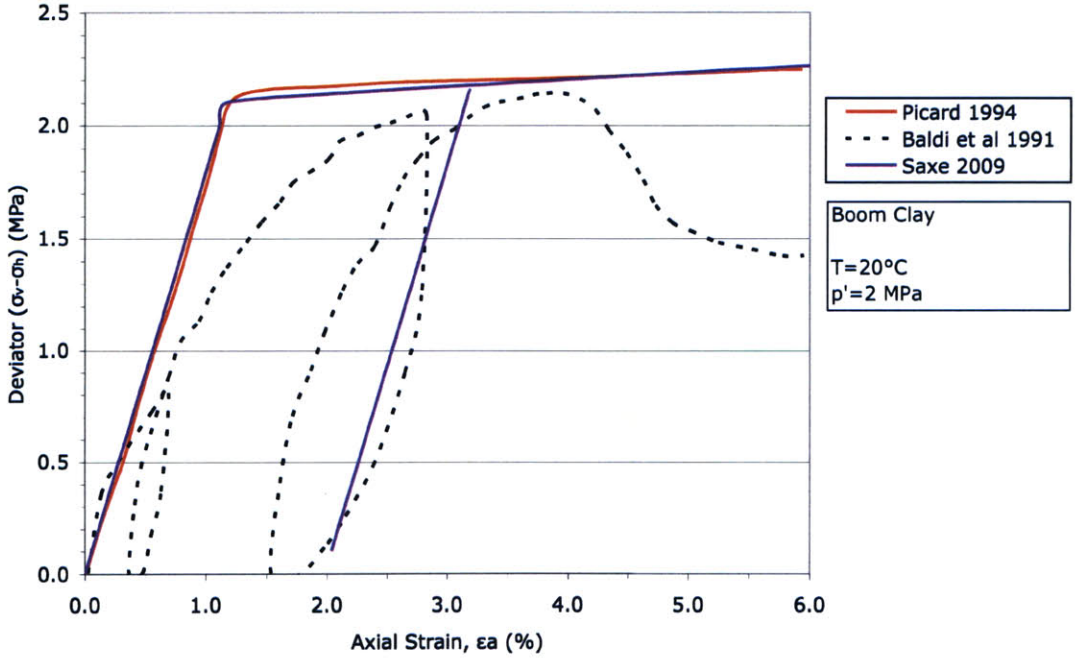


Figure 4.2: Comparison of numerical simulation vs. Picard model for CIDC test on overconsolidated Boom Clay at T = 90°C

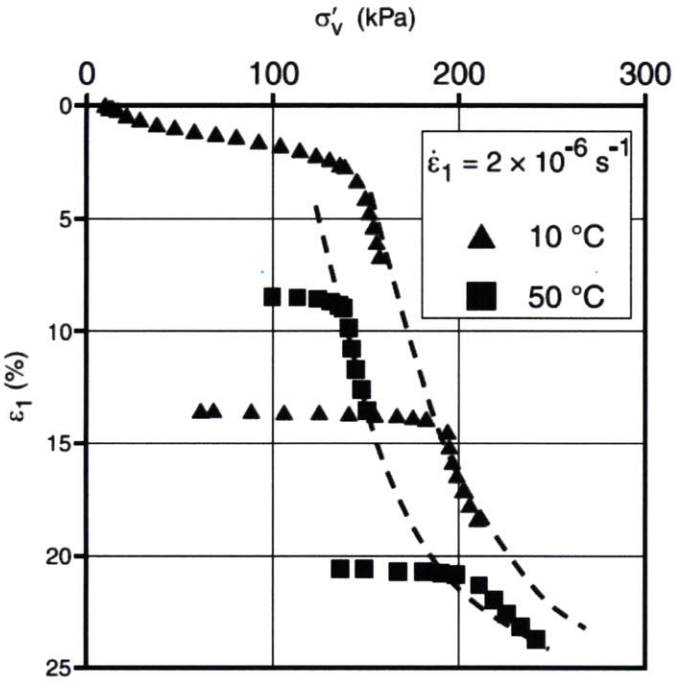


Figure 4.3: The effect of temperature on 1-D drained compression of SRLA Clay (Marques et al., 2004)

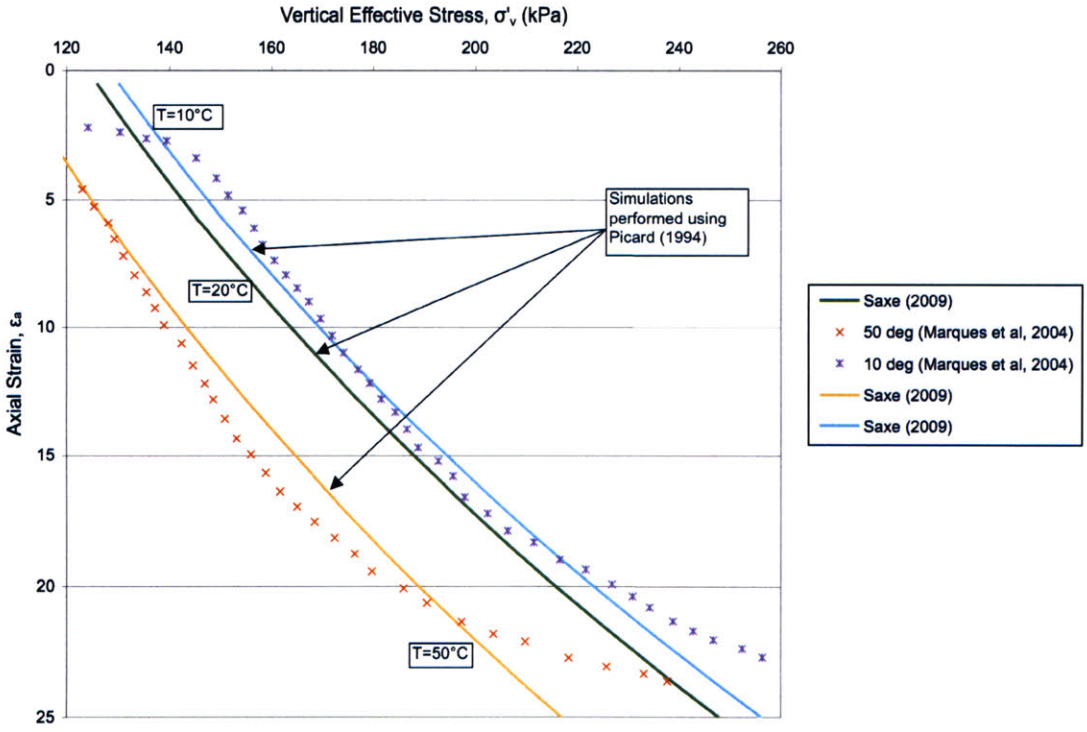


Figure 4.4: 1-D compression, SRLA Clay

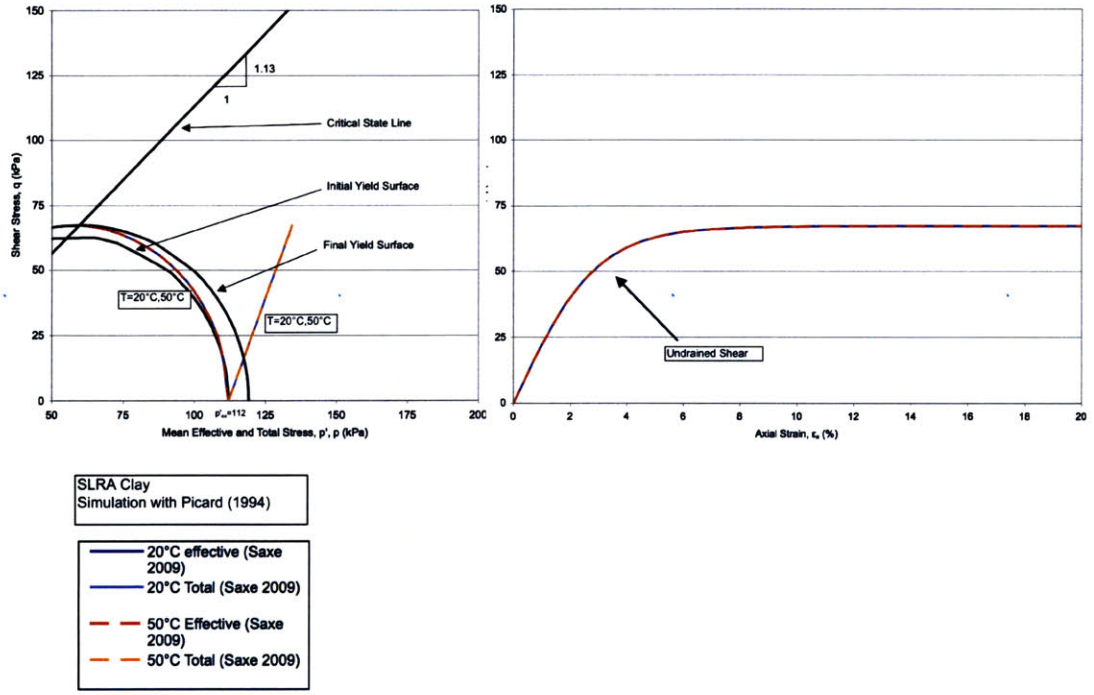


Figure 4.5:(a) Effect of temperature on undrained shear response of SRLA Clay using Picard (1994) model, (b) undrained shear: q vs axial strain, $\varepsilon_a$ during shearing

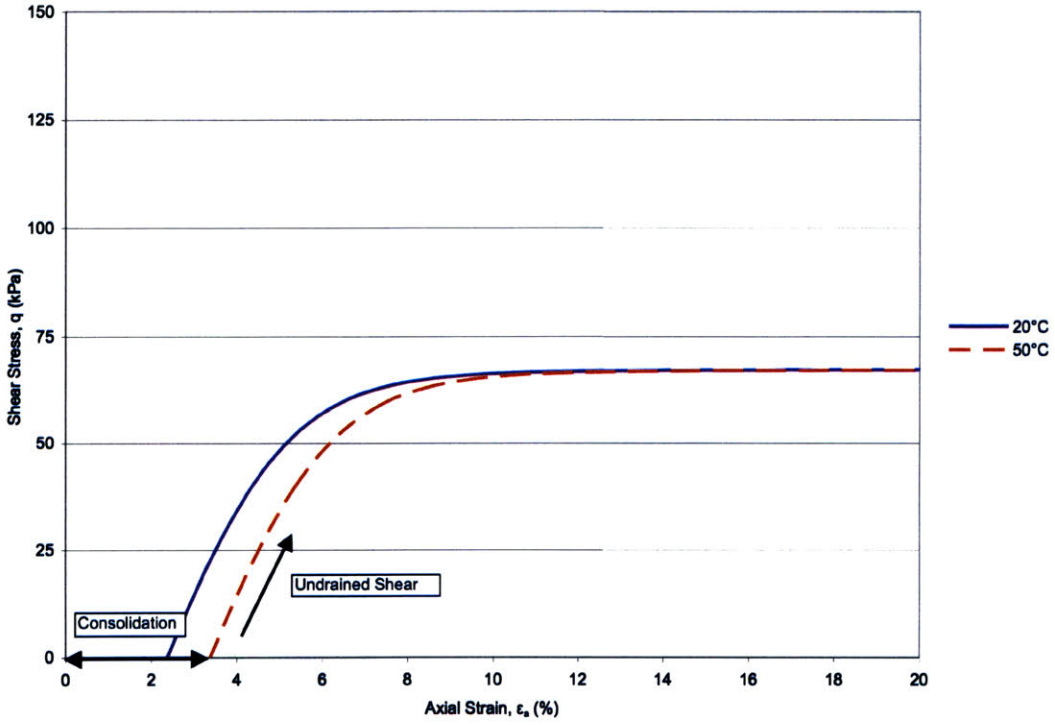


Figure 4.6: Undrained shear: q vs axial strain (%) including strain during K=1 consolidation

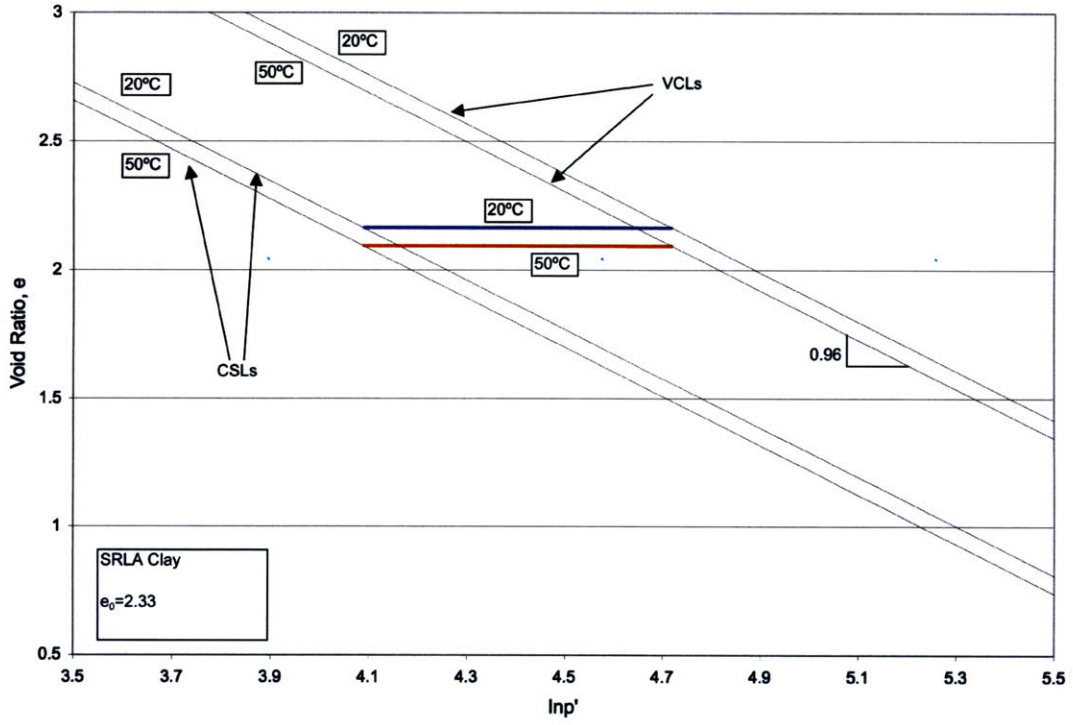


Figure 4.7: Undrained shear: void ratio, e, vs lnp'.

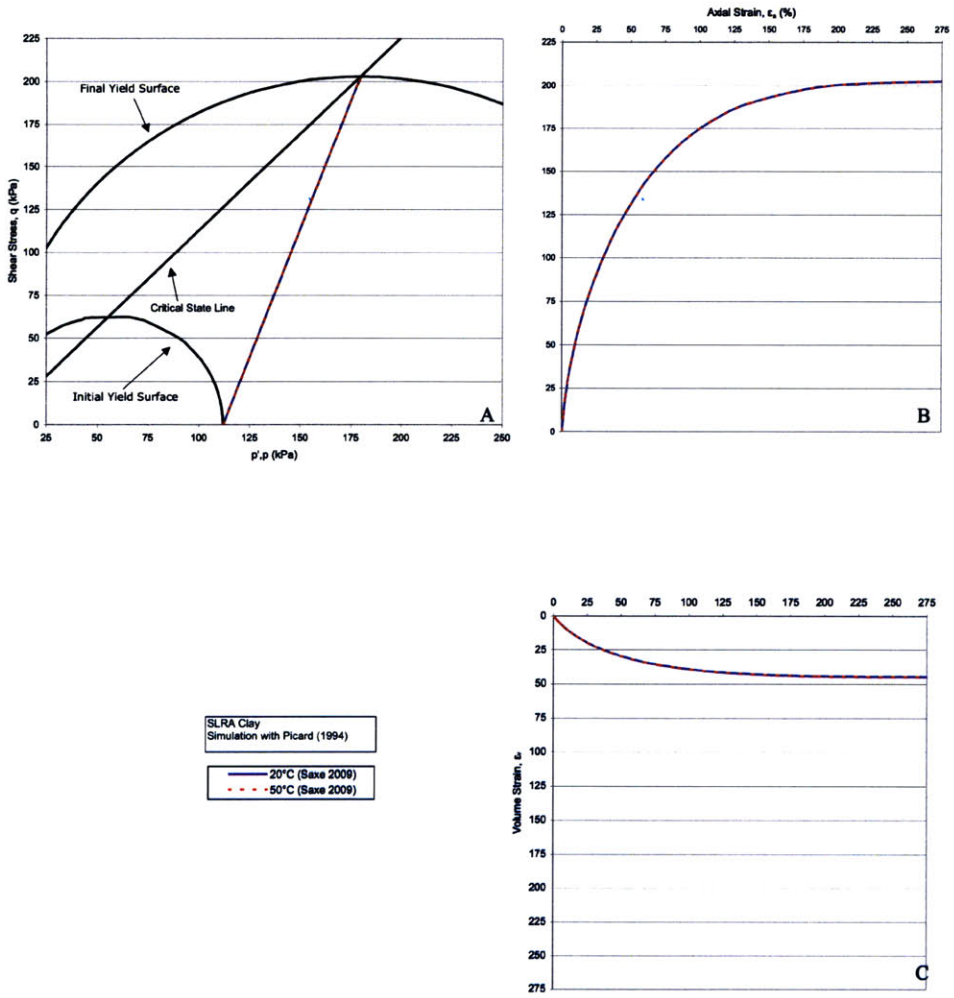


Figure 4.8: Drained shear: Cambridge space stress path

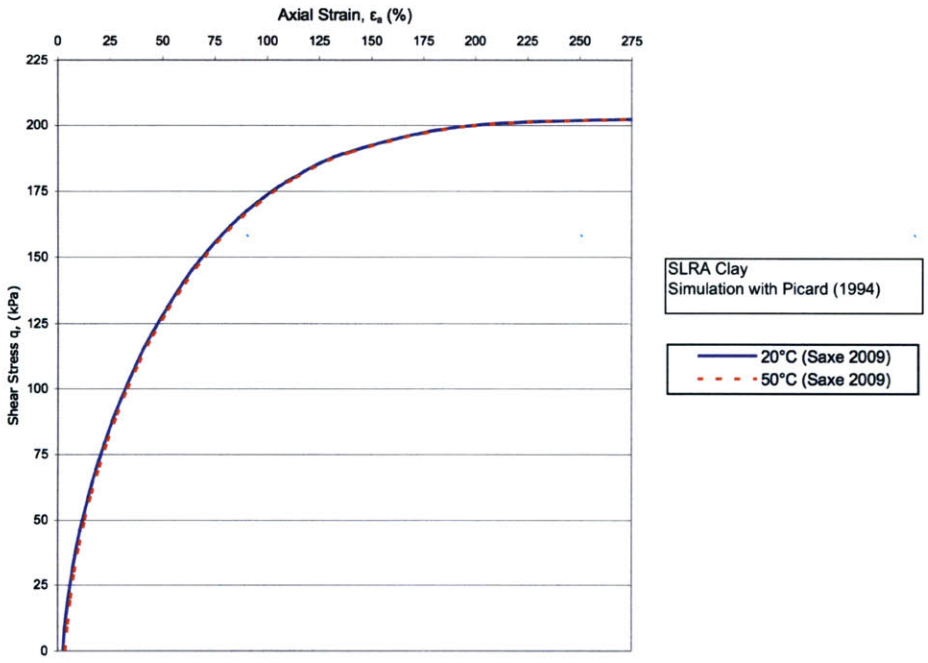


Figure 4.9: Drained shear: q vs axial strain including strain including effects of consolidation

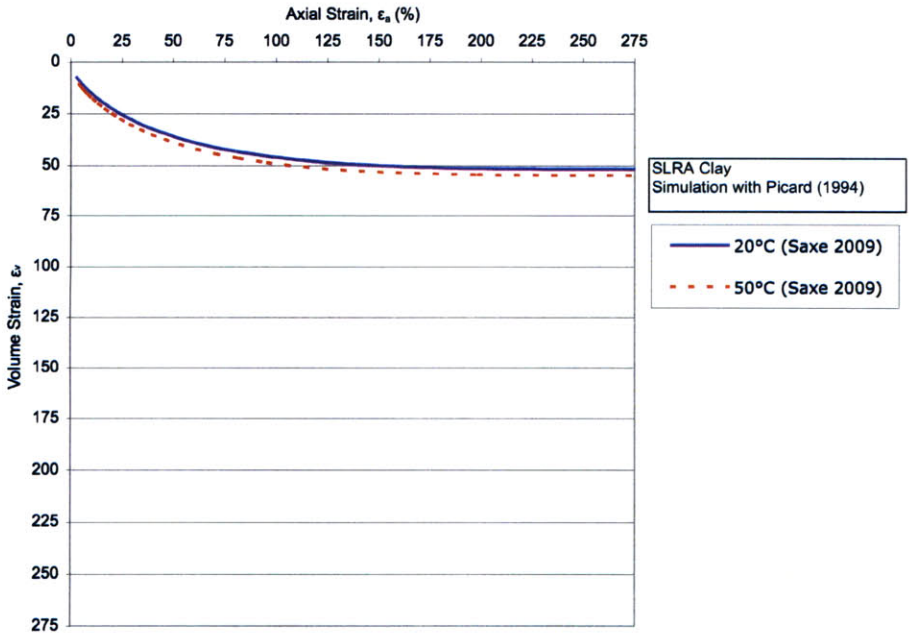


Figure 4.10: Drained shear: volume strain vs. axial strain including effect of consolidation

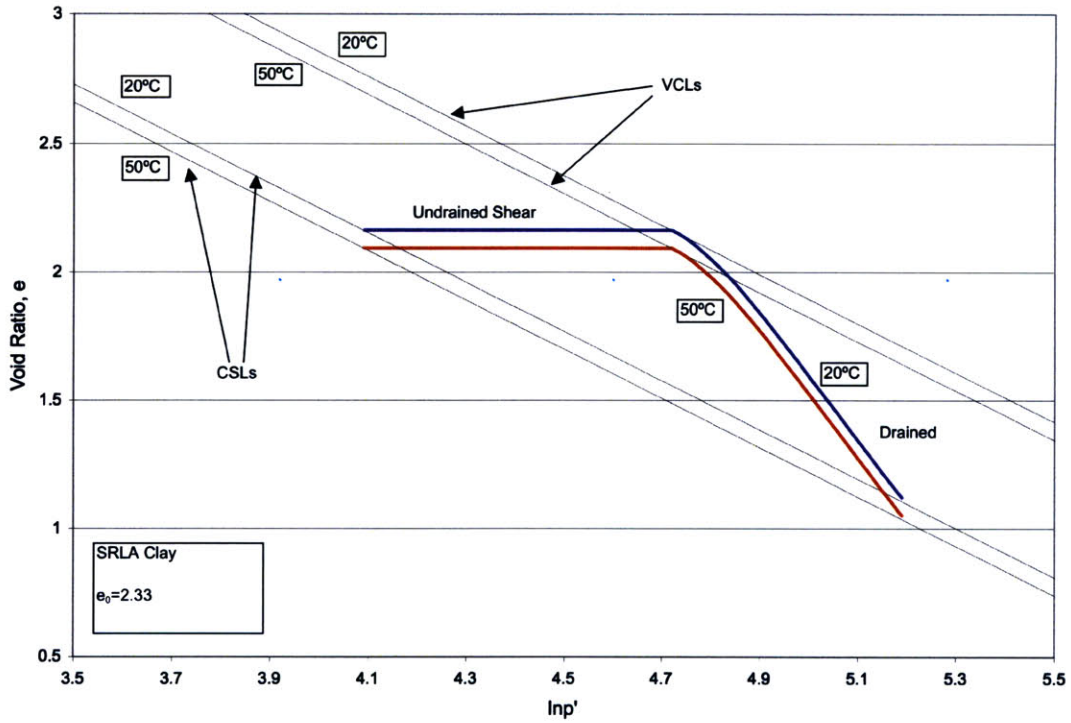


Figure 4.11: Drained shear: void ratio, e, vs lnp'

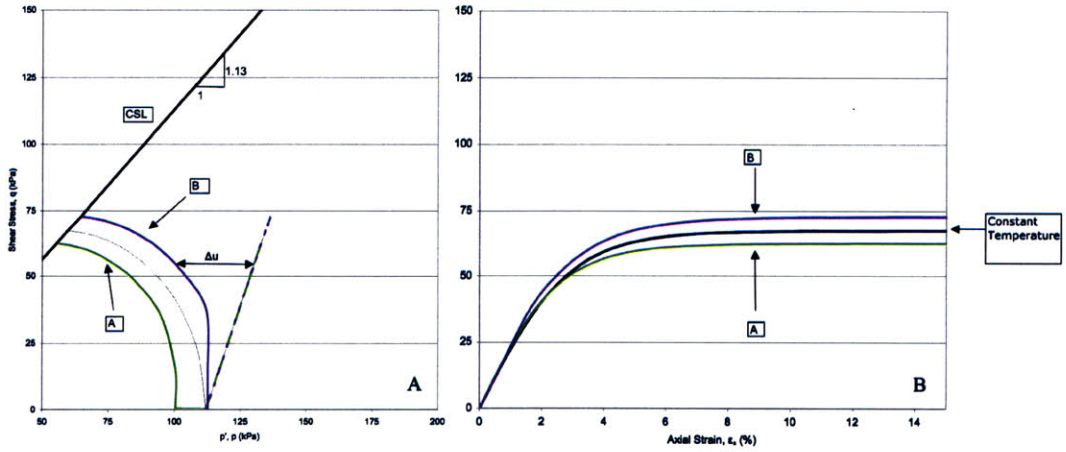


Figure 4.12: Undrained shearing: step change in temperature, ΔT = ±30°C

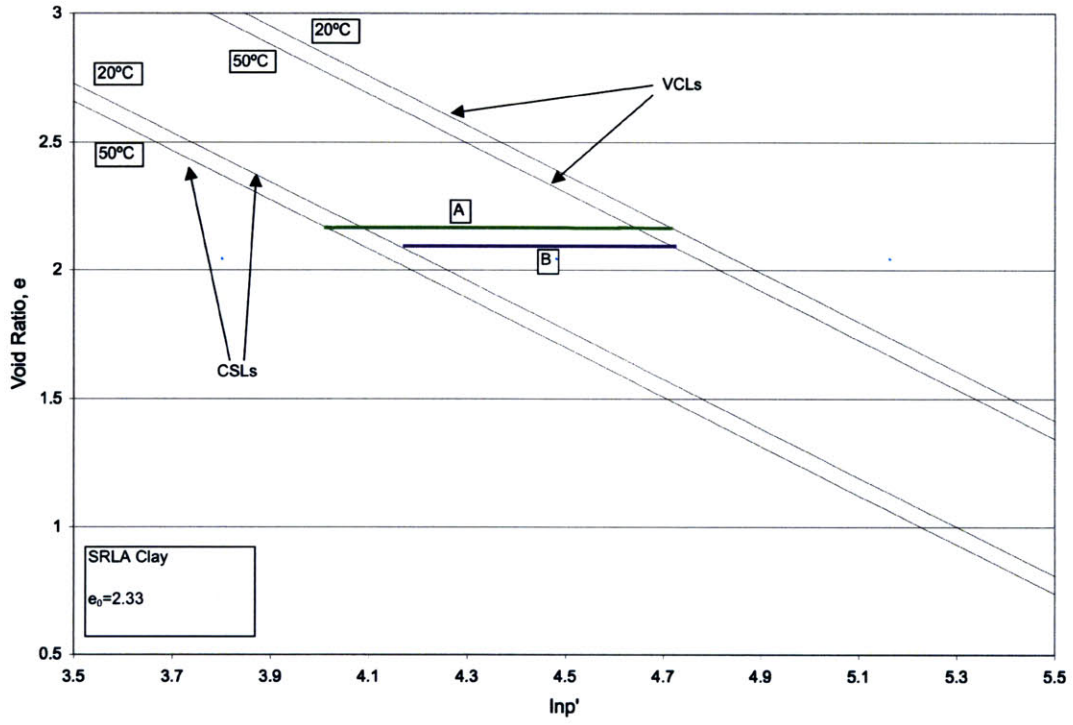


Figure 4.13: Void ratio, e, vs. lnp': undrained samples consolidated at one temperature and sheared after a step change in temperature, $\Delta T = \pm 30°C$

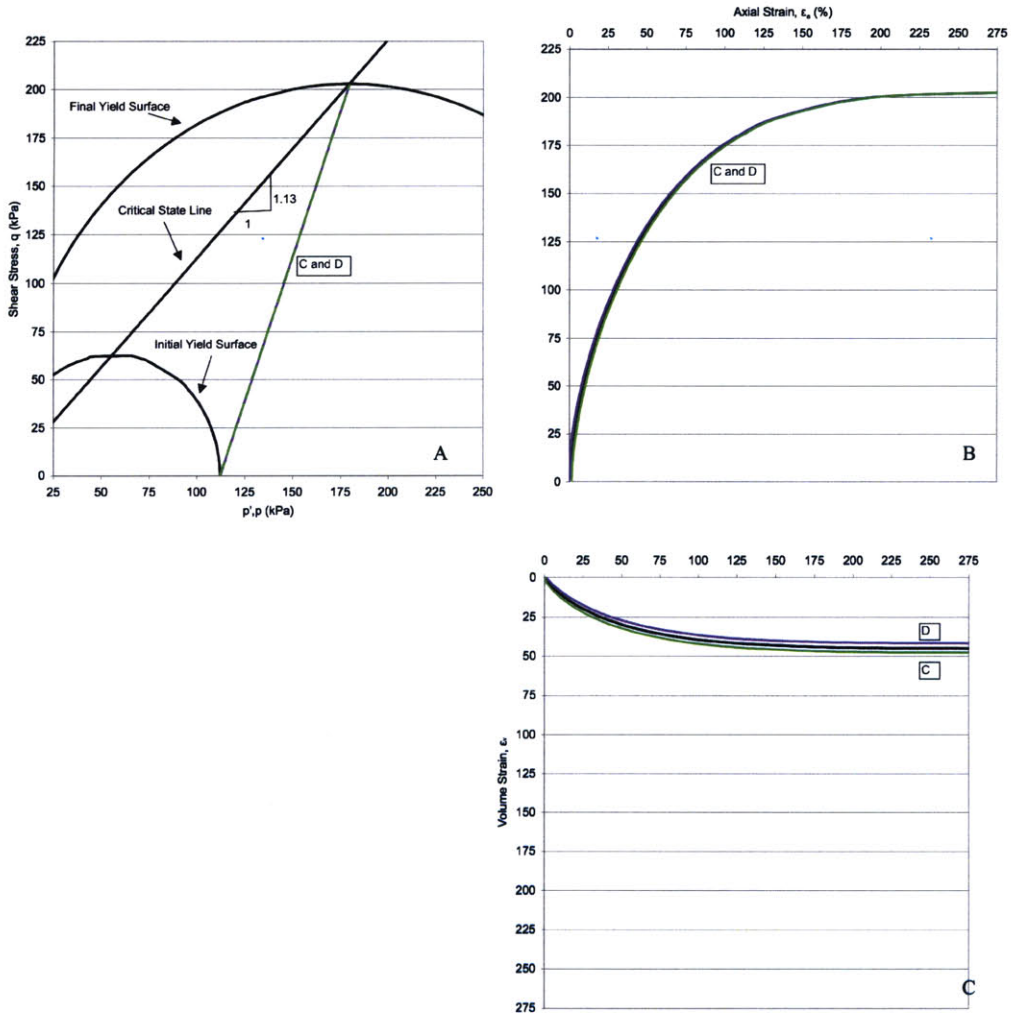


Figure 4.14: Drained shearing of specimens consolidated at one temperature and sheared after a step change in temperature, $\Delta T = \pm 30°C$

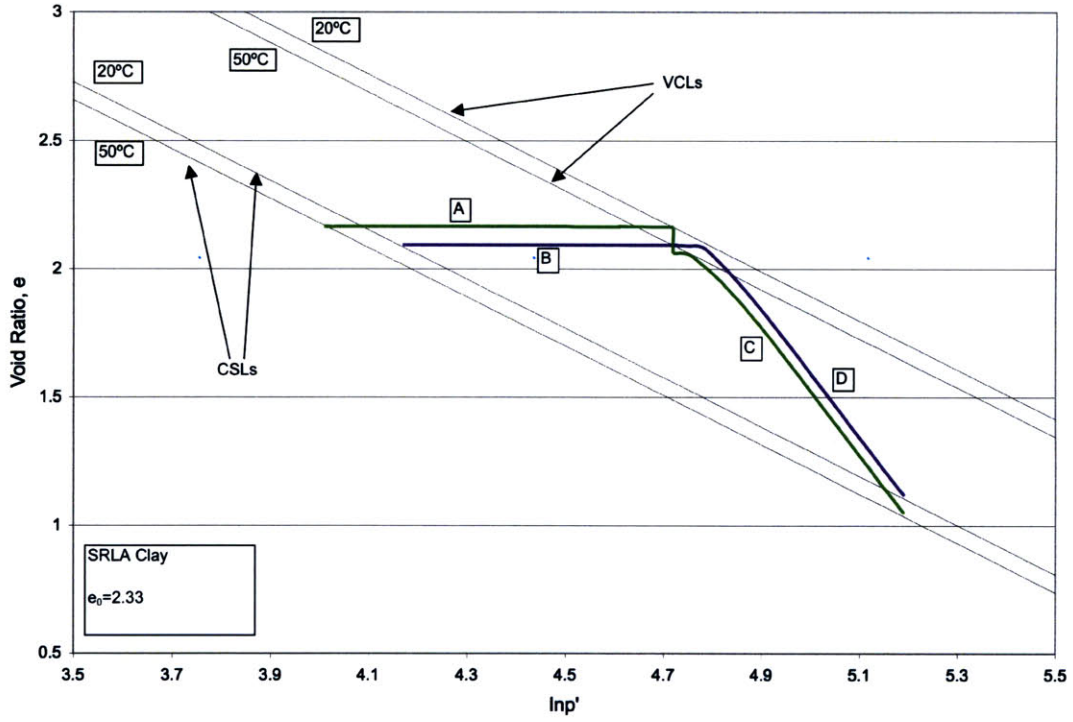


Figure 4.15: Void ratio, e, vs. lnp' for sample consolidation at one temperature and drained sheared after a step change in temperature, $\Delta T = \pm 30°C$

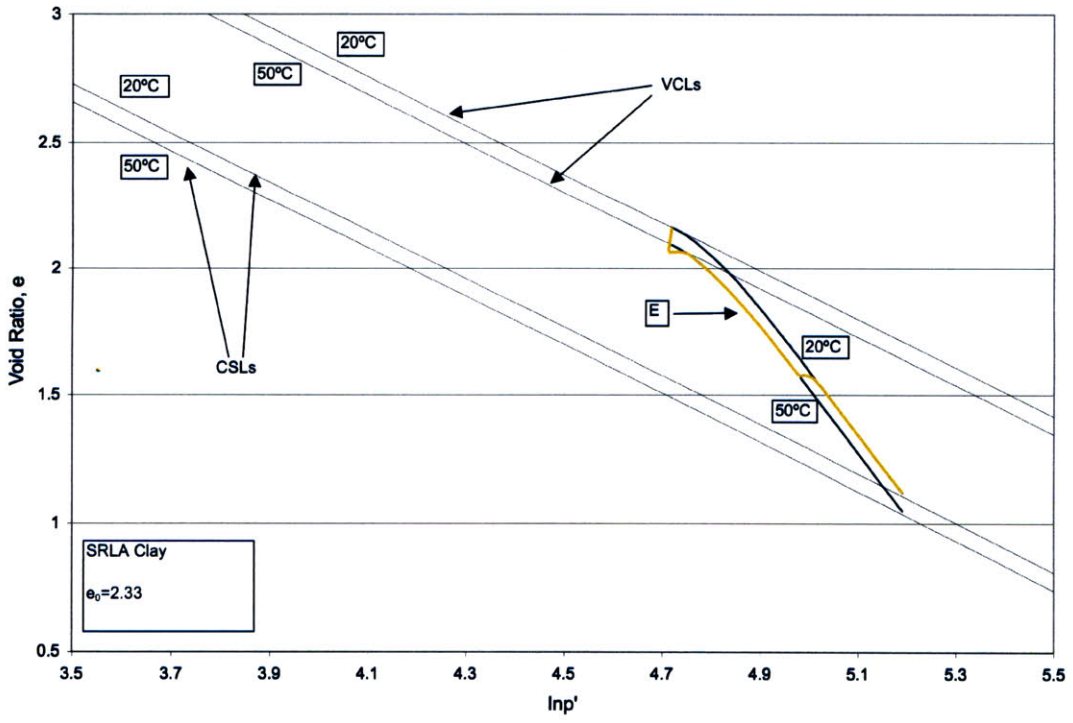


Figure 4.16: Temperature cycle E, void ratio, e vs. lnp'

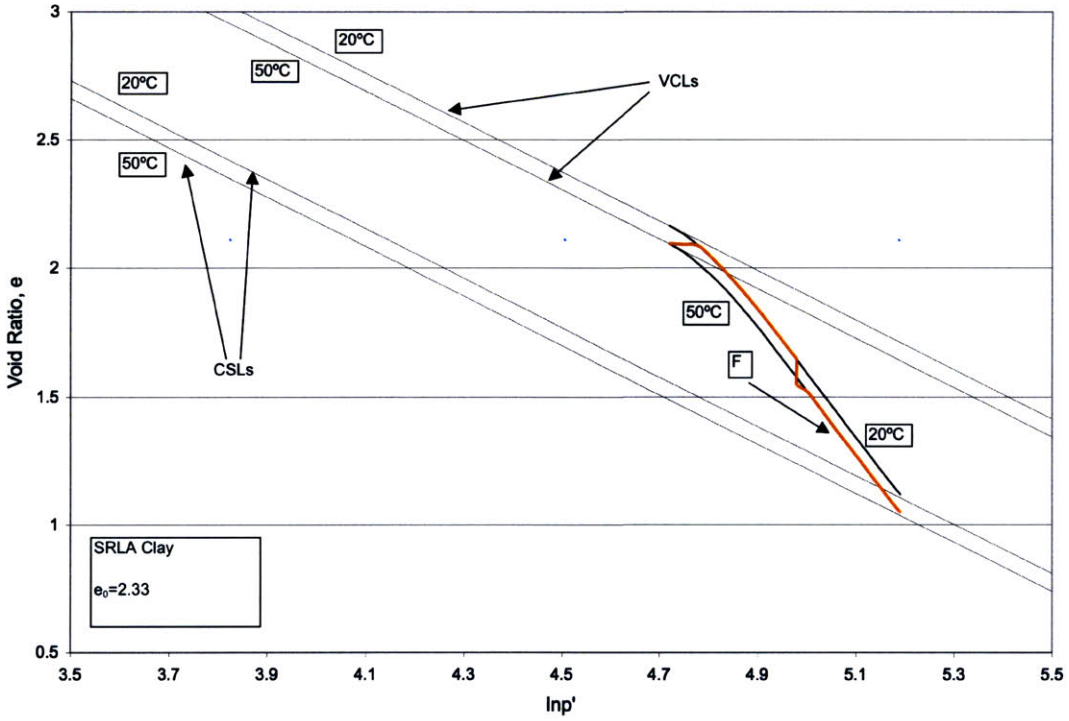


Figure 4.17: Temperature cycle F, void ratio, e vs. lnp'

# 5 MODELING A HEAT STORAGE FIELD

This chapter used the Picard model (1994) with CESAR-LCPC to integrate thermo-mechanical-hydraulic response of the ground associated with ground heat storage systems similar to that investigated by SGI. Two limit cases were considered: 1) a single heat pipe in a semi-infinite field and 2) a heat pipe at the center of a heat storage field. The simulations were evaluated for the effect of temperature storage on pore pressure, stress and deformation within the clay mass. Material behavior is represented using properties identified for NC SRLA Clay in chapter 4.

## 5.1 Numerical Model

Figures 5.1-5.6 summarize the boundary conditions of the two element models considered.

### 5.1.1 Single Heat Pipe

Case 1 evaluated the situation of one heat pipe installed in an otherwise undisturbed clay field of 20m deep NC SRLA Clay. The heat pipe provides the only thermal input to the system and the far field boundaries are significantly removed from the heat source, so as to be unaffected by it. Insulation was used to cover the surface of the heat field, meaning that there is no heat flux across the surface boundary. Drainage was provided at the top and bottom of the clay layer (at y=0 and -20 m). Since it is an axisymmetric simulation, radial displacement was set to 0 at the centerline and vertical displacement is set to 0 at the base of the layer. Figures 5.1, 5.2 and 5.3 illustrate the boundary conditions for Case 1; the heat pipe is shown in red.

### 5.1.2 Heat Pipe at the Center of a Heat Storage Field

Case 2 evaluated the ground response around a heat pipe at the center of a heat storage field, assuming a compact spacing of pipes at 1.2 m center to center. The model assumed equal heat flux applied to all heat pipes; a single representative pipe is considered here. Since each heat pipe had equal thermal influence, the centerline between two heat pipes had a zero heat flux condition. Insulation was used to cover the surface of the heat field, meaning that there was no heat flux across the surface boundary. Drainage was provided at the top and bottom of the clay layer. The right hand boundary is the centerline between two heat pipes, and was constrained horizontally. Figures 5.4, 5.5 and 5.6 illustrate the boundary conditions for Case 2.

## 5.2 Thermal Loading

Two different programs of thermal loading were evaluated for each geometry using similar temperature programs as reported by SGI: 1) Constant temperature and 2) Varying temperature. The temperature control in CESAR-LCPC is generated through the application of a heat flux. For these simulations, a uniform heat flux was applied along the contact boundary between the heat pipe and clay.

### 5.2.1 Constant Temperature

In this thermal program, the soil around the heat pipe was ramped to ~70°C over a span of 50 days and then held constant at T ≈ 70°C for 650 days. In order to heat the clay to 70°C, a constant heat flux in $W/m^2$ was applied along the boundary of the heat pipe. After the first 50 days, the heat flux from the heat pipe was significantly reduced to hold the temperature constant rather than continue to increase.

### 5.2.2 Varying Temperature

The goal of this program was to simulate the thermal cycles experienced by the soil during the natural heating and cooling cycles dictated by the changes in season. The heating and cooling cycles are considered equal in length. The soil was ramped to T ≈ 70°C over 50 days and then cooled to T ≈ 30°C over 50 days. 7 heating/cooling cycles were simulated over a period of 700 days.

### 5.2.3 Soil Parameters

The soil parameters used to test the base cases were passed on the mechanical properties of SRLA. When there was not sufficient information to independently calculate the necessary input parameters, reasonable assumptions were made from parameters for other clays as described in section 4.2. For all the simulations, the ground water level is assumed to be at the surface, and the clay fully saturated. For all the simulations, an assumption of $K_0$=1 was used. Table 5.1 lists the basic input parameters used for SRLA Clay in this section.

$\alpha_o$ is the Thermo-Elastic Compressibility Coefficient. It describes the thermal expansion of the soil particles themselves during heating. This parameter is not affected by stress level or temperature in the Picard model (Picard, 1994). The value for $\alpha_o$ used was taken from Picard 1994. $3\alpha_m$ describes the thermal expansion of the fluid phase of the soil, in this case, water (Picard, 1994). For these simulations, $3\alpha_m$ = 8.8E-05/K was used. $\alpha_p$ is the primary thermal parameter in the model; it describes the thermal hardening/softening of the yield surface with temperature. The contraction/expansion of the yield surface with changing temperature controls the change in settlement and strength behavior of the clay. $\alpha_p$ was determined from the change in preconsolidation pressure from 10°C to 50°C and found to be 1E-3 $K^{-1}$ as discussed in chapter 4.

## 5.3 Hydrostatic Conditions for NC SRLA Clay

It is not possible on the CESAR-LCPC platform to vary preconsolidation stress with depth to characterize a soil profile with constant OCR. A reasonable approximation is used in the model to resolve the competing demands of OCR and gravity, the in situ stress was modeled in step changes. The model was divided into 20 layers, each 1 m thick. The in situ stress and $p'_{co}$ of each layer were constant, giving a constant OCR $\approx$ 1 for the sample, $\sigma' = p'_{co}$, ($K_0 = 1$ case) . At the same time, the in situ stress increases with depth approximating gravity. Figure 5.8 shows the in-situ effective stress in the model. The initial $p'_{co}$ of each layer is the average of the stress in that layer and the one below it.

## 5.4 Single Heat Exchange Pipe

### 5.4.1 Constant Temperature

In order to approximate the constant heat temperature program, a constant heat was applied along the boundary of the heat pipe. During heating to 70°C, the required heat flux was Q=1.1 W/m$^2$. After 50 days, the heat flux was reduced in steps with the goal of maintaining the soil temperature at an average ~70°C. Figure 5.9 shows the applied heat flux with time. The current approach was unable to exactly match the goal temperature program. Each reduction in heat flux, Q, resulted in an oscillation of temperature ($\Delta T \approx$ 5°C). However, the applied Q results in a reasonable approximation of the intended temperature program.

The application of a heat flux to the clay resulted in an increase in temperature, the development of excess pore pressure, and settlement of the clay. Figure 5.10 illustrates the development of pore pressure due to the applied heat flux around the heat pipe. Figure 5.11 shows the extent of the temperature change at 700 days. Figure 5.12 shows

temperature and vertical displacement of the soil surface at the edge of the heat exchange pipe. Figure 5.13 illustrates the development of excess pore pressure with time at the edge of the heat pipe 9 mBGS.

During the initial heating, the clay and water particles expanded causing the soil to swell, a thermo-elastic response. The initial expansion was followed by settlement due to the contraction of the yield surface (a reduction in $p_c$), and the dissipation of the thermally induced excess pore pressure. The large mass of the soil compared to the area directly affected by the heat pipe mitigated the effect of the thermal load. The heat energy applied radiated through the large mass of soil. The heat energy induced excess pore pressure and resulting deformation spread out over a large soil volume and so at any given point have only small effects. Figure 5.11 shows the extent of the spread of the increased temperature field after 700 days. The heat pipe has a radius of 0.1 m and is 10 m long. The cross section of clay modeled has a radius of 30 m and is 10 m deep. After 700 days of heating, the vertical settlement next to the heat pipe is less than 0.1 mm.

## 5.4.2 Fluctuation of Temperature

The one heat pipe in the Case 1 simulation was surrounded by a very large amount of clay. This clay had a large associated thermal mass and thermal inertia. This exerted a significant cooling load on the soil near the heat pipe. It was not possible to perform a simulation of fluctuating temperature between 70°C and 30°C for Case 1. Once the heating load was turned off, the clay adjacent to the heat pipe returned to a temperature of ~15°C with no cooling load applied. Figure 5.14 shows the temperature and displacement development of the clay after the heat flux is turned off. This inability to store heat in the clay around the single heat pipe made it impossible to test the fluctuating temperature case. In the fluctuation temperature program, it is presupposed that it is possible to extract heat from the ground during the heat season (winter). In this geometry, an extraction of heat from the ground would drive the ground temperature below the annual average in situ temperature, 10°C.

## 5.5 Heat Exchange Pipe at Center of Heat Storage Field

In Case 2, the effects of the applied heat flux are contained in a much smaller soil mass, so the applied heat is unable to radiate away. The heat pipe had a radius of 0.1 m and is 10 m deep. The soil column is 0.6 m and 20 m deep, reflecting a center-to-center heat pipe spacing of 1.2 m.

### 5.5.1 Constant Temperature

For Case 2 a much smaller constant heat flux, Q=0.2 W/m$^2$, was needed to heat the soil to 70°C over 50 days (vs. Q=1.1 W/m$^2$ in Case 1). After 50 days, a much smaller heat flux was needed to maintain the clay at 70°C, Q= 0.025 W/m$^2$ (versus 0.77 W/m$^2$ in Case 1). Figure 5.15 shows the temperature and heat flux input for Case 2 at constant temperature.

Figure 5.16 shows temperature and vertical displacement of the soil surface at the centerline between two adjacent heat pipes. In this case, the ground surface at r = 0.6 m swells 3 cm before undergoing a net contraction of 3.6 cm after 700 days. Figure 5.17 illustrates the development of excess pore pressure with time along a vertical cross section at r=0.1m

In Case 2, the temperature changes and corresponding excess pore pressure were confined to a much smaller soil volume and therefore had significantly larger effects. During the initial heating, the soil swelled 3 cm due to thermal expansion of the clay and water molecules. After the initial expansion, the soil settled as the pore water dissipated. Over 700 days the net settlement was 3.5 cm and the excess pore pressure was 0.5 kPa. This corresponds to an average vertical strain, $\varepsilon_v$ = 1.75% or 3.5%, if we consider the entire clay layer or just the heated upper 10 m, respectively. This constriction of the heat loads led to higher temperature effects with a smaller applied heat flux. During the initial heating period, the excess pore pressure in the sample grew to, $\Delta u$ = 9 kPa, Figure 5.17. Once the applied heat flux was reduced, to maintain the clay at 70°C, the excess pore

pressure stopped increasing and began to dissipate. This dissipation of excess pore pressure caused consolidation in the clay.

Displacement of the clay layer occurs due to two competing phenomena: the thermal expansion of the clay itself (thermo-elastic) and consolidation due to the shrinking of the yield surface (thermo-plastic). During the first 50 days of this simulation, the expansion of the clay dominated; later the thermo-plastic consolidation of the clay, due to shrinking of the yield surface, was the dominant factor.

### 5.5.2 Fluctuating Temperature

In Case 2, the input heat is confined to a much smaller area and cannot radiate away, making it possible to store heat. It was possible to model the effects of fluctuation in temperature due to the shift between heating and cooling. The bottom end of the layer is the only exposure to clay mass at 10°C. The influence of thermal inertia in Case 2 is very small compared to Case 1. Figure 5.18 shows the temperature change after 50 days if no more heat is added. The input heat is very well conserved in the clay mass, making heat storage, and therefore heat extraction, possible.

The amount of heat needed to reach 70°C was 0.2 $W/m^2$, as in the constant heat program. To then reduce the temperature to 30°C, a heat flux of -0.125 $W/m^2$ was applied. To cycle back to 70°C, the applied heat flux was 0.126 $W/m^2$. This indicates that some input heat was lost to the boundary and unrecoverable. At the same time, the temperature of the clay drifted lower over the cycles, indicating that, over time, more heat is lost to the boundary. Figure 5.19 shows the heat flux with time and the corresponding temperature.

Figure 5.20 shows the fluctuation of temperature with time and the corresponding vertical displacement at the surface midway between 2 adjacent heat pipes. Figure 5.21 illustrates the fluctuation of the excess pore pressure induced by the heating/cooling cycles.

During each heating cycle, the clay expanded and, during each cooling cycle, the clay contracted. However, there is an overall trend of settlement. This is due to the expulsion of the excess pore pressure built up during the heating cycles. At the end of the $7^{th}$ heat/cool cycle, the net settlement of the clay was 6 cm. This is larger than in Case 2 – with constant temperature. It is important to note that the 6 cm includes the contraction of the clay during cooling only. If the sample was heated back to 70°C, the clay would expand again and the net vertical displacement would significantly smaller. At the end of the last heating phase, at 650 days, the net vertical settlement was 3 cm. In contrast with a ramped temperature held at 70°C (Figure 5.16), at 650 days, the net vertical settlement is 3.25 cm. The vertical displacement is completely in phase with the shifts in temperature. As the temperature rises, the clay expands and, as the temperature cools, the clay contracts. The net effect is a drift towards consolidation. The net contraction of the soil is larger than the net expansion.

## 5.6 Parametric Study

The goal of this section is to evaluate how changes in different parameters important to the thermo-poro-mechanical coupling affect the soil response around the heat exchange pipe. Five different parameters are considered in the following section:

1) Hydraulic conductivity, k;
2) The coefficient of thermal hardening, $\alpha_p$;
3) The volumetric heat capacity, $C_v$;
4) Overconsolidation ratio, OCR;
5) Spacing between adjacent heat pipes.

For the purposes of this parametric study, most of these simulations focus on the constant temperature case, with the exception of OCR with the fluctuating temperature program.

### 5.6.1 Hydraulic Conductivity, k

The hydraulic conductivity of the clay determines how fast the thermally induced excess pore pressure can dissipate. Figure 5.22 shows that smaller excess pore pressures are generated when the hydraulic conductivity is increased. Figure 5.23 illustrates the effect a one order of magnitude increase in thermal conductivity of the clay has on the deformation behavior with time. After 50 days, the excess pore pressure generate at k = $2.5x10^{-8}$ m/s was 2 kPa (rather than 9 kPa at the reference k = $2.5x10^{-9}$ m/s). The increased hydraulic conductivity led to a faster initial rate of excess pore pressure dissipation. The initial swelling of the sample during the initial heating was reduced; the accelerated rate of consolidation of the clay counteracted the thermal expansion of the clay. The initial swelling was reduced from 3 cm to 0.5 cm. Over time, as the excess pore pressure dissipated, the rate of settlement at elevated k approached that observed for the reference case. Over the 700 day period, at k=$2.5x10^{-8}$ m/s the surface settlement was nearly 5 cm at r=0.6 m, 1.5 cm larger than the base case simulation.

### 5.6.2 Thermal Hardening Parameter, $\alpha_p$

The thermal hardening parameter, $\alpha_p$, controls the amount of contraction of the yield surface with heating. The larger $\alpha_p$, the more sensitive the clay will be to changes in temperature. In the standard parameter set, $\alpha_p=10^{-3}$ $K^{-1}$. To evaluate the effect of this parameter, simulations were carried out with $\alpha_p = 10^{-4}$ $K^{-1}$. Figures 5.24 and 5.25 show the changes in excess pore pressure and displacement due to this change in $\alpha_p$. The effect on excess pore pressure is relatively small; however, there is a much larger change in displacement. For $\alpha_p = 10^{-4}$ $K^{-1}$, the amount of consolidation strain is greatly reduced. The clay recovered from the initial swelling but did not consolidate any further. The net displacement is nearly 0.0 cm at t = 700 days.

## 5.6.3 The Volumetric Heat Capacity, $C_v$

The volumetric heat capacity used in the standard parameters is $C_v$=2.16x10$^6$ J/m$^3$K. As discussed in Chapter 2, the range of $C_v$ for clays is not very large. In this section, a change to $C_v$ = 2.0x10$^6$ J/m$^3$K is investigated. The decrease in $C_v$ means that, for a set volume, a smaller amount of heat energy is needed to change the temperature of the clay. For this simulation, the heat influx input was not changed. This resulted in consistently higher temperatures in the clay. Figure 5.26, shows the excess pore pressure in the system at 50 and 450 days. Figure 5.27 shows the displacement and temperature response with time. As a direct result of the higher temperatures, the peak excess pore pressure at 50 days was also higher, by ~0.5 kPa. This increase in excess pore pressure resulted in more consolidation and a larger net displacement of the clay. The increase in temperature also resulted in more thermal expansion. After 50 days, the displacement of the clay was a swelling of 3.2 cm. The net displacement after 700 days was 4.1 cm contraction.

## 5.6.4 Overconsolidation of Clay

One of the powerful effects of thermally loading a soil is that the response can drive an over-consolidated soil into a normally consolidated range of behavior. The cases discussed above were all evaluated in the normally consolidated condition. It is comparatively rare to find a soil that is truly normally consolidated in situ, especially at the surface (due to the effects of aging etc). Even very soft soils have some small preconsolidation. To evaluate the effects of OCR, the Case 2 - fluctuating simulation was re-run with initial OCR =1.2. Figure 5.28 shows the change in pore pressure when OCR = 1.2. Figure 5.29 shows the displacement behavior of the clay. The initial positive excess pore pressure was the same but the negative excess pore pressure was lower for the OC case. Due to the higher OCR, the net displacement decreased; after 700 days the net displacement was a 1.4 cm contraction as opposed to 6 cm at OCR=1.0.

### 5.6.5 Spacing

The spacing of the heat pipes has a serious effect on thermo-mechanical coupling. Case 1 showed how a single heat pipe causes negligible pore pressure and displacement in the clay even at high temperature. Case 2 showed that constraining input heat into a 0.5 m radius cylinder around the heat pipe (center to center spacing of 1.2 m) led to significant build up of pore pressure. To evaluate the effect of spacing, Case 2 at constant temperature was repeated with the center-to-center spacing of the heat pipes at 2 m. The boundary conditions for Case 2 were used for this model.

At the wider spacing with the same input heat flux, Q, the resulting temperature change was much smaller. The temperature in the clay at the midpoint between two heat pipes rose to 33°C rather than 74°C at 1.2 m spacing. Figure 5.30 shows the input heat flux and the resulting temperature change with time for both 1.2 and 2 m center-to-center spacing of the adjacent heat pipes. The temperature increase is smaller for 2 reasons: 1) The soil mass heated by each heat pipe is 167% larger and 2) a larger area at the bottom of the soil column radiates heat to the groundmass unaffected by the heat pipe.

As a direct result of the lower soil temperature, much less deformation takes place in the clay at the 2 m spacing. Figure 5.31 shows the change in deformation at the midpoint between 2 heat pipes at 1.2 and 2 m spacing. For the same input energy, the deformations at 2 m spacing are much smaller. The net settlement after 700 days is 0.5 cm at 2 m rather than 3.6 at 1.2 m.

The spacing of the heat pipes is directly proportional to the concentration of heat and associated deformations. The more closely spaced the heat pipes, the less energy is radiated to the surrounding soil. The heat pipe spacing of any given project should be optimized to limit the number of heat pipes and associated cost while maximizing the retained portion of input heat.

## 5.7 Simulating a Year Long Heating and Cooling Cycle

All of the tests above have dealt with heating and cooling of the clay on accelerated timelines. In practice, the heating and cooling of the clay in a heat storage field is tied to the seasonal changes in outdoor air temperature. During the warm season, excess heat will be exhausted to the ground providing cooling. In the cold season, heat will be drawn from the ground to provide heating. A heat storage field is most likely to serve a commercial building; the heating and cooling of a theoretical office building using a heat store is examined here in the Boston, MA climate. Figure 3.32 shows typical weather data for Boston, MA (US DOE, 2009).

Due to the high concentration of people and equipment (computer, lights, etc) in an office, commercial buildings tend to need cooling the majority of the year. For this simulation, the following conditioning needs were assumed:

1) 186-day cooling period;
2) 45-day period with neither heating nor cooling;
3) 90-day heating period;
4) Second 45-day period with neither heating nor cooling.

During the cooling period, excess heat from the building was exhausted to the ground, heating the clay. During the heating period, heat was extracted from the clay to heat the building. During the cooling and heating periods, a heat flux, Q= 0.05 $W/m^2$ and -0.06 $W/m^2$ were applied to the soil. Figure 5.33 illustrates the temperature and displacement with time for the one-year period. There was an offset in temperature; from the start of the year to the end of the year, the soil was nearly 20°C warmer. Ideally, the average annual soil temperature in a heat store should be kept constant. In order to achieve this, less air-conditioning can be supplied by the heat store, minimizing the amount of heat rejected to the ground. A better option would be to increase the amount of heat extracted from the ground, thereby maximizing the conditioning energy given by the heat store and achieving a constant annual average ground temperature. Using the heat store to heat

more space, to heat the same space warmer or to heat hot water needs year round, would use more heat energy and help balance the yearly heat extraction/rejection cycle.

During the heating phase, the clay swelled 1 cm initially and then began to be dominated by thermally induced consolidation. Consolidation continued during the period of no thermally loading due to the sustained high temperature of the soil. During the cooling phase, the consolidation of the clay continued as the clay was still warmer than the initial temperature; the yield surface remained contracted. Over one year of operation, there was 3.5 cm of net settlement in the clay.

Table 5.1: Picard Model input parameters for SRLA Clay

| | | | |
|---|---|---|---|
| *Physical Properties* | | | |
| Buoyant Density | $\rho_{bouyant}$ | $kN/m^3$ | 5.0 |
| Fluid Density | $\rho_{fluid}$ | $kg/m^3$ | 1000 |
| Porosity | n | | 0.7 |
| | | | |
| *Conduction Properties* | | | |
| Permeability $K_{xi}=K_{yi}=K_{zi}$ | $k_{x\text{-}intrinsic}$ | $m^4/kNs$ | 2.5E-12 |
| Thermal Conductivity $K_{xT}=K_{yT}=K_{zT}$ | $k_{x\text{-}thermal}$ | W/m/K | 1.7 |
| | | | |
| *Material Properties* | | | |
| *Poro-Elastic* | | | |
| Young's Modulus | E | Pa | 14.2p' |
| Poisson's Ratio | $\nu$ | | 0.35 |
| Biot Coefficient | b | | 1 |
| Biot Modulus | $M_{biot}$ | Pa | 4.40E+09 |
| Skempton's Coefficient | $\beta$ | | 1 |
| *Thermo-Elastic* | | | |
| Thermo-Elastic Compressibility Coefficient | $\alpha_d$ | $K^{-1}$ | 1.00E-05 |
| Thermal Expansion Coefficient | $3\alpha_m$ | $K^{-1}$ | 8.80E-05 |
| *Thermo-Plastic* | | | |
| Slope of the Critical State Line | M | | 1.13 |
| Coefficient of Plastic Strain Hardening | $V=(1+e_0)/(\lambda-\kappa)$ | | 2.77 |
| Coefficient of Thermal Hardening | $\alpha_p$ | $K^{-1}$ | 1.00E-03 |
| Volumetric Heat Coefficient | $C_v$ | $J/m^3K$ | 2.16E06 |
| | | | |
| *Other* | | | |
| Preconsolidation Pressure | $P'_{c0}$ | Pa | 1.11E+05 |
| Reference Temperature | $T_o$ | Deg C | 10 |

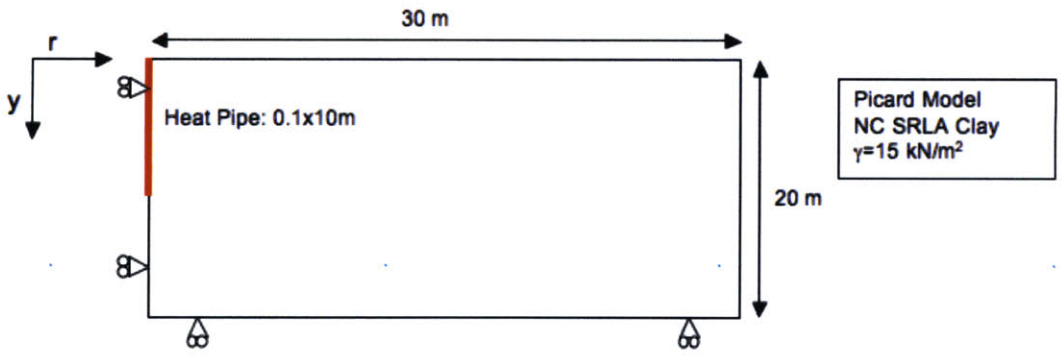


Figure 5.1: Mechanical boundary conditions for Case 1

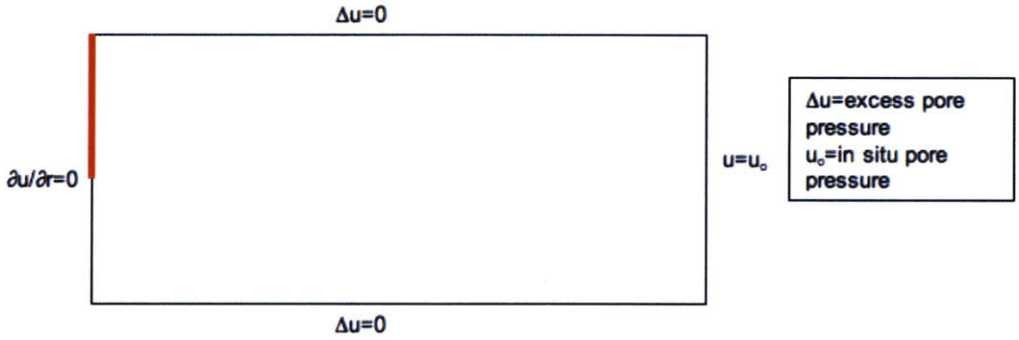


Figure 5.2: Drainage boundary conditions for Case 1

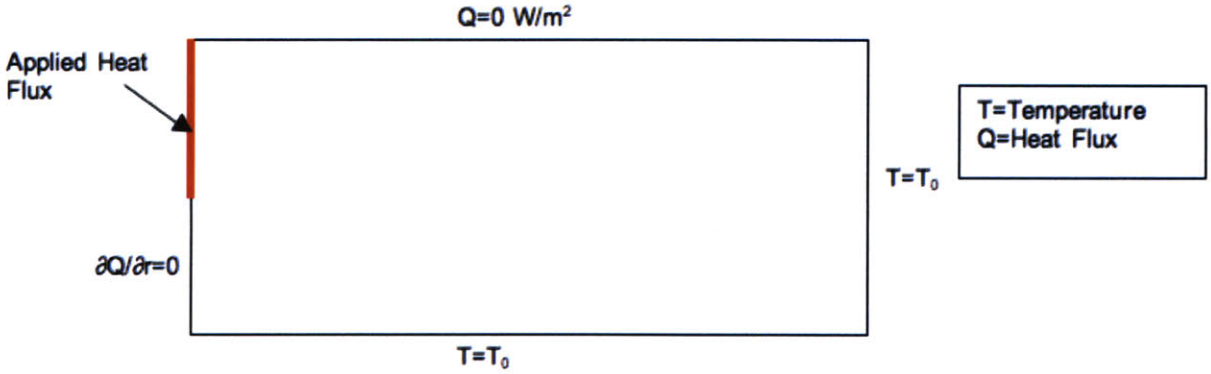


Figure 5.3: Thermal boundary conditions for Case 1

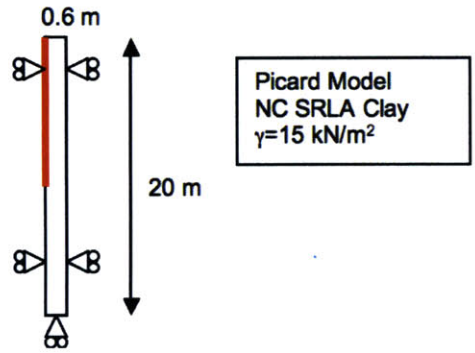


Figure 5.4: Mechanical boundary conditions for Case 2

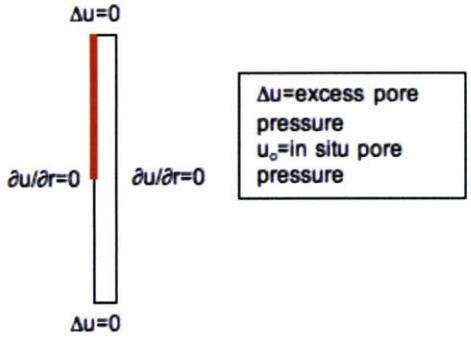


Figure 5.5: Drainage boundary conditions for Case 2

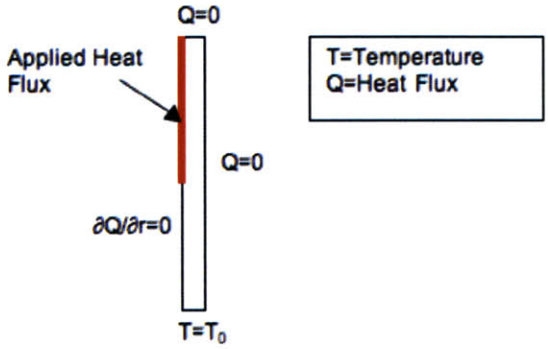


Figure 5.6: Thermal boundary conditions for Case 2

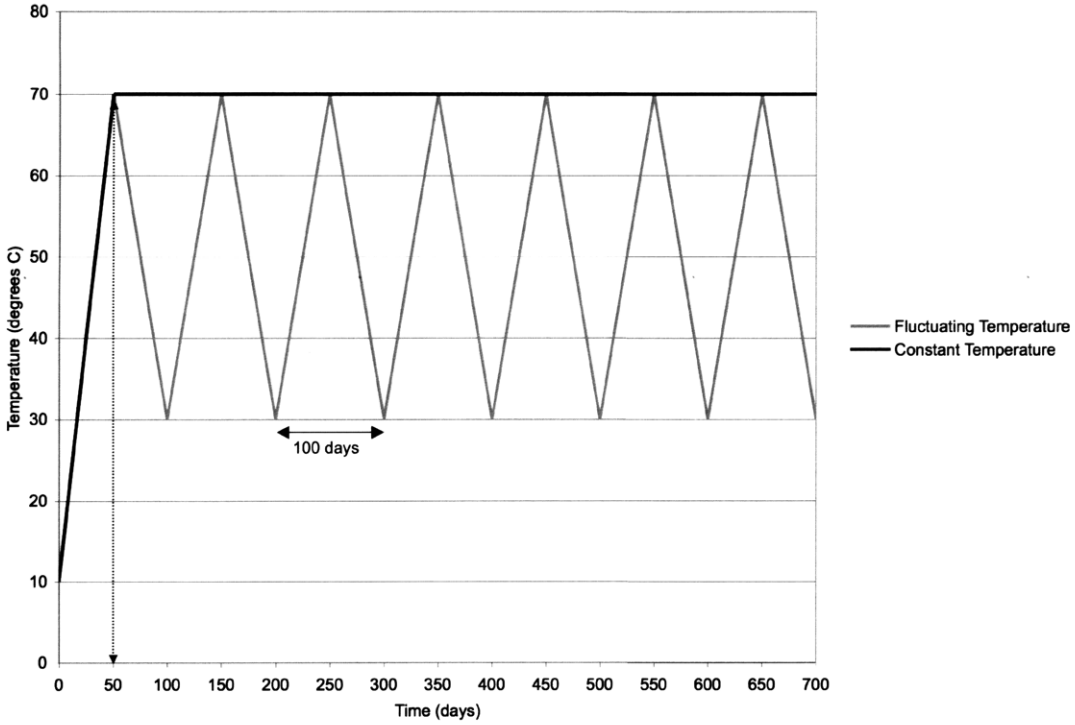


Figure 5.7: Ideal temperature with time for the two temperature programs for simulated heat pipe

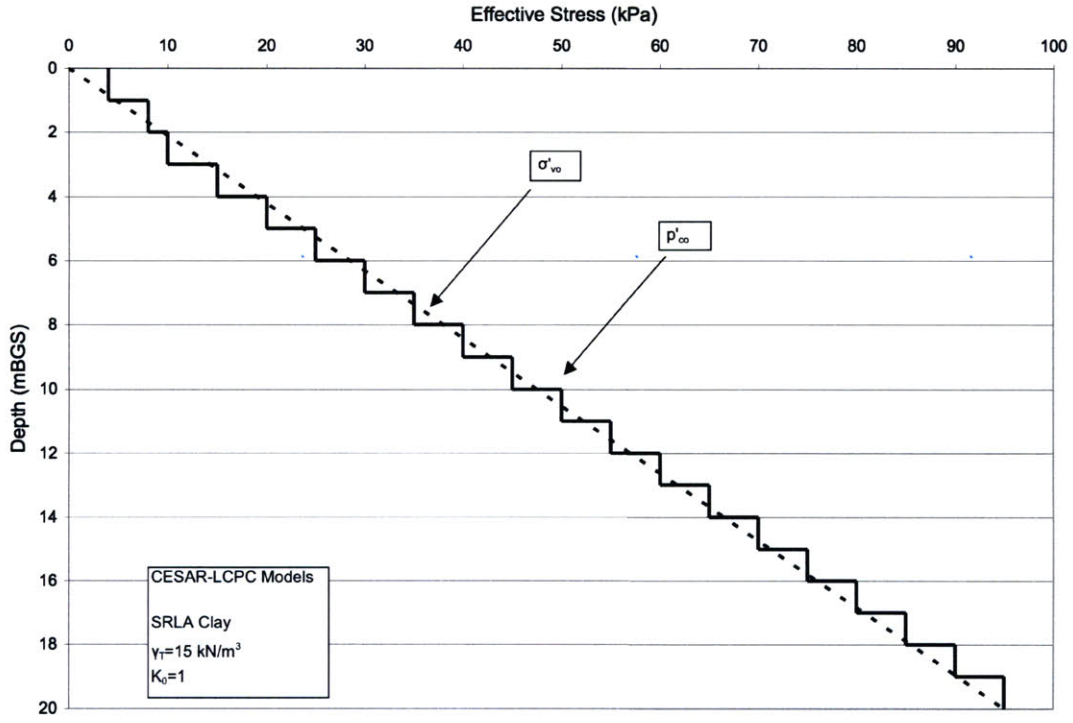


Figure 5.8: Model in-situ effective stress

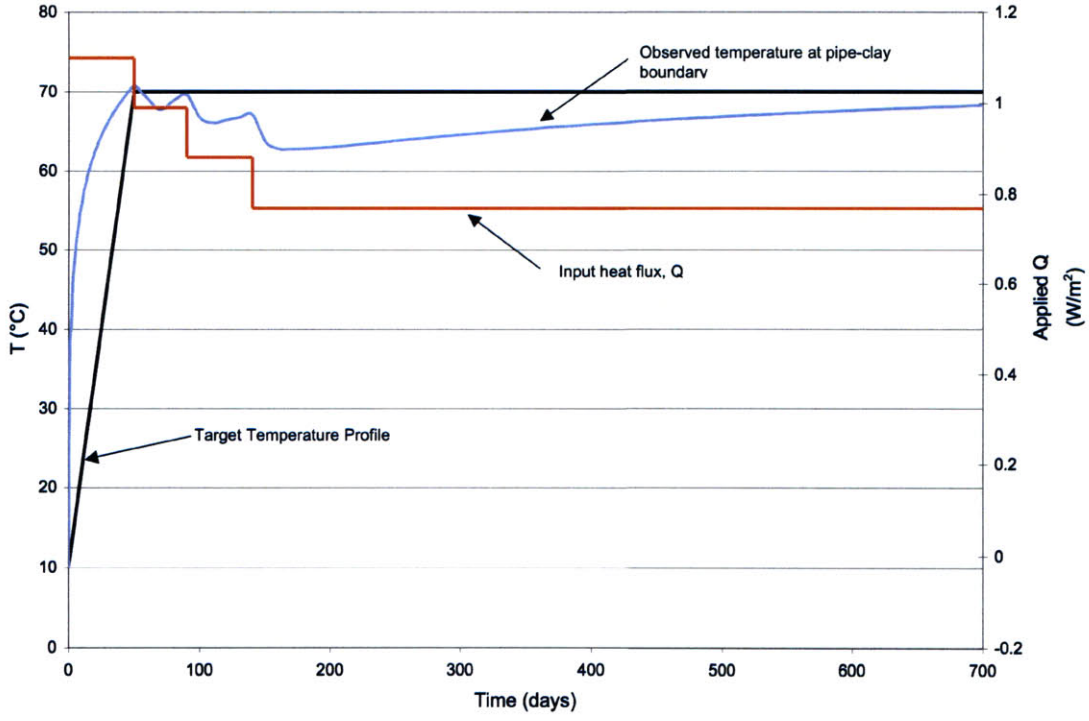


Figure 5.9: Simulation constant temperature-time conditions for a single heat exchange pipe using CESAR-LCPC

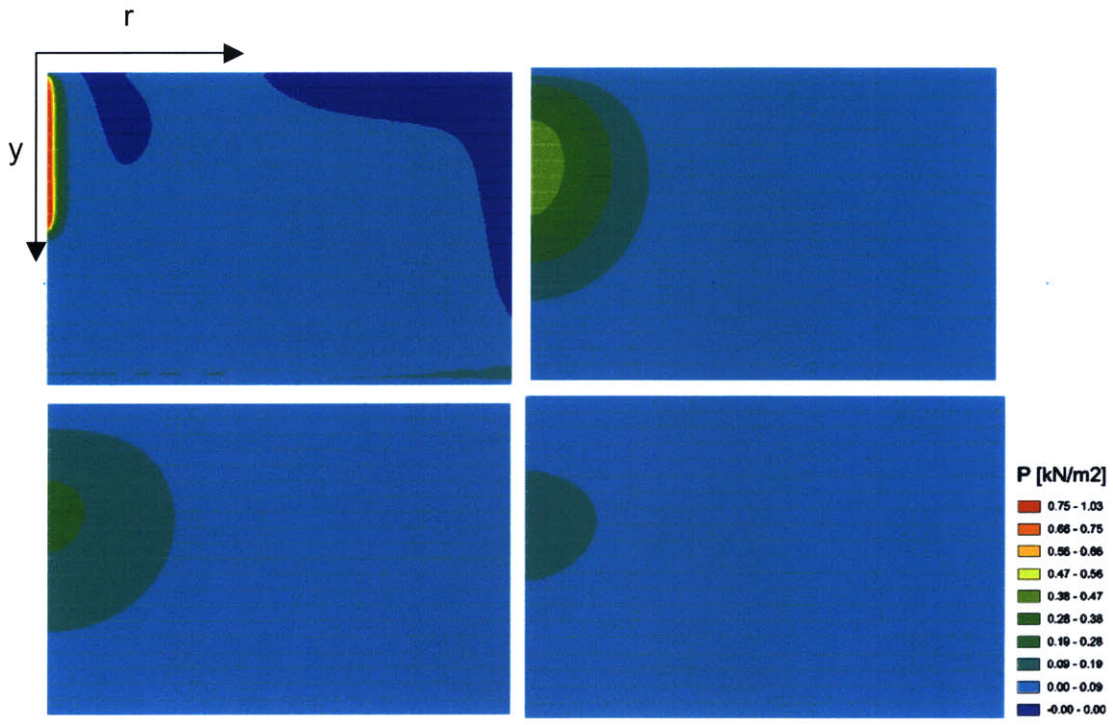


Figure 5.10: Case 1 single heat pipe: development of pore pressure around heat pipe at day 1, day 50, day 150 and day 300 (Each frame 30 x 20 m)

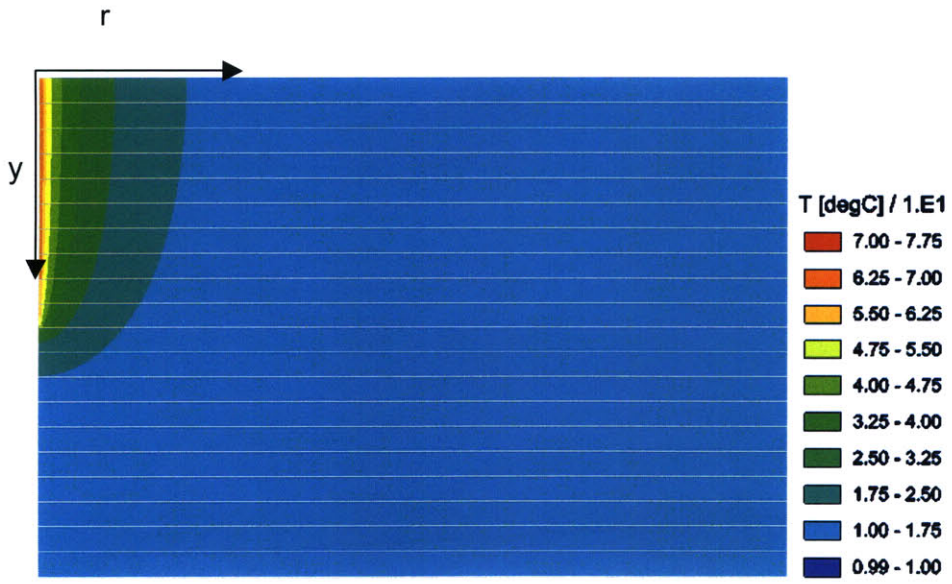


Figure 5.11: Case 1 single heat pipe: temperature Distribution in the clay after 700 days (Frame 30 x 20 m)

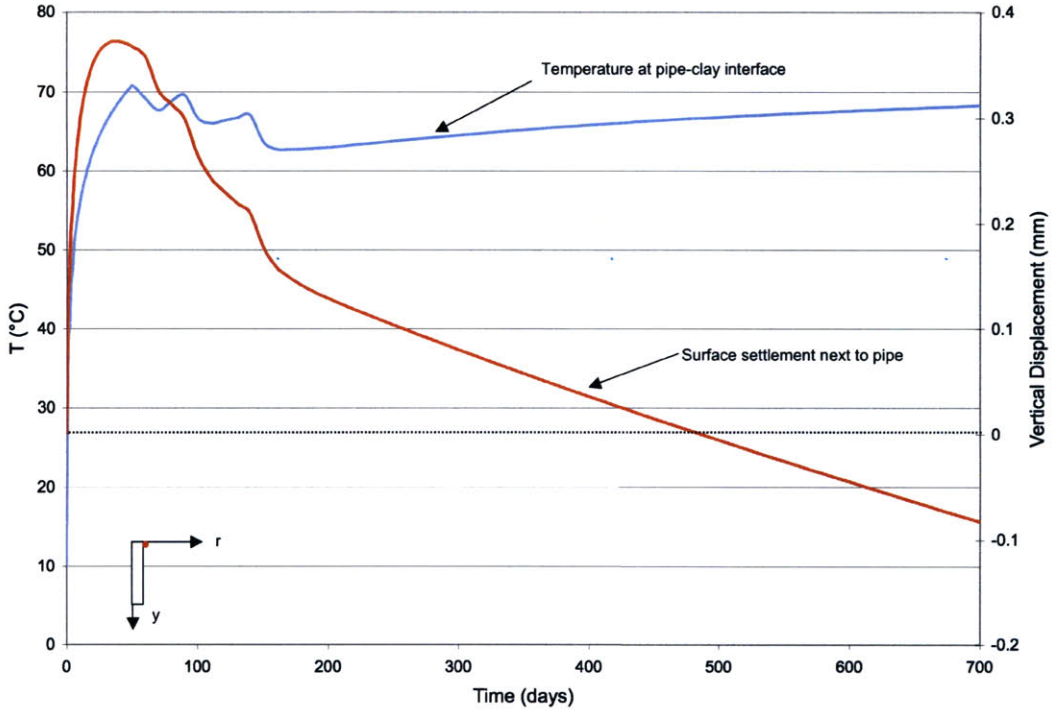


Figure 5.12: Case 1 single heat pipe: Temperature and displacement evolution with time

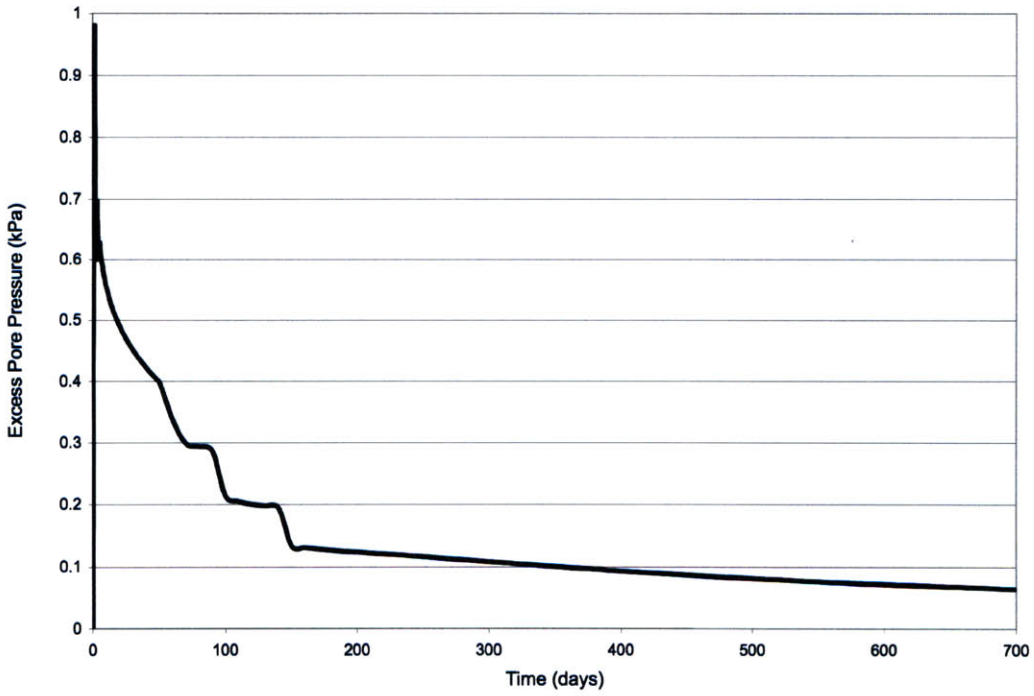


Figure 5.13: Case 1 single heat pipe: excess pore pressure with time at point (r,y) = (0.1,-9)

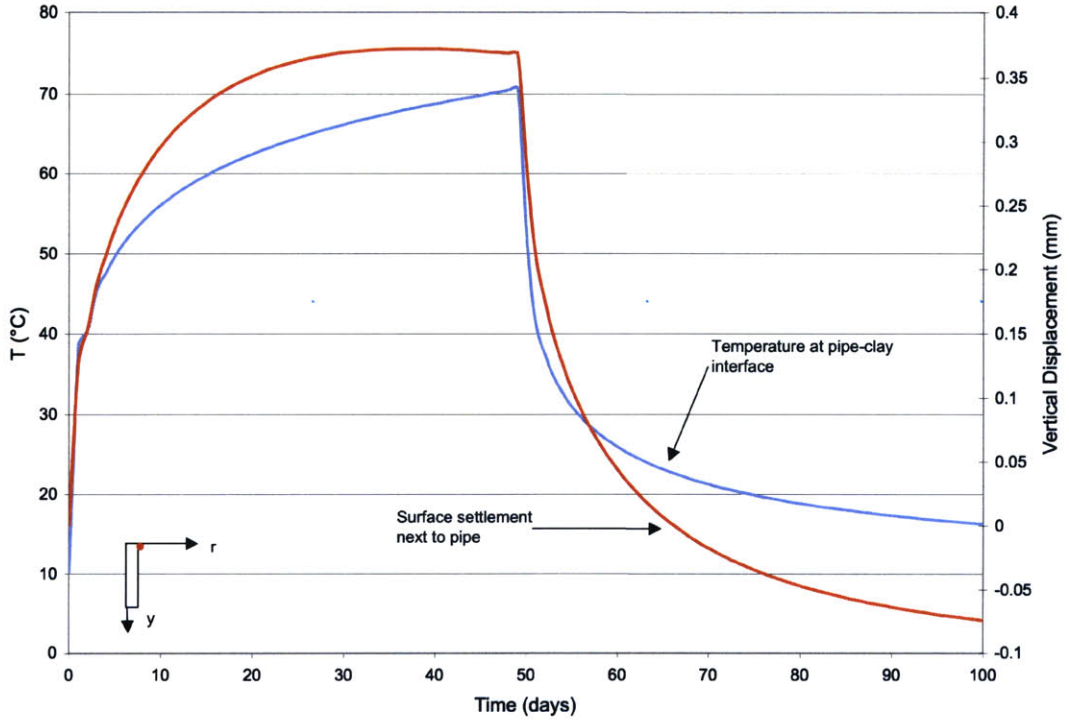


Figure 5.14:Case 1 single heat pipe: temperature and vertical displacement development with time for 50 day heating period and 50 days after heat is turned off

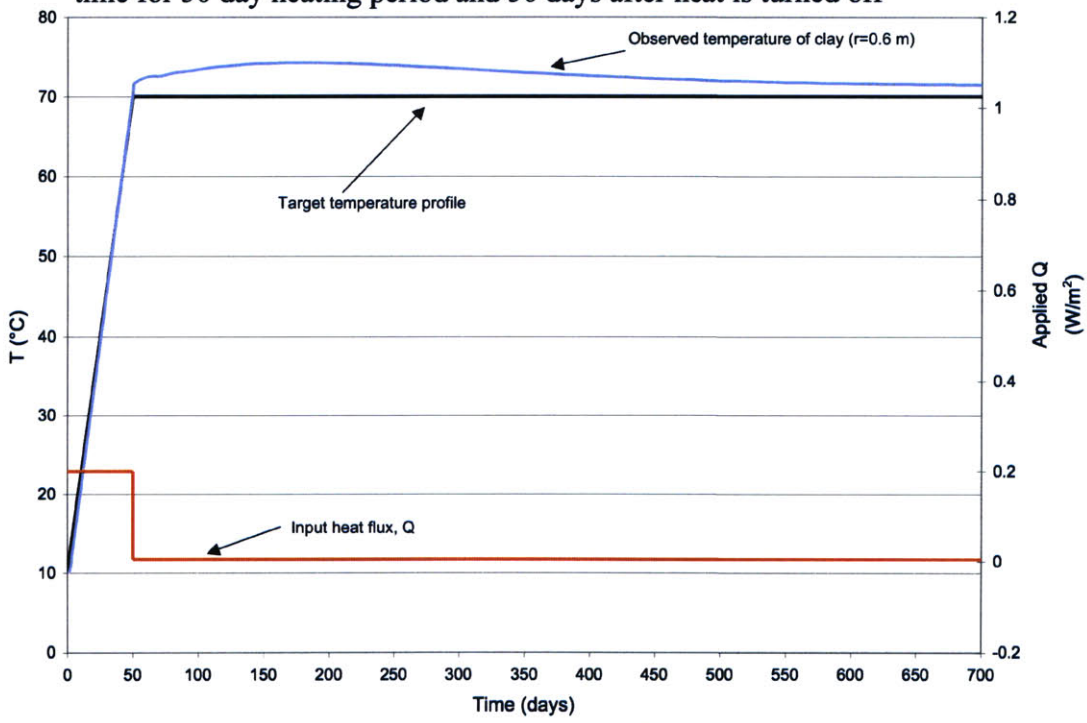


Figure 5.15:Case 2 ramped temperature: Heat input and corresponding temperature with time at surface midway between heat exchange pipes

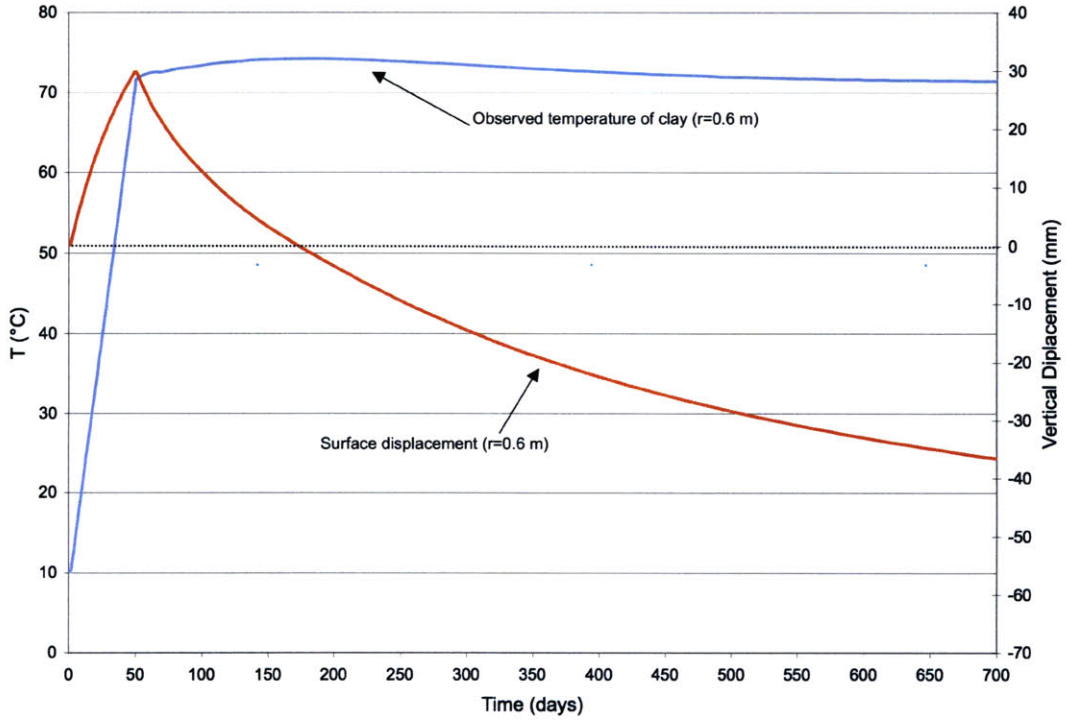


Figure 5.16: Case 2 ramped temperature: Temperature and surface displacement with time at point midway between heat pipes

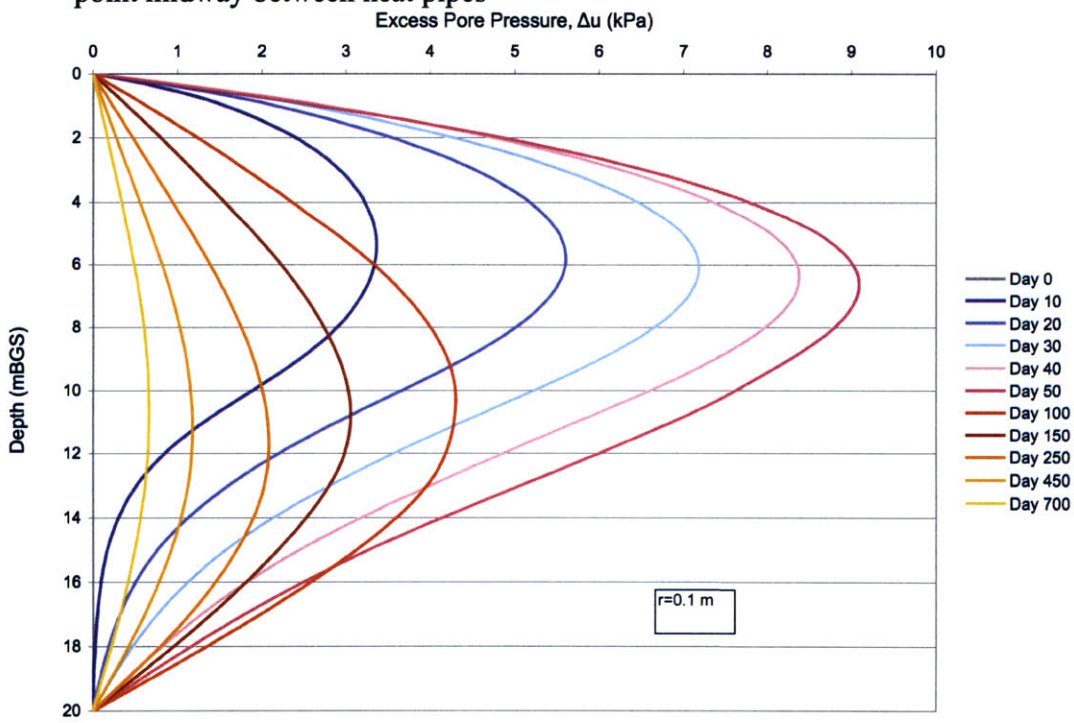


Figure 5.17: Case 2 ramped temperature: Induced excess pore pressure with time along depth of model

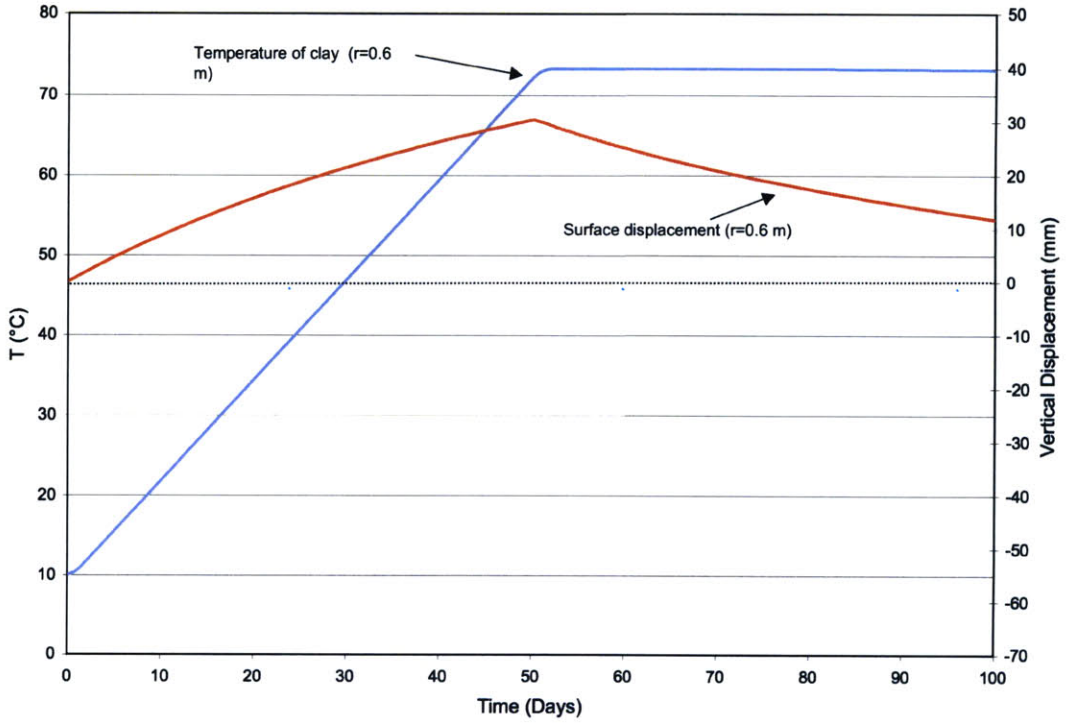


Figure 5.18: Case 2: temperature and displacement with time with heat input reduced to zero after 50 days midway between heat pipes

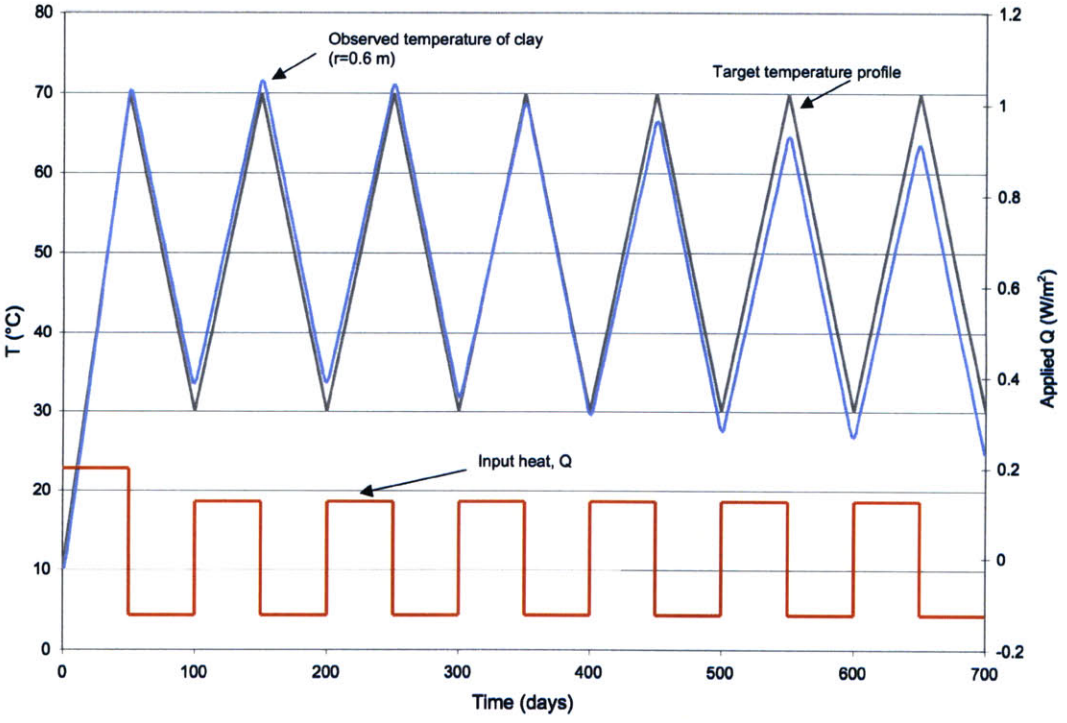


Figure 5.19: Case 2 fluctuating temperature: heat input and corresponding temperature with time at point midway between heat pipes

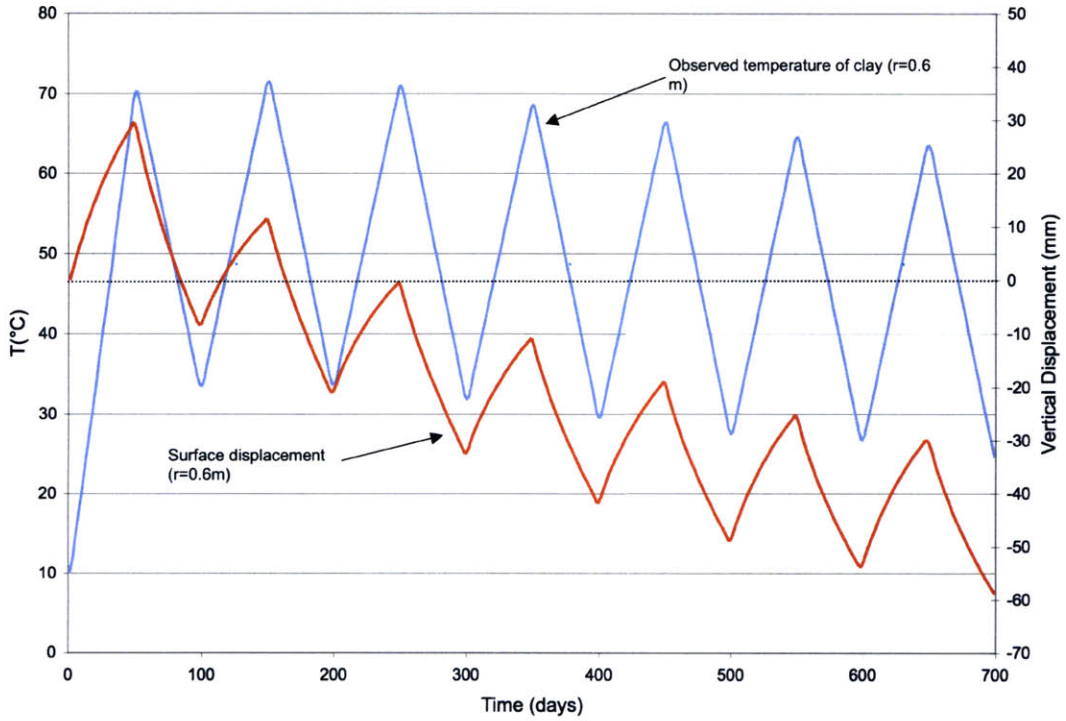


Figure 5.20: Case 2 fluctuating temperature: temperature and displacement with time at midpoint between heat pipes

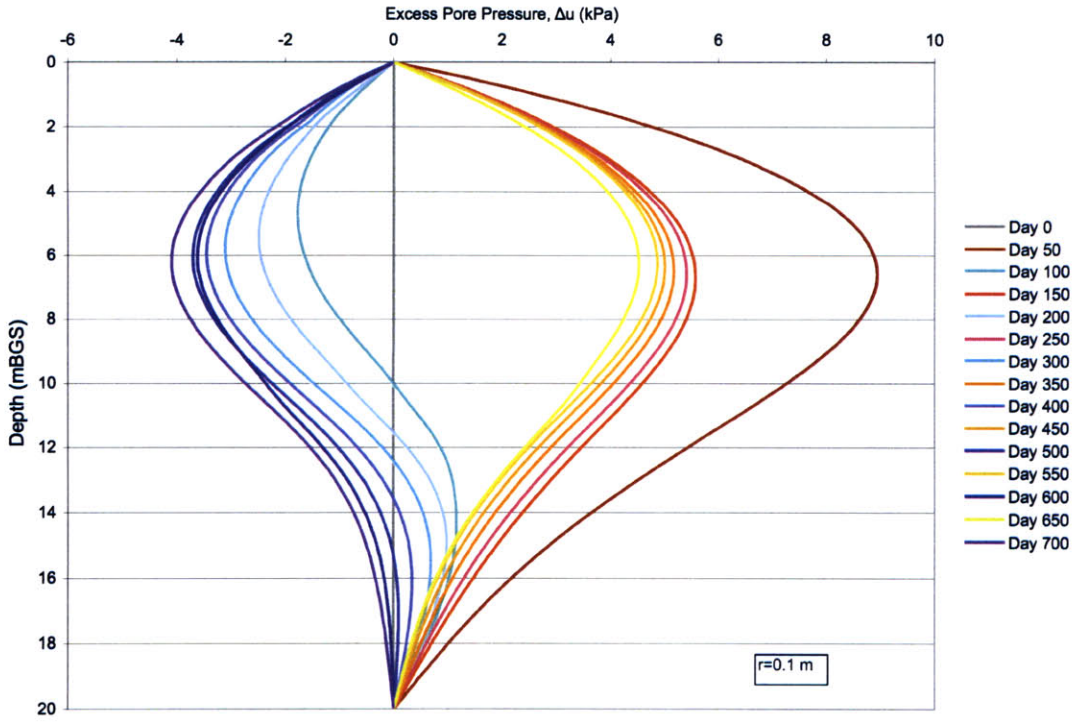


Figure 5.21:Case 2 fluctuating temperature: excess pore pressure at the end of each heating and each cooling cycle along the depth of clay

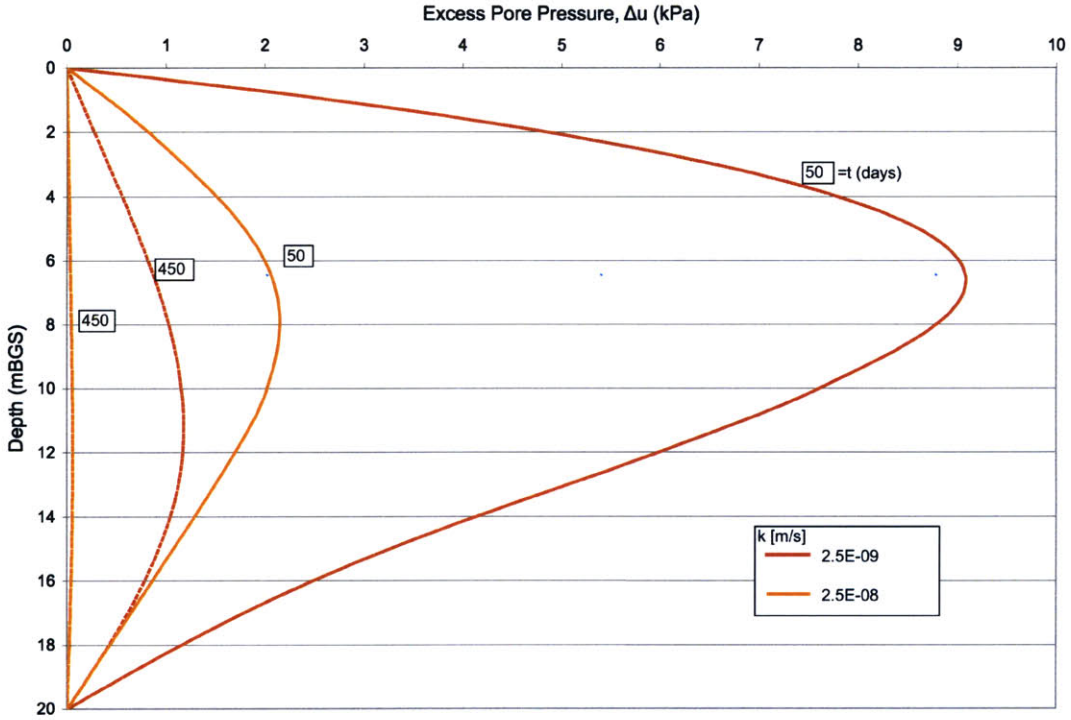


Figure 5.22: The effect of changes in hydraulic conductivity on excess pore pressure along the depth of clay layer

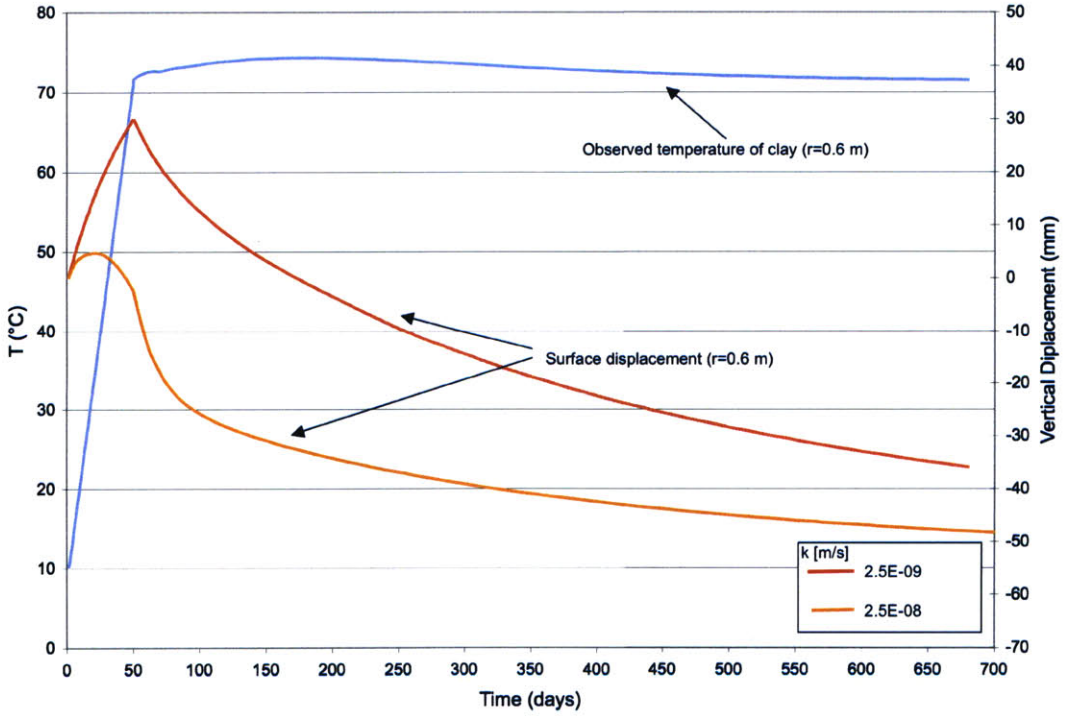


Figure 5.23: The effect of changes in hydraulic conductivity on surface settlement midway between heat pipes

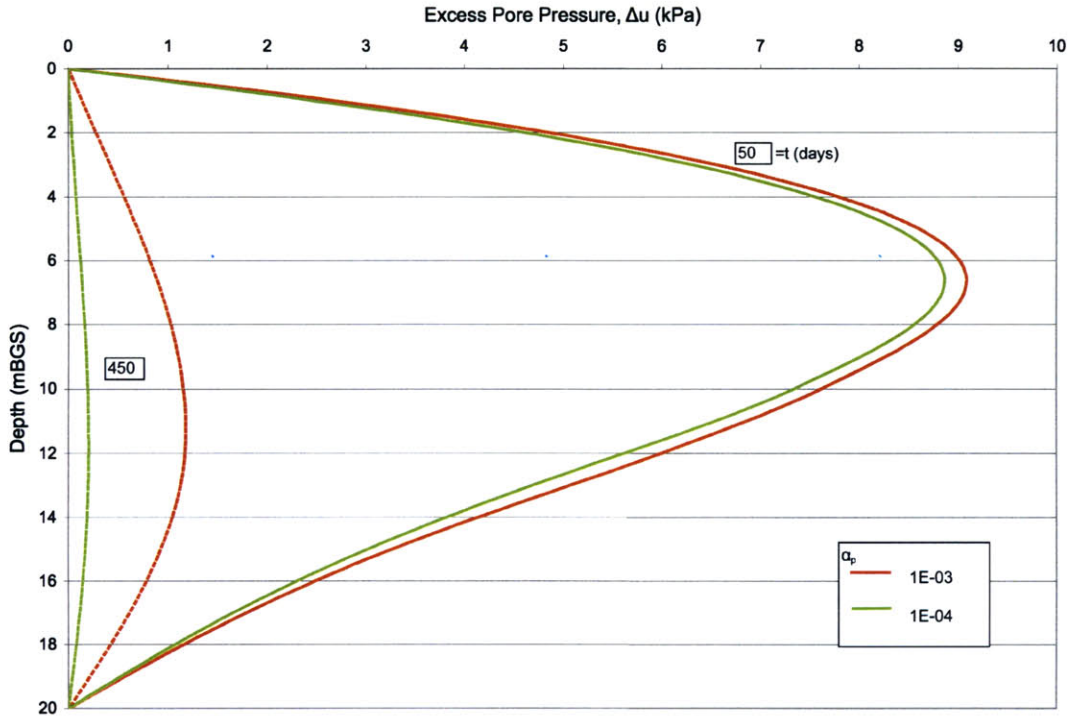


Figure 5.24: Effect of a change in $\alpha_p$ on $\Delta u$ along the depth of clay layer

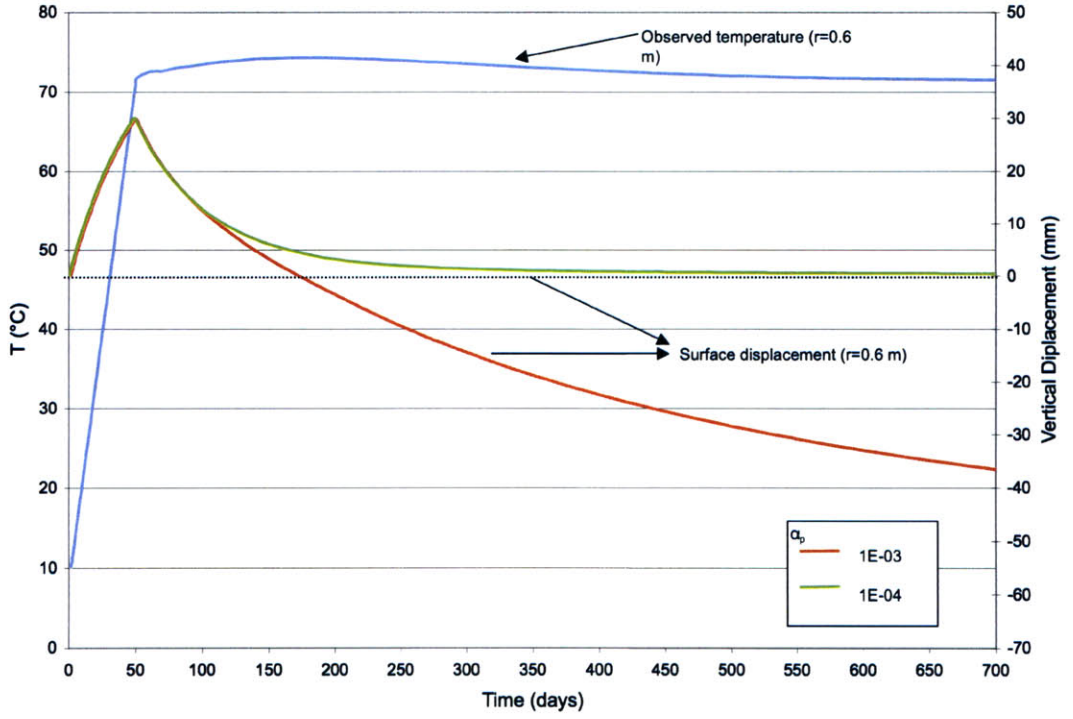


Figure 5.25: Effect of changes in $\alpha_p$ on displacement midway between heat pipes

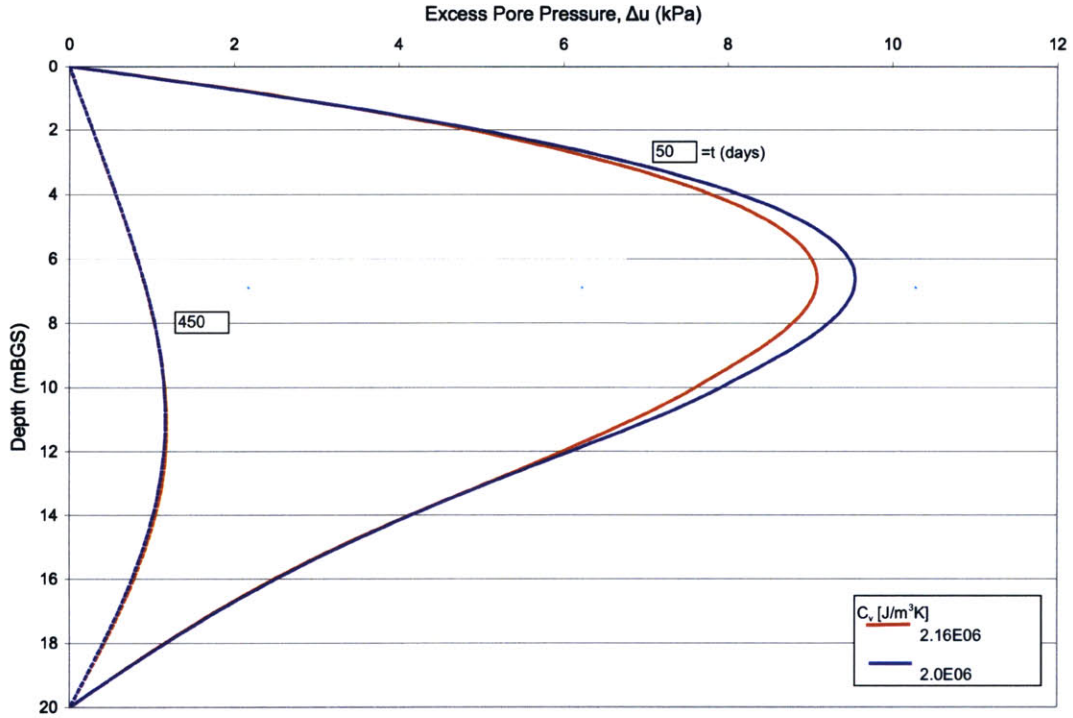


Figure 5.26: The effect of a change in $C_v$ on the observed Δu along the depth of clay layer

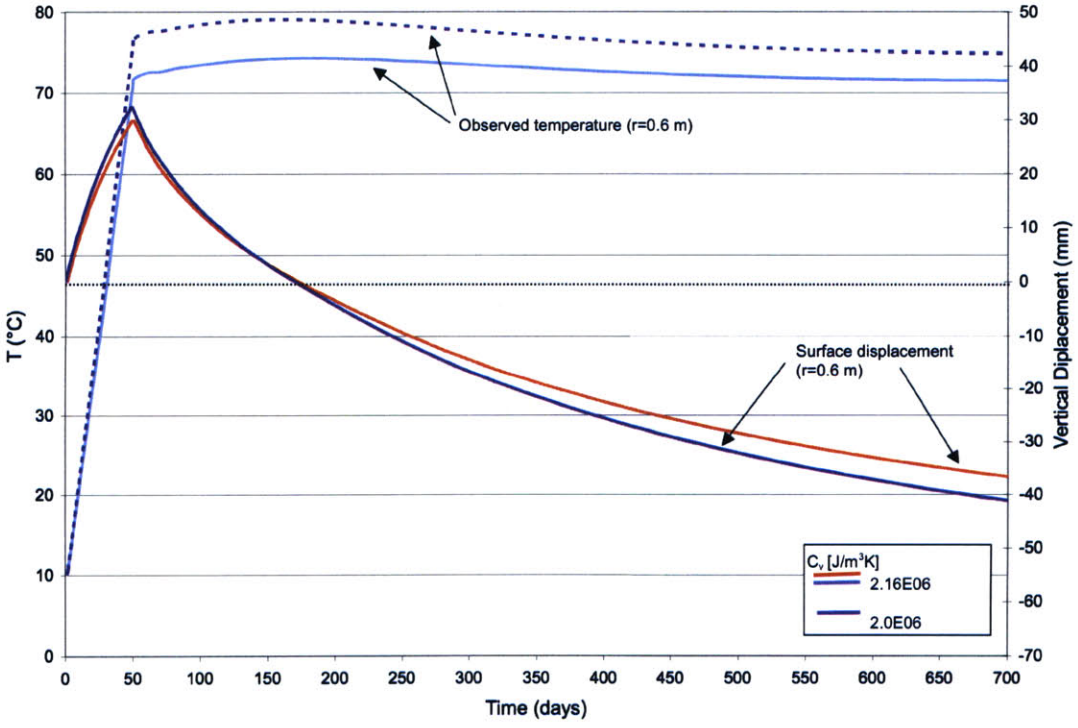


Figure 5.27: The effect of a change in volumetric heat capacity on the temperature and displacement response midway between heat pipes

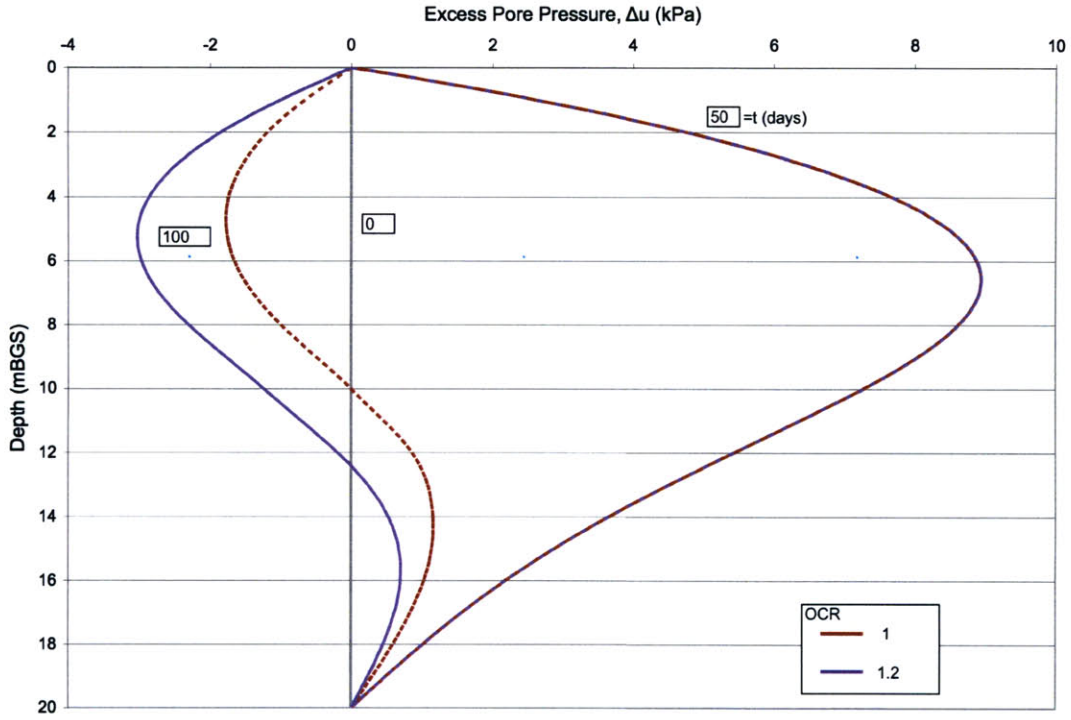


Figure 5.28: Effect of OCR on Δu along the depth of clay layer

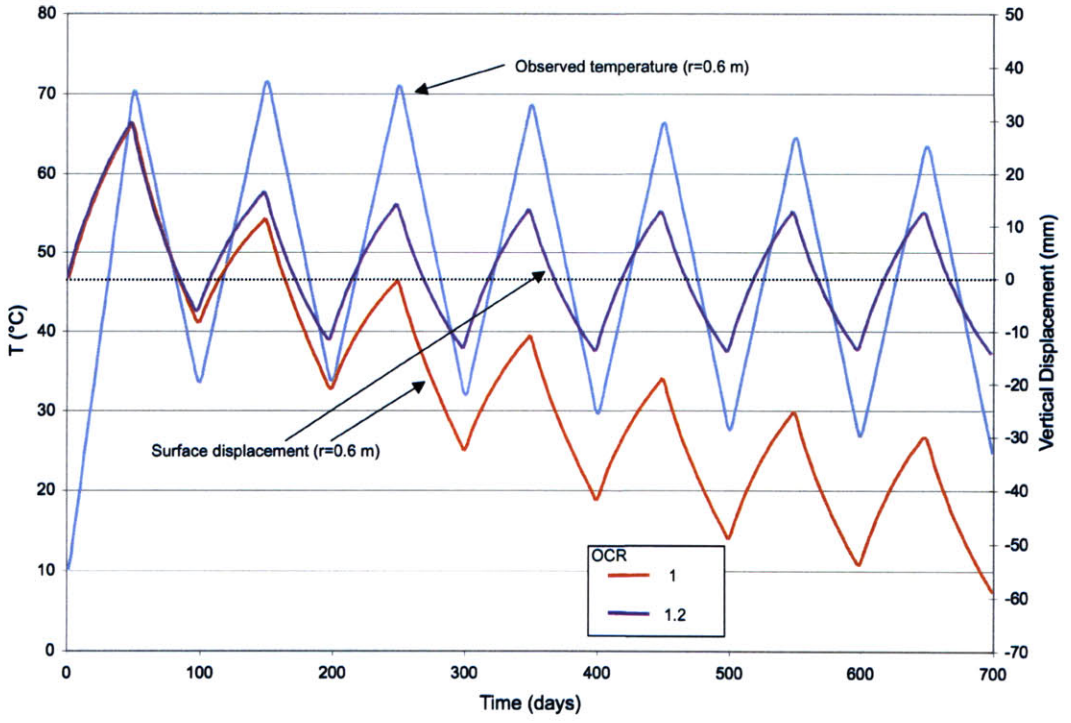


Figure 5.29: Effect of change in OCR on displacement behavior midway between heat pipes

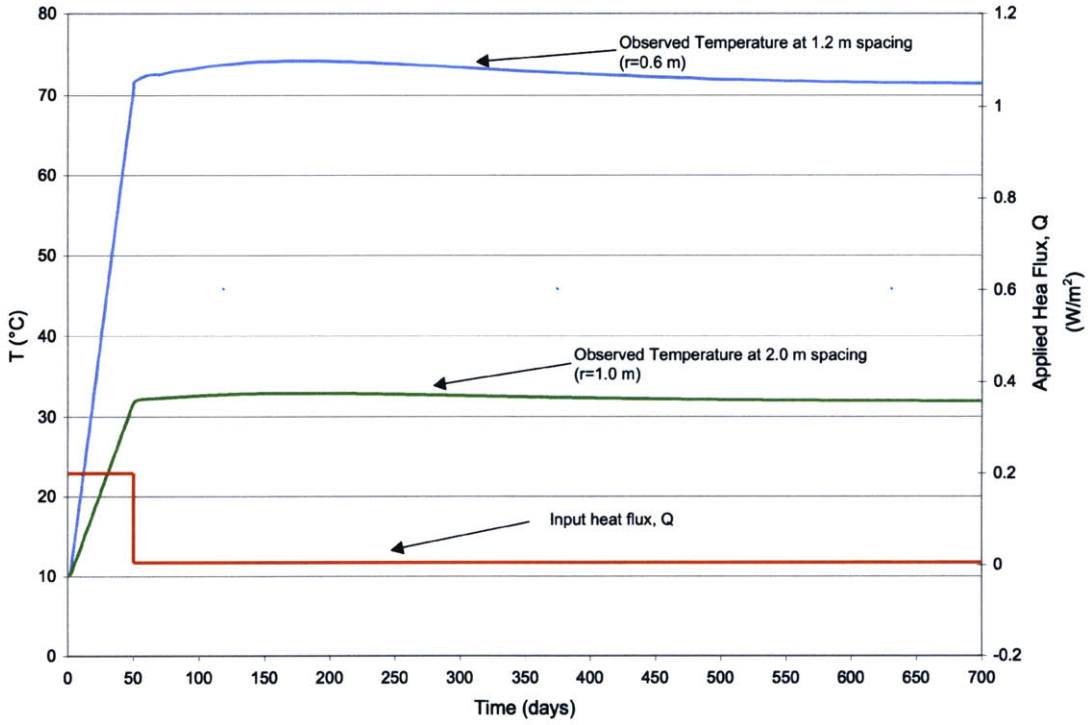


Figure 5.30: Input heat flux, Q, and measured ground temperature at midpoint between the heat pipes for 1.2 and 2 m spacing

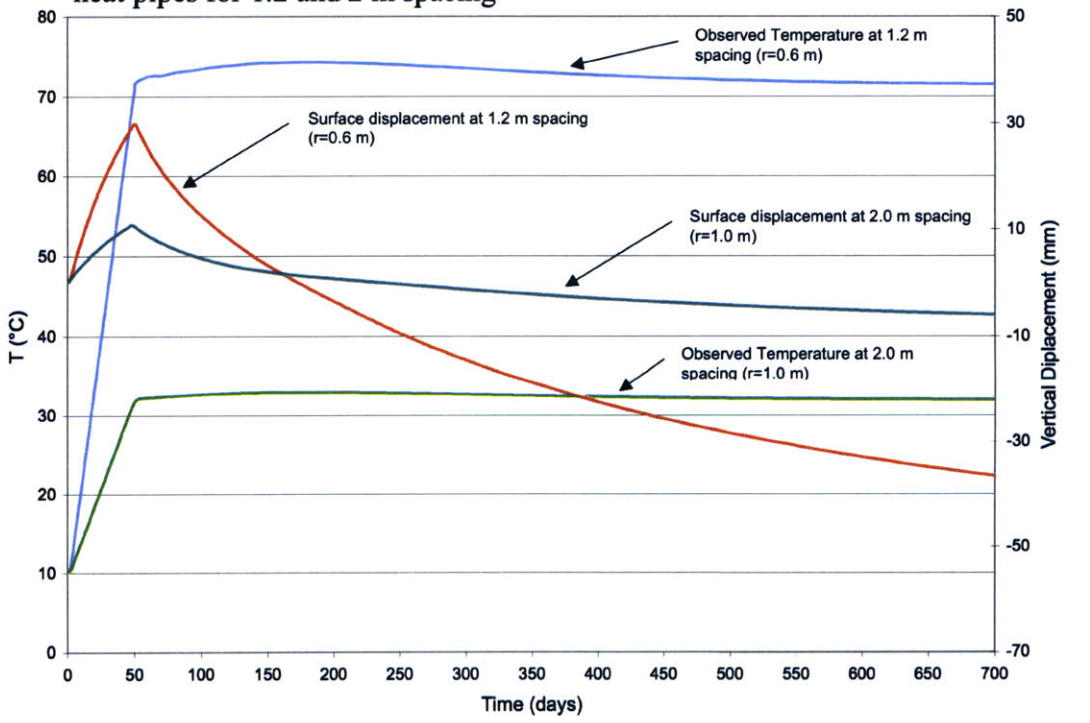


Figure 5.31: Effect of change in spacing on temperature and deformation response at the midpoint between heat pipes

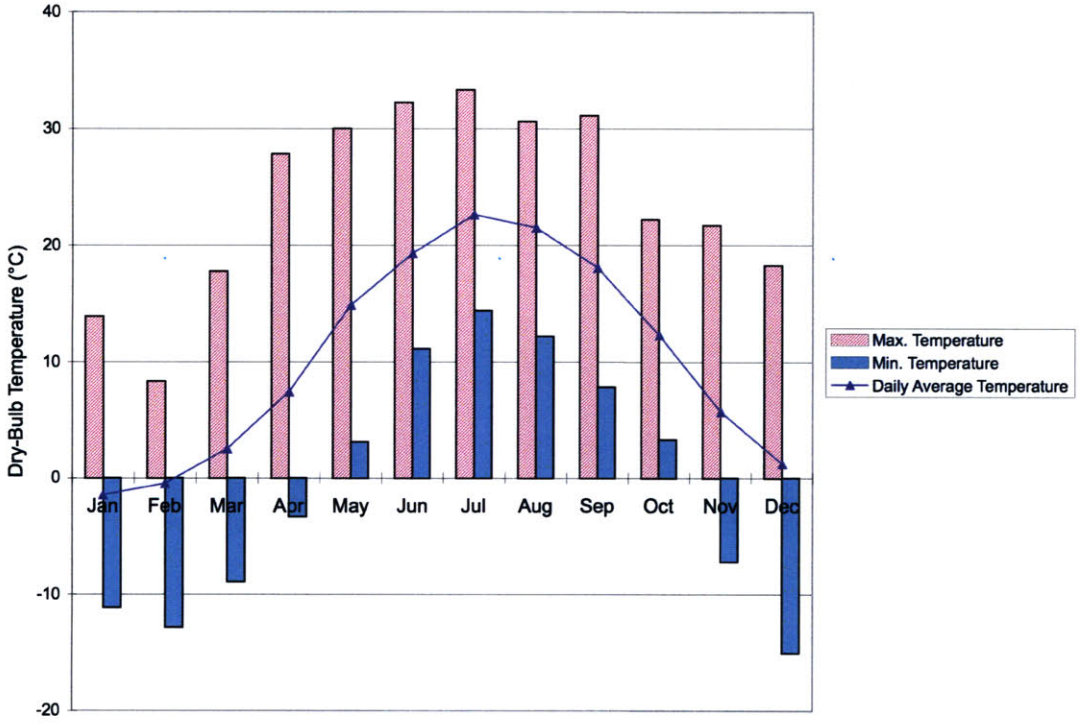


Figure 5.32: Monthly outdoor temperatures for Boston, MA (U.S. Department of Energy, 2009)

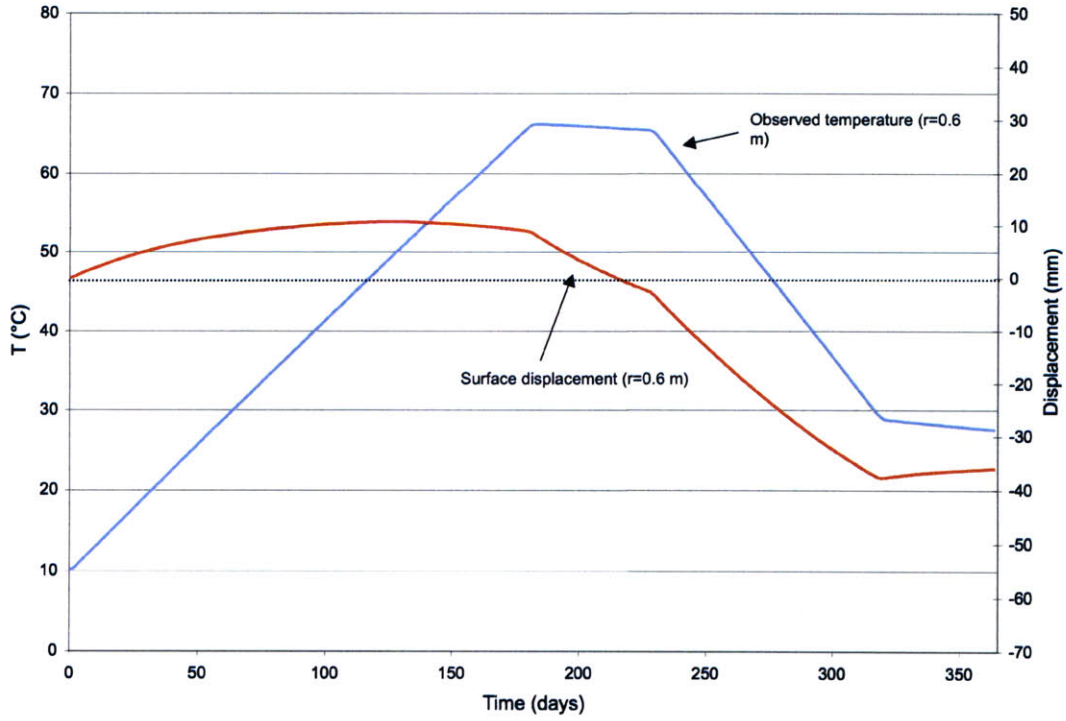


Figure 5.33: Temperature and displacement of simulated one year real operation

# 6 SUMMARY, CONCLUSIONS AND RECCOMENDATIONS

## 6.1 Summary

Ground energy storage systems present an underutilized opportunity for increasing the energy efficiency of buildings. However, their necessitates evaluation of the impact of changing ground temperature on the ground and any surrounding structures. If the ground is clay, thermal loads can lead to significant changes in the strength and deformation behavior of the clay.

Chapter 2 provided an introduction to the thermal environment of the ground, estimating thermal ground properties and different kinds of ground sourced heat storage systems. Chapter 3 provided a detailed look at the effect of temperature changes on the behavior of soft clay and computer models that endeavor to predict the thermo-poro-mechanical behavior of clay by expanding on the MCC model. In Chapter 4, the Picard (1994) model was selected for modeling in this thesis and a validation of the model to understand its capabilities and limitation was performed. Chapter 5 used the Picard (1994) model to perform a parametric study on the response of an idealized clay heat field to the thermal loading associated with seasonal heat storage.

## 6.2 Conclusions

The yield surface of soft clay contracts with increasing temperature. This leads to increased consolidation at higher temperatures and the associated risk of thermally unstable ground conditions. Normally consolidated clays are particularly susceptible to thermally induced consolidation. A change in temperature shifts the virgin consolidation and critical state lines of a soil. An increase in temperature shifts both line to the left in

void ratio, e-lnp' space, resulting in a lower apparent preconsolidation pressure and smaller $s_u$ at failure.

The Picard (1994) model on the CESAR-LCPC is available to simulate thermo-mechanical consolidation. While subject to the standard limitations of the MCC model, the Picard (1994) model can satisfactorily predict thermal hardening of soft clay and the resulting changes in deformation and strength behavior. The strength of the model lies in its commercial availability and its relatively simple user interface. However, the model suffers from never having been fully integrated onto the LCPC platform and remains in Beta form.

Chapter 4 illustrates the accuracy of the Picard (1994) model through comparison to SRLA Clay. The model accurately predicted deformation and yielding according to the MCC formulations under both drained and undrained condition. It was possible to satisfactorily simulate thermal yield hardening in the clay as well as the effects of cyclic thermal loading.

In Chapter 5, the Picard (1994) model was used to simulate a ground heat storage field. From the simulations, it is clear that the thermal loading applied to the ground by one heat pipe results in negligible changes to in-situ stress, pore pressure and settlement. The heat applied to the ground by the heat pipe is radiated over a very large soil mass and therefore does not lead to a local build up in temperature. This is parallel to the common situation of a ground source heat system built for a personal home or small building. This is an encouraging result; the current industry standard does not call for the evaluation of thermal load for small community based ground sourced heat storage systems. If there were potential for large changes of in-situ stress or settlement behavior, this practice would be inherently dangerous. On the other hand, since the heat exhausted to the ground disperses it is not possible to store that heat for use, making seasonal heat storage impractical. A small ground sourced heat system can still provide both heating a cooling by using the large thermal mass and inertia of the ground; a small amount of input or withdrawn heat will have negligible effects on a large soil mass.

Conversely, in a heat field with many closely spaced heat pipes, it was possible to store excess heat rejected to the ground and extract it later for use. The many closely spaced heat pipes limited the opportunity fir the heat to disperse. The closer the pipes, the less heat that could be input per °C change in temperature. At the same time, the more closely spaced the heat pipes, the less heat was lost to the boundary. The ability to store heat was coupled with the generation of significant excess pore pressure and associated consolidation. The induced consolidation ranges from 3 to 6 cm over 700 days, depending on the properties used and heating program followed. It is important to note that, except for the OCR test in Chapter 5, all of the simulations were run on normally consolidated clay. In-situ, even very soft soils are usually at least slightly overconsolidated. In section 5.6.4, changing the OCR from 1 to 1.2 led to a reduction in vertical displacement of 4.5 out of 6 cm. Even while investigating a normally consolidated, very sensitive soil, the amount of settlement due to changes in temperature was relatively small. A 6 cm consolidation over the 10 m deep heated clay corresponds to a 0.6% strain through the layer.

## 6.3 Recommendations

This thesis solely investigated the effect of thermal loading. Traditionally, ground source heat storage systems have been installed in locations removed from the built environment. Efficient use of space and materials calls for the ability to install ground source heat systems underneath buildings and structures. The exciting new foundation technique, Energy Foundations, would combine ground source heat storage systems into the concrete foundation elements of the structure itself. In such a system, the ground would be simultaneously mechanically and thermally loaded. For energy foundations, accurate understanding of thermal hardening is very important. Ignoring the thermal effects can lead to significant miscalculation of settlement and an overestimation of in situ strength.

In order to more fully understand thermal loading of soft clays it will be important to investigate the interaction of simultaneous thermal and mechanical loading. This can be done in three ways:

1) Modeling of a energy pile in soft clay subject to thermal and mechanical loads,
2) Lab experiments on thermally and mechanically loaded soft clays to evaluate the accuracy of the model predictions, and
3) Monitoring of a full-scale energy pile in soft clay.

A debugging of the Picard (1994) Model should precede any further large undertaking of simulations. This could be done in cooperation with CESAR. Alternatively, the Picard (1994) thermal hardening equation could be incorporated into the MCC model and integrated within another FE code (such as ABAQUS of PLAXIS).

Future work with this concept could concentrate on an understanding of applied thermal loads. This thesis dealt with ground energy storage isolated from the structures benefiting from the heat exchange. A thorough investigation of the thermal loads applied to the ground by a sample structure would enhance the understanding of the length and intensity of thermal cycles experienced by the soil due to a ground energy storage system.

# 7 REFERENCES


Adam, D. and Markiewicz, R. (2009), "Energy from earth-couple structures, foundations, tunnels, and sewers," *Géotechnique*, 59(3), 229-236.

Andersland, O. B., and Ladanyi, B. (2004), 'Frozen ground engineering,' Edition 2, John Wiley and Sons, 2003.

Akagi, H. and Komiya, K. (1995), "Constant rate of strain consolidation properties of clayey soil at high temperature," *Compression and Consolidation of Clayey Soils*, Rotterdam, 3-8

Arnorsson, S. (2004), "Environmental Impact of Geothermal Energy Utilization," Geological Society Special Publication, Washington, DC, 236, 297-336

Baldi, G., Hueckel T, Peano, A and Pellegrini, R. (1991), "Developments in modeling of thermo-hydro-mechanical behaviour of Boom Clay and clay-based buffer materials," Vols 1 and 2; EUR 13365/1 and 13365/2. Luxembourg. Commission of the European Communities.

Boudali, M, Leroueil, S. and Srinivasa Murthy, B.R. (1994), Viscous behaviour of natural clays, *Proc. XIII ICSMFE*, New Dehli, pp. 411-416.

Bourgeois, E. (2008), Personal correspondence.

Brandl, H. (2006), "Energy foundations and other thermo-active ground structures," *Géotechnique*, 56 (2), 81-12

Britto, A.M., Savidou, C., Gunn, M.J., and Brooker, J.R. (1992), "Finite element analysis of the coupled heat flow and consolidation around hot buried objects," *Soils and Foundations*, 32(1), 13-25.

Campanella, R.G. and Mitchell, J.K. (1968), "Influence of temperature variations on soil behavior", *ASCE Journal of the Soil Mechanics and Foundations Division*, 709-734.

Cekerevac, C. and Laloui, L. (2003), "Experimental study of thermal effects on the mechanical behaviour of a clay," *International Journal for Numerical and Analytical Methods in Geomechanics*, 28, 209-228.

Clauser, C. (2006), *"Ch.8 Geothermal Energy". From: Renewable Energy. Landolt-Börnstein - Group VIII Advanced Materials and Technologies.* Springer Berlin Heidelberg. http://www.springerlink.com/content/mq115u7nl9100295/, Last Accessed: 15-March-2009.

U.S. Department of Energy (2009). *Building Technologies Program Weather Data*, http://apps1.eere.energy.gov/buildings/energyplus/cfm/Weather_data.cfm, last accessed 8-July-2009.

Ennigkeit, A. and Katzenbach, R. (2000) "The double use of piles as foundation and heat exchanging elements," *Proceedings XV ICSMGE*, 2, 893-896.

Eriksson, L. G. (1989) "Temperature effects on consolidation properties of sulphide clays," *Proc. 12th ICSMFE*, Rio de Janeiro,3, 2087-2090.

Esch, D.C. (2004), "Thermal Analysis, Construction, and Monitoring Methods for Frozen Ground," *ASCE Technical Council on Cold Regions Engineering*, Reston, Virginia.

Farouki, O. T. (1986), *Thermal Properties of Soils, Series on Rock and Soil Mechanics Vol. 2*. Trans Tech Publications, Germany.

François, B., Laloui, L. and Laurent, C. (2009), "Thermo-hydro-mechanical simulation of ATLAS in situ large scale test in Boom Clay", *Computers and Geotechnics*, 36, 626-640.

Florides, G. and Kalogirou, S. (2007), "Ground heat exchangers - A review of systems, models and applications," *Renewable Energy*, 32, 2461-2478.

Gabrielsson, A., Bergsahl, U, and Moritz, L. (2000), "Thermal energy storage in soils at temperatures reaching 90°C," *Journal of Solar Engineering*, 122, 3-8.

Graham, J., Tanaka, N., Crilly, T. and Alfaro, M. (2001), "Modified Cam-Clay modeling of temperature effects in clays," *Canadian Geotechnical Journal*, 38, 608-621.

Harris, J.S. (1995), *Ground freezing in practice*, New York, ASCE.

He, M. M. and Lam, H. N. (2005), "Study of Geothermal Seasonal Cooling Storage System with Energy Piles," Mechanical Engineering Department, University of Hong Kong,http://intraweb.stockton.edu/eyos/energy_studies/content/docs/FINAL_PAPERS/11A-2.pdf, Last Accessed 10-July-2009.

Holdsworth, B. (2006), "Keeping cool with concrete," *Concrete Engineering International*, Winter, 32-33.

Hueckel, T. and Baldi, G. (1990), "Thermoplasticity of Saturated Clays: Experimental Constitutive Study," *ASCE Journal of Geotechnical Engineering*, 116(12), 1178-1796.

Hueckel, T. and Borsetto, M. (1990), "Thermoplasticity of Saturated Soils and Shales: Constitutive equations," *ASCE Journal of Geotechnical Engineering*, 116, (12), 1765-1777.

Hueckel, T., Francois, B. and Laloui, L. (2009), "Explaining thermal failure in saturated clays", *Géotechnique*, 59(3), 197-212.

Hueckel, T., Pellegrini, R. and Del Olmo, C. (1998), "A constitutive study of thermo-elasto-plasticity of deep carbonatic clays," *International Journal for Numerical and Analytical Methods in Geomechanics*, 22, 549 – 574.

Hughes, P. J. (2008), "Geothermal (Ground-Source) heat pumps: market status, barriers to adoption, and actions to overcome barriers," *EERE Geothermal Technologies Program*, Energy and Transportation Science Division, U.S. Department of Energy, ORNL/TM-2008/232.

Johansen, O. (1975), "Thermal conductivity of soils," Ph.D. Thesis. Norwegian University of Science and Technology, Trondheim.

Kuntiwaittanakul, P., Towhata, I., Ohishi, K. (1995), "Temperature effects on undrained shear characteristics of clay," *Soils and Foundations*, 35(1), 147-162.

Laloui, L. and Cekerevac, C. (2003), "Thermo-Plasticity of clays: An isotropic yield mechanism," *Computers and Geotechnics*, 30, 649-660.

Laloui, L., Nuth, M. and Vulliet, L. (2006), "Experimental and numerical investigation of the behaviour of a heat exchanger pile," *International Journal for Numerical and Analytical Methods in Geomechanics*, 30, 763-781.

Laloui, L., Leroueil, S. and Chalindar, S. (2008), "Modelling the combined effect of strain rate and temperature on one-dimensional compression of soils," *Canadian Geotechnical Journal*, 45, 1765-1777.

Laloui, L. and Nuth, M. (2007), "Numerical modeling of some features of heat exchanger pile," *ASCE Geotechnical Special Publication; Foundation analysis and design-innovative methods*, 189-194.

Leroueil, S. and Marques, M. E. S. (1996)," Importance of strain rate and temperature effects in Geotechnical Engineering," *ASCE Measuring and Modeling Soil Behavior (GSP 61),* 1-60.

Leroueil, S. (1996), "Compressibilty of Clays : Fundamental and Practical Aspects," *ASCE Journal of Geotechnical Engineering*, 122(7), 534- 543.

Marques, M.E.S., Leroueil, S. and Almeida, M.S.S. (2004) "Viscous behavior of St-Roch-De-L'Achigan Clay, Quebec," *Canadian Geotechnical Journal*, 41, 25-38.

Moritz, L. (1995), "Geotechnical Properties of Clay at Elevated Temperatures," Swedish Geotechnical Institute, Report SGI 47.

Moritz, L. (1997), "Heat Storage in soft clay field tests with heating (70°C) and freezing of the soil," Swedish Geotechnical Institute, Report SGI 53.

Moriwaki, T., Yoshikuni, H., Nagai, O. and Nago, M. (1995), "Cyclic Consolidation characteristics of clay reconsolidated at high," *Compression and Consolidation of Clayey Soils*, Rotterdam, 135-142.

Oberhauser, A., Adam, D., Kopf, F., Markiewicz, R., and Ostermann, N. (2004), "Utilization of geothermal energy in railway tunnels," Department of Railway Engineering, Traffic Economics and Ropeways, Vienna University of Technology, Austria.

Phetteplace, G. (2007), "Geothermal Heat Pumps," *ASCE Journal of Energy Engineering*, 133(1), 32-38.

Picard, J. M. (1994), " Écrouissage Thermique des argiles saturées: Application au stockage de dechets radioactifs," These de Doctorat de l'École National de Ponts et Chausées.

Preene, M and Powrie, W. (2009) "Ground energy systems: from analysis to geotechnical design," *Géotechnique*, 59(3), 261-271.

Robinet, J.C., Rahbaoui, A., Plas, F. and Lebon, P. (1996), "A constitutive thermomechanical model for saturated clays," *Engineering Geology*, 41, 145-169.

Roscoe m K. H. and Burland, J.B. (1968), "On the generalized stress-strain behaviour of wet clay", In *Engineering Plasticity*, eds. J. Heyman and F.A. Leckie, 535-609. Cambridge, England: Cambridge University Press.

Sailor, D. J., Hutchinson, D. and Bokovoy, L. (2008), "Thermal property measurement for ecoroof soils common in the western U.S," *Energy and Buildings*, 40, 1246-1251.

Seneviratne, H. N. (1993), "A review of models for predicting the thermomechanical behaviour of soft clays," I*nternational Journal for Numerical and Analytical Methods in Geomechanics*,17, 715-733.

Towhata, I., Kuntiwattanaku, P., Seko, I, and Ohishi, K. (1993), "Volume change of clays induced by heating as observed in consolidation tests," *Soils and Foundations*, 33(4), 170-183.

Unterberger, W., Hofinger, H., Grünstäudl, T. Adam, D. and Markiewicz, R. (2004), "Utilization of tunnels as sources of ground heat and cooling - Practical applications in Austria," *Proc. of the ISRM International Symposium 3rd ARMS*, Rotterdam, 421-427.

Unterberger, W., Hofinger, H., Markiewicz, R. and Adam, D. (2005)" Running hot and cold in Vienna," *Tunnels and Tunneling International*, 37, (2), 36-39.

Hoare, R. (2005), WorldClimate, http://www.worldclimate.com/. Last Accessed: 14-March, 2008.

Yashima, A., Leroueil, S., Oka, F. and Guntoro, I. (1998), "Modelling Temperature and strain dependent behavior of clays," *Soils and Foundations*, 38(2), 63-73.

# APPENDIX A: Picard (1994) on CESAR-LCPC Tutorial

Performing an consolidated-undrained shear simulation on SRLA Clay:

## A.1 Drawing the sample

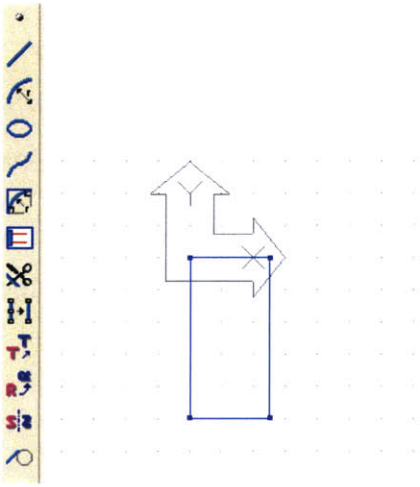

Use the drawing tools at the left hand side of the screen to draw a 0.5 m x 1 m box. Since the model will be run in axisymmetric space this corresponds to a 1 m tall cylinder with a radius-0.5 m.

Go to the density tab  on the top left to choose node spacing. Choose 5 nodes on each of the top and bottom and 10 on each side.

Click on  on the top left to go to the mesh tab. Select  from the left tool bar.

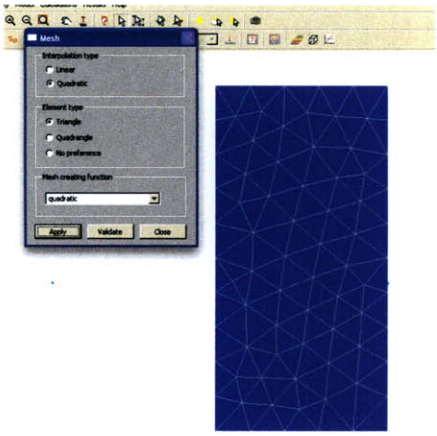


Select interpolation type: Quadratic, Element Type: Triangle and Mesh creating function, quadratic. Highlight the sample and click 'apply'. Use the "make groups" button to name the type of soil  . This is very important when working with multiple materials. In this case, there is only one soil that will be named "clay". Highlight the sample and click "apply" followed by validate and close.

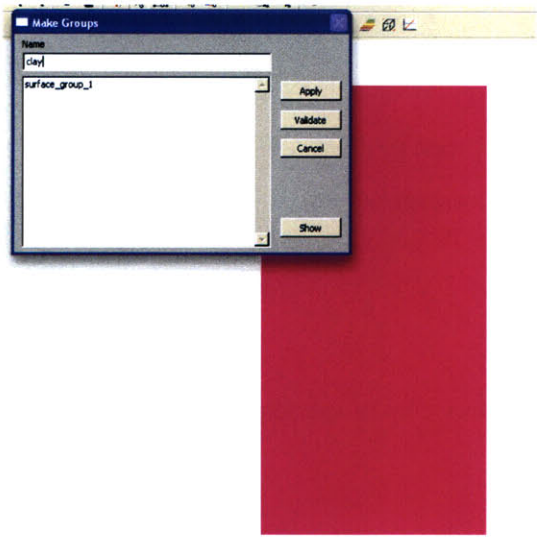

## A. 2 Inputting Initial Conditions

 Click to define the model. Give the simulation a name. In this case, the name is SRLA-U. Click 'Open'. The model type selection window comes up. Select "coupled problems", MPNL, Axisymmetrical. Click validate. From the next screen, choose "initialization of parameters".

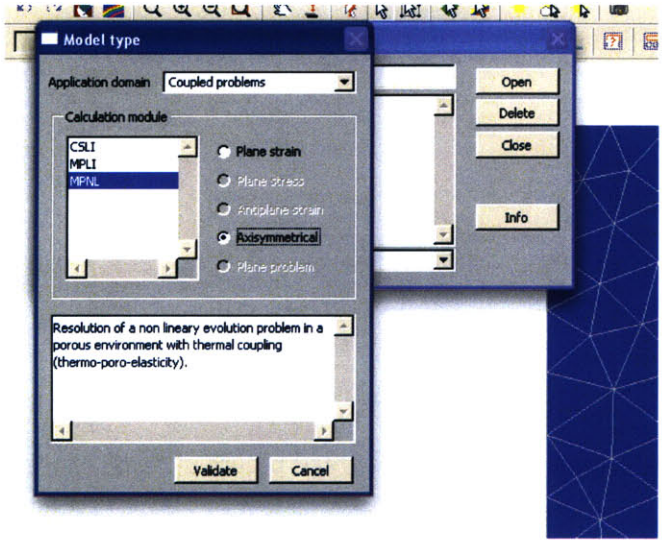


The next step is to assign properties to the clay. However, since the Picard model does not mount properly on the platform we will need to change this later. Click on  . Highlight the sample and apply any Mechanical, groundwater and thermal properties. Select all the properties before clicking on apply.

Click on  to apply the initial conditions. There are 4 options for applying initial conditions:

1) Initial displacement
2) Initial stress

3) Initial temperature
4) Initial excess pore pressure

In this case there is no initial displacement or excess pore pressure. An initial uniform stress and temperature are applied, ignoring the effects of gravity.

From the initial stress bar 

click on 

and apply 0 kPa initial stress. (In other simulations if applying stress larger than zero. Note that the sign convention is negative: to apply 100 kPa in situ stress type -100.)

From the initial temperature bar 

select 

and apply a uniform initial temperature of 50°C. Note: To apply anything the sample must be highlighted before clicking 'apply'. After applying the highlight will turn off, indicating that the property has been applied.

## A.3 Defining Boundary Conditions

 Click to define boundary conditions. Give the boundary conditions a name.

There are three types of boundaries to by applied, mechanical 

, thermal 

and water pressure, 

.

Select the left hand side of the model (representing the center line), click on  and apply a zero horizontal displacement condition.


Repeat on the bottom boundary and apply a zero vertical displacement condition.

Using the  button apply a 50°C boundary condition to all 4 boundaries.

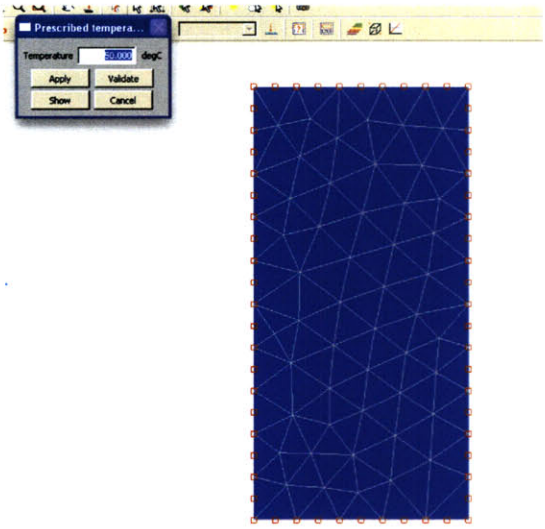


Using the $\overline{p}$ button apply 0 kPa excess pore pressure to the top and bottom boundaries.

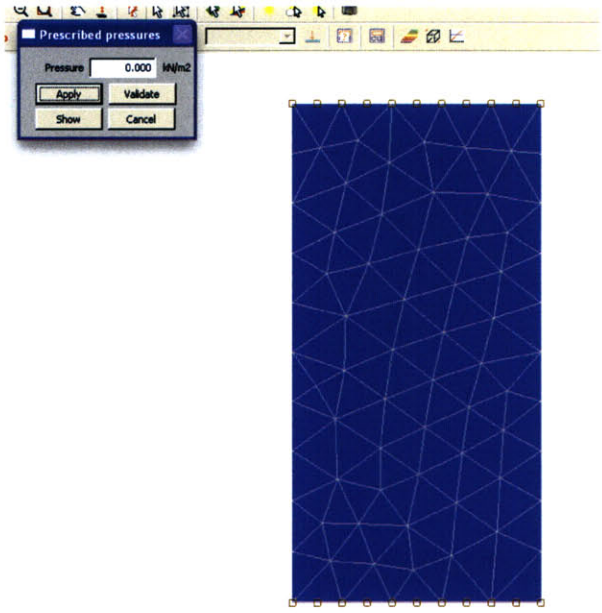

## A.4 Applying Loads (Consolidation)

 Click to open loads tab. Give the load a name.

Apply a uniform pressure of 112 kPa to the top boundary and the left boundary using  .

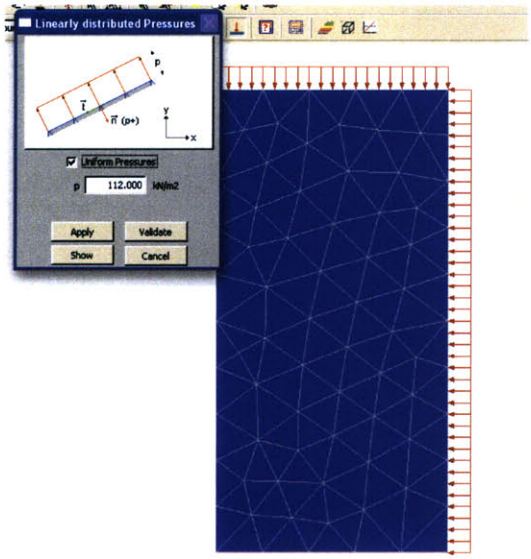


It is possible to apply more than one load at once by adding another load case. Using the  button. When applying thermal loads and mechanical loads simultaneously it is useful to separate them under different labels.

## A.5 Calculation Parameters

 Click, from the top toolbar. A window will open with a number of tabs. In this window it is possible to set the time steps, the load and boundary factors, the time for analysis, acceptable error and save data for restart.

Set 10 constant time steps starting at time 0 h, each 200 h long. (The goal is to consolidate the sample fully drained so the steps need to be long enough so that no excess pore pressure develops).

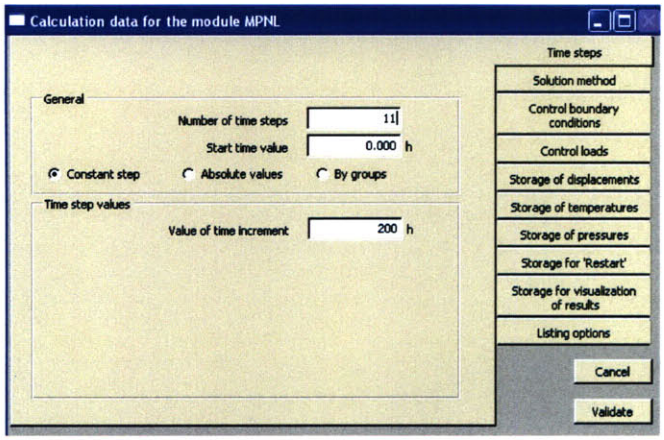


Set the max number of iteration to 5000 and the tolerance to 0.01.

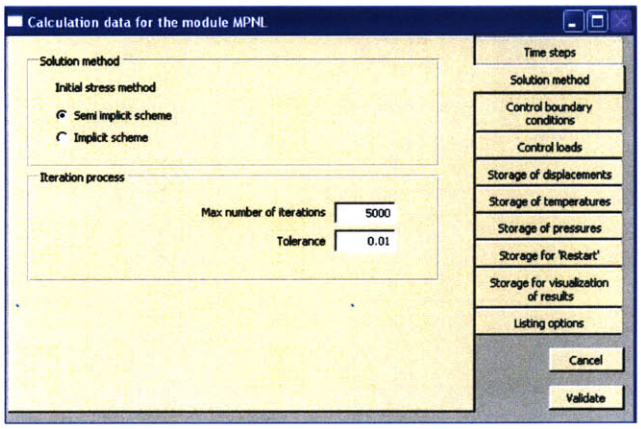


In the control loads tab change the load coefficient for each step to range from 0.0 in the first step to 1.0 in the last step, increasing in increments of 0.1.

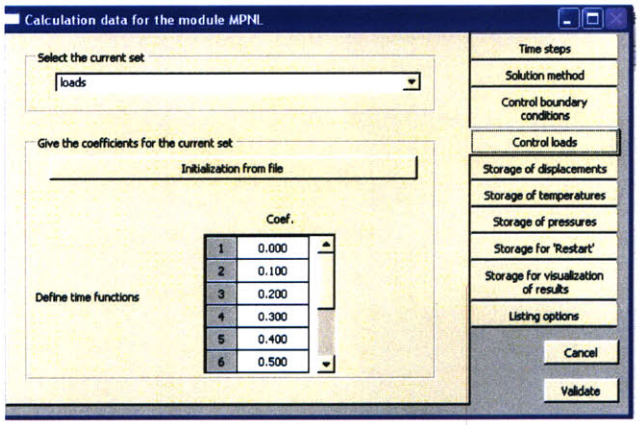


In the "Storage for restart tab" click the box and provide a name and location for the file. Keep the name short, too many characters and the program will not be able to locate it later. Make sure to type in the file type ".rst" as part of the file name.

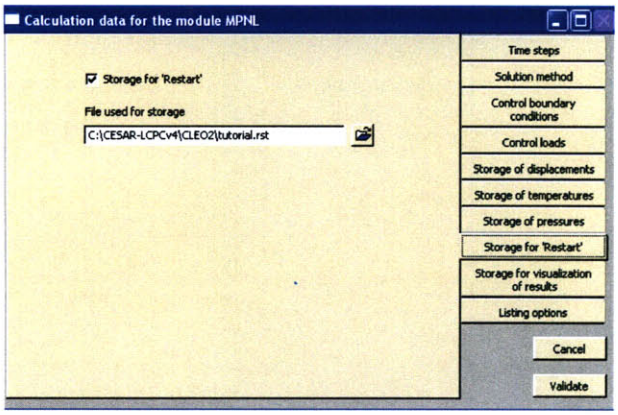


Select "Validate".

## A. 6 Performing Calculations

 Click, from the top toolbar. Highlight the simulation to be run, click on "create input files for the solver"

Click validate.

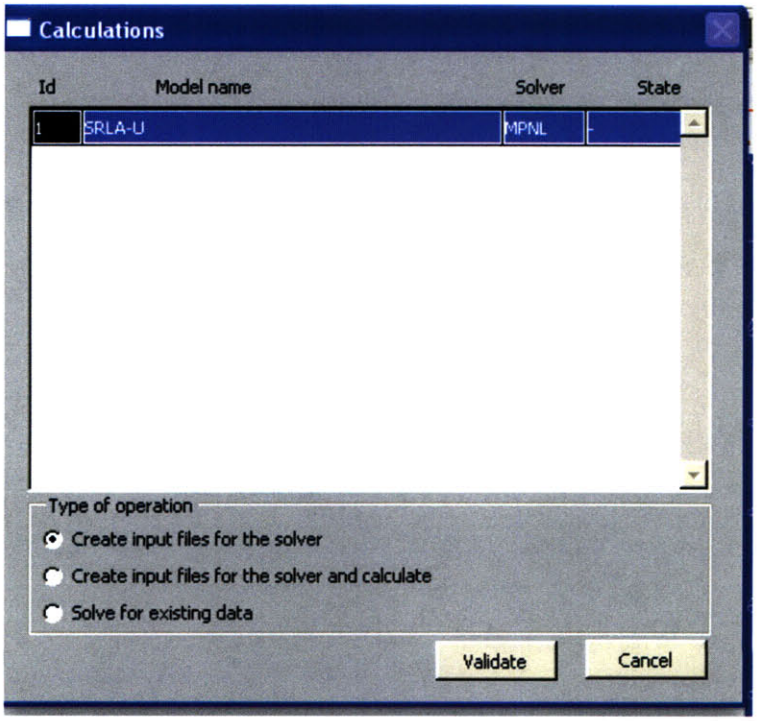

Go 'user tools/edit file .data'. This file lists the code for the run of this model. When working with Picard (1994) the soil properties need to be entered by manually.

Find the section of the code that lists the soil properties. It will be labeled with the name of the layer given in step 1, in this case "clay".

```
1  1  1  1  1  1  1  1  1  1
1  1  1  1
clay                                   A  9
1  2
0.00000e+000  0.00000e+000  0.00000e+000  0.00000e+000  0.00000e+000  0.00000e+000
0.00000e+000  0.00000e+000  0.00000e+000  0.00000e+000  0.00000e+000  0.00000e+000
0.00000e+000  0.00000e+000  0.00000e+000  0.00000e+000  0.00000e+000
COND
2
IMP
```

The fist number after clay lists the type of model. The number for the Picard (1994) model is 43. The second number determines between plane strain (1) and axisymmetric (2). The following rows of numbers list the material parameters.

The Picard (1994) model calls for 21 inputs in the following order.

1) Buoyant Density ($kN/m^3$)
2) Young's Modulus (Pa)
3) Poission's Ratio
4) Fluid Density ($kg/m^3$)
5) Porosity
6) Biot Modulus (Pa)
7) Permeability in x-direction ($m^4/kNs$)
8) Permeability in y-direction ($m^4/kNs$)
9) Permeability in xy-direction ($m^4/kNs$)
10) Biot coefficient
11) Volumetric Heat Coefficient ($J/m^3K$)
12) Thermal conductivity in x-direction ($W/m^3K$)
13) Thermal conductivity in y-direction ($W/m^3K$)
14) Thermal conductivity in xy-direction ($W/m^3K$)
15) Thermo-Elastic compressibility coefficient ($K^{-1}$)
16) Thermal expansion coefficient ($K^{-1}$)
17) Slope of the critical state line
18) Preconsolidation pressure at reference temperature (Pa)
19) Coefficient of thermal hardening ($K^{-1}$)
20) Skempton's Coefficient
21) Reference Temperature (°C)

```
1  1  1  1
clay
43   2
5.00000e+000  2.10000e+006  3.50000e-001  1.00000e+003  7.00000e-001  4.40000e+009
2.00000e-001  2.00000e-001  0.00000e+000  1.00000e+000  2.16000e+006  2.70000e+000
2.70000e+000  0.00000e+000  1.00000e-005  1.00000e-005  1.13000e+000  1.11000e+005
2.77000e+000  1.00000e-003  1.00000e+000  2.00000e+001
COND
```

(note: the permeability is artificially large in this simulation to force fully drained consolidation, since time is not an important issue here this is acceptable).

Save changes. Close the window.

Click on  . Select solve for "existing data" and validate. The program will perform the simulation. (Don't forget to save).

## A. 7 Viewing the results

The 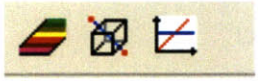 tools on the top left can be used to view the results.

For example, the vertical displacement after increment 11 is shown below.

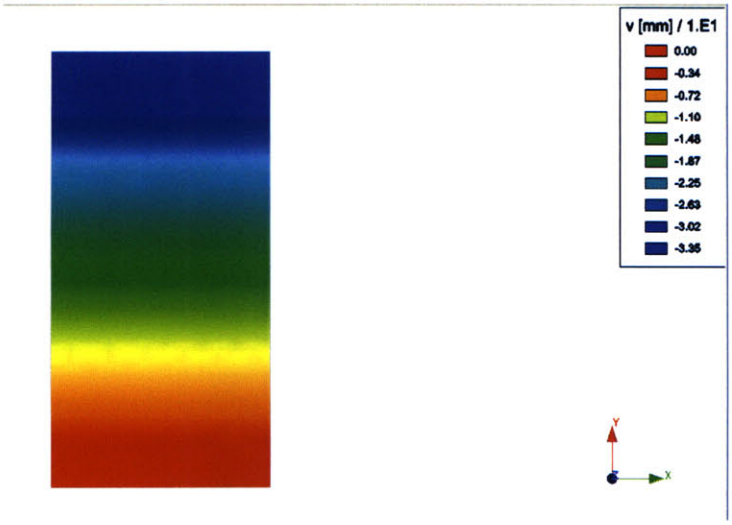


On the  tab it is possible to draw points, to measure the changing of in situ properties with time and cross sections.

On the  tab it is possible to plot data for the points and cross-section draws on the  tab. The  tab allows for exporting of the results in .txt format.

## A.8 Undrained shear: Restart

In order to go from a fully drained to an undrained condition it is necessary to perform a restart. Repeat step 2. However, when the choice arises between "initialization of parameters" and " simple restart" choose restart.

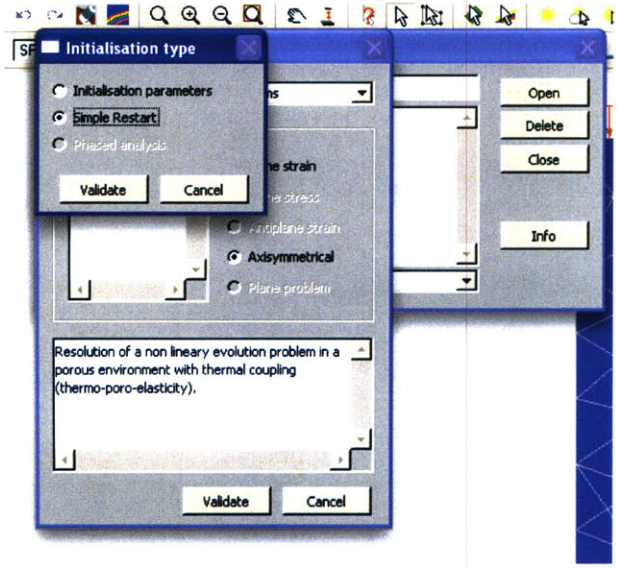


Apply soil parameters the same as before. Instead of initializing the initial condition after clicking on  , a box will appear for file import. Import the restart file created in step 5.

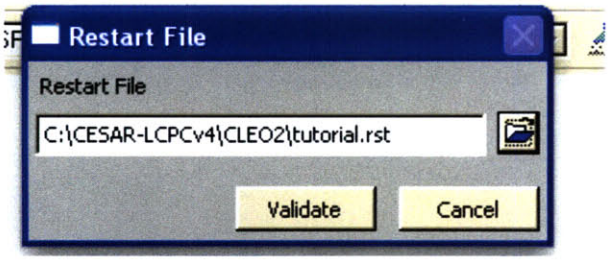


Apply the boundaries in the same way as above, with two differences:

1) Do not apply any drainage boundaries (this is a fully undrained analysis)
2) On a separate boundary sheet apply a physical boundary to the top surface

Click on  to open a second boundary sheet for the same simulation. Give it a name and validate.

Select to top surface and apply a -10 mm-vertical displacement.

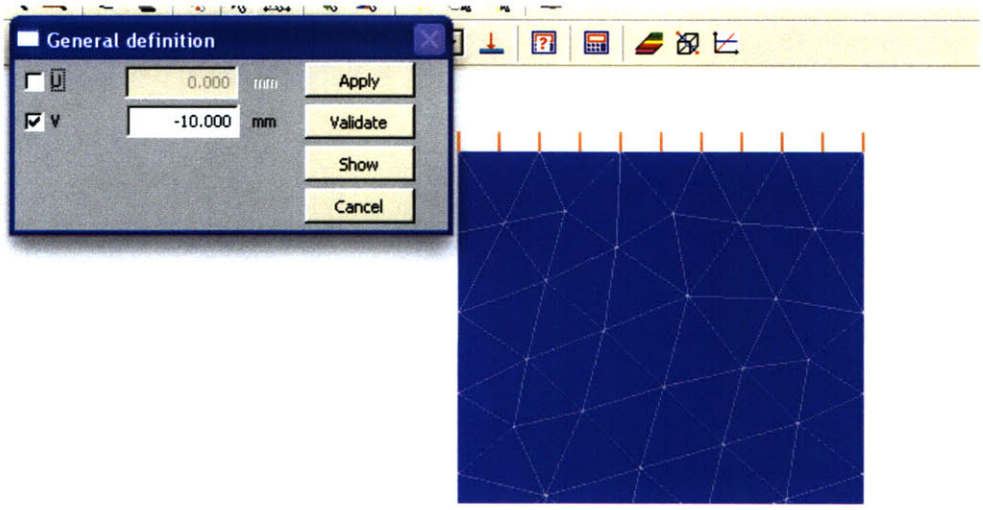


Open a load tab to complete the model but apply no loads.

---

 Initialize calculations parameters. Repeat step 6 with 20 increments 1 hour long starting at 0 hours. Instead of controlling the loads the top boundary will be controlled

using multipliers of the applied 10 mm displacement. Change the coefficient of the top boundary to range from 3.35 to 22.35 in increments of 1.

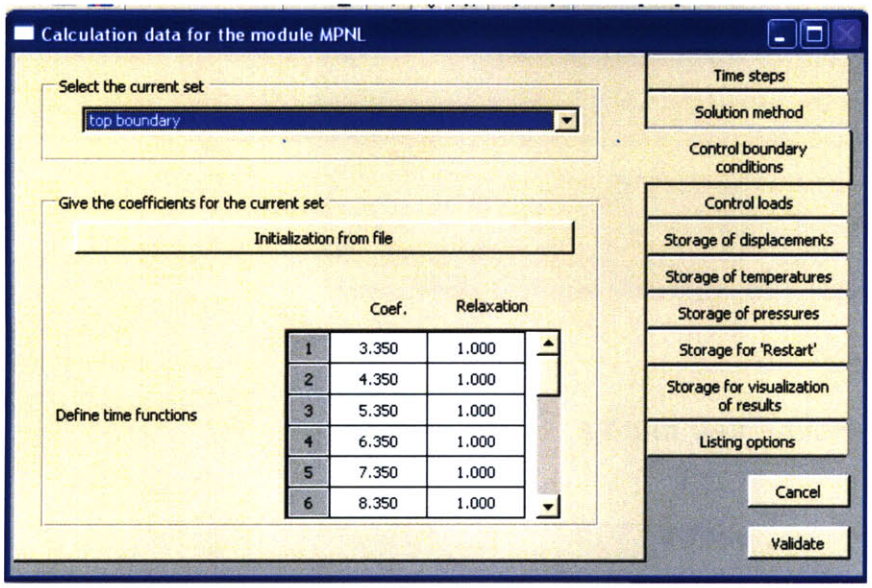


Create the input for solver using the  tap.

Update the soil parameters as in step 6. Run the simulation by solving for existing data.

At the end of this step the sample has been consolidated, fully drained, to p'=112 kPa, q=0, and then shear undrained through displacement control.

To visualize the results of shearing, click on.  . Select  from the left hand toolbar. Draw a point at the midpoint of the sample at x=0, y=-0.5. Using  name the point. Go to 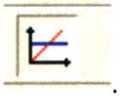 . Using  it is possible to plot the excess pressure at the point with increments of load.

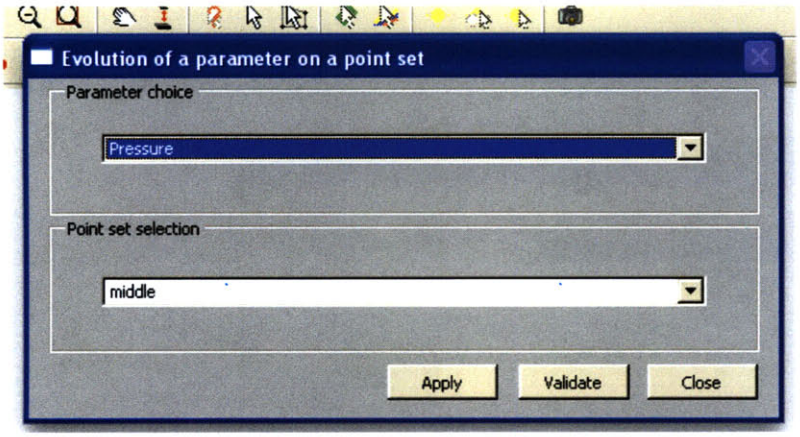


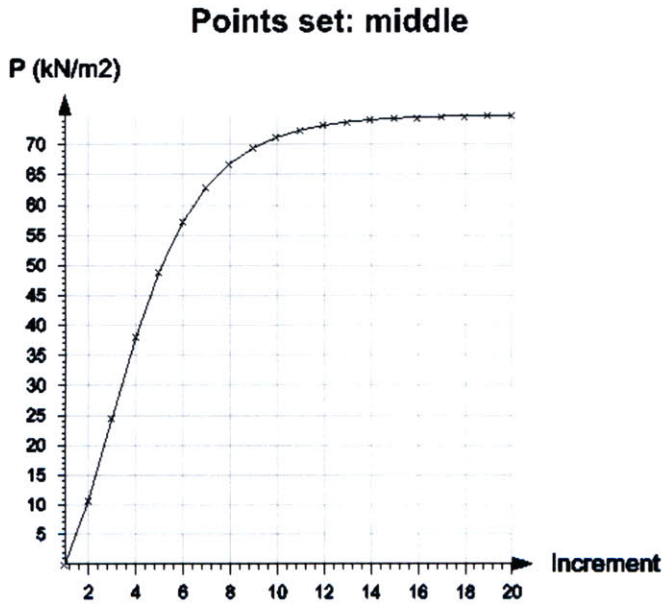


## A.9 Applying thermal loads

In the example above it was not necessary to apply a thermal load as the entire test was run at constant temperature. However, in other types of simulations it will be very important to apply a thermal load. The CESAR-LCPC interface has a simple method for applying thermal loads similar to applying mechanical loads on the "Loads" tab.

Unfortunately, they do not generate properly in the Picard (1994) model and it is necessary to apply thermal loads manually, similar to entering the material parameters.

To apply thermal loads begin by applying a MECHNICAL load of the same order of magnitude in $N/m^2$ as desired for the THERMAL load in $W/m^2$.

For example, to apply a 10 $W/m^2$ heat flux to the top surface of the sample. Apply a 10 $N/m^2$ (or a 0.01 $kN/m^2$) mechanical load to the top surface. Once the entire model is set up generate 'input for solver' and open the .data file.

Locate the section in the .data file that is titled PUR and has on the last line the magnitude of the applied load. If two or more loads are applied simultaneously (especially if one is mechanical and the other thermal) it is very important to identify the correct load. Change the letters "PUR" to "FUS"; this changes the load from mechanical to thermal.

```
PUR
5   3
2   9   1   9   21   11   21   44   23   44
71   46   71   91   73
-10.00000
```

```
FUS
5   3
2   9   1   9   21   11   21   44   23   44
71   46   71   91   73
-10.00000
```